THESIS FOR THE DEGREE OF LICENTIATE OF ENGINEERING

Material Solutions for Mitigating High Temperature Corrosion in Biomass- and Waste-fired Boilers

Utilizing Novel FeCrAl Alloys and HVAF-sprayed Ni-based Coatings

Johan Eklund

CHALMERS

Department of Chemistry and Chemical Engineering

CHALMERS UNIVERSITY OF TECHNOLOGY

Gothenburg, Sweden 2018

Material Solutions for Mitigating High Temperature Corrosion in Biomass- and Waste-fired Boilers Utilizing Novel FeCrAl Alloys and HVAF-sprayed Ni-based Coatings

Johan Eklund

Thesis for the degree of Licentiate of Engineering
Nr: 2018:23
Department of Chemistry and Chemical Engineering
Chalmers University of Technology
SE-412 96 Gothenburg
Sweden
Telephone + 46 (0)31-772 1000

Cover: SEM cross section images of FeCrAl alloys with varying silicon content (upper) and three different HVAF-sprayed coatings (bottom) after exposure in O_2+H_2O+KCl at 600 °C for 168 hours. See pages 40-42 and 49-50 respectively for further information.

Printed by Chalmers Reproservice

Gothenburg, Sweden 2018

Abstract

Combustion of biomass and waste for heat and electricity production is a promising alternative to fossil fuels and is thereby an important step towards a more sustainable future. However, due to substantial amounts of alkali- and chlorine-containing species as well as moisture in biomass and waste, the combustion of these results in a highly corrosive environment which accelerates the degradation of steel components in the boiler, drastically increasing the maintenance costs. One way to reduce the corrosivity in the boiler is to reduce the operating temperature but this simultaneously reduces the electrical efficiency of the boiler process. To retain the combination of optimized operating parameters of the boiler and low maintenance costs, new and improved material solutions has to be considered. In this study two different approaches has been investigated; improving corrosion properties of the material by altering the alloy composition and utilizing thermally sprayed high alloyed coatings.

The first approach, to improve corrosion resistance by altering the composition, has been focused on FeCrAl alloys. FeCrAl alloys has been shown to exhibit good corrosion properties at elevated temperatures due to the formation of α-alumina (above 900 °C) and transient forms of alumina (below 900 °C). However, in very harsh environments these protective oxides tend to break down, resulting in rapid material degradation. It is therefore of interest to further improve the corrosion resistance of FeCrAl alloys, one possible approach is to alter the alloy composition. Minor additions of silicon has been shown to have great beneficial effects on the corrosion behaviour of stainless steels. It is however not known if the presence of silicon affects the corrosion behaviour of FeCrAl alloys in the same way. Thus, in this study, FeCrAl model alloys with varying silicon content were exposed in O_2, O_2+H_2O and O_2+H_2O+KCl at 600 °C in order to investigate the possibility of improving the corrosion properties of FeCrAl alloys. The results showed minor additions of silicon drastically improved the corrosion resistance of FeCrAl alloys in the presence of water vapour and KCl. In the presence of water vapour, the silicon containing alloys retained a protective oxide while displaying breakaway oxidation in the absence of silicon. In the presence of KCl, all alloys formed iron oxide but addition of silicon drastically reduced the oxide growth rate.

Utilizing coatings to protect different components from degradation due to corrosion attack is used in many applications. However, in very harsh environments, the density of the coating becomes crucial for achieving a good corrosion protection. The more novel thermal spraying technique, High Velocity Air-Fuel (HVAF) has been shown to obtain coating with higher density and improved substrate adherence than other techniques. Therefore, in this study, the possibility of using coatings for corrosion protection in biomass and waste-fired boilers was investigated by exposing three Ni-based HVAF-sprayed coatings (NiCr, NiAl and NiCrAlY) in O_2+H_2O and O_2+H_2O+KCl at 600 °C. The results showed that the NiCr coating failed to prevent the diffusion of corrosive species such as chlorine to the substrate, leaving it vulnerable to severe corrosion attacks. However, both the NiAl and NiCrAlY coatings managed to prevent the diffusion of chlorine and only displayed minor oxide formation at the coating surface.

Keywords: High temperature corrosion, Biomass, Waste, FeCrAl alloys, Silicon, HVAF, Ni-based coatings

List of publications

The thesis is based on the following papers:

Paper I

J. Eklund, B. Jönsson, A. Persdotter, J. Liske, J.-E. Svensson, T. Jonsson. The influence of silicon on the corrosion properties of FeCrAl model alloys in oxidizing environments at 600 °C, Corrosion Science, Volume 144, 2018, Pages 266-276, ISSN 0010-938X, https://doi.org/10.1016/j.corsci.2018.09.004.

Paper II

J. Eklund, J. Phother, E. Sadeghi, S. Joshi, J. Liske
High Temperature Corrosion of HVAF-Sprayed Ni-Base Coatings for Boiler Applications
Submitted to Oxidation of Metals

Statement of the author's contribution

I was responsible for the scientific writing of both included papers. I did all the experimental work along with most of the analysis of Paper I. Amanda Persdotter performed preparation, imaging and analysis of some of the ion milled cross sections in Paper I. In Paper II, Esmaeil Sadeghi and Shrikant Joshi were responsible for the thermal spraying of the HVAF-sprayed coatings. I performed half of the experimental work in Paper II, including corrosion tests and analysis of exposed samples. Julien Phother performed the other half of the experimental work in Paper II.

Related work and technical reports not included in this thesis

Sadeghimeresht E, Eklund J, Phother Simon J, Liske J, Markocsan N, Joshi S. Effect of water vapor on the oxidation behavior of HVAF-sprayed NiCr and NiCrAlY coatings *Materials and Corrosion*. 2018;69:1431-1440.

M. A. Olivas-Ogaz, J. Eklund, J.-E. Svensson, J. Liske and T. Jonsson, Microstructural Study of the Influence of KCl and HCl on Preformed Corrosion Product Layers on Stainless Steel, Oxidation of Metals 87 (2017) p. 801-811.

M. A. Olivas-Ogaz, J. Eklund, A. Persdotter, M. Sattari, J. Liske, J-E. Svensson, T. Jonsson
The influence of oxide scale microstructure on KCl(s) induced corrosion of a low-alloyed steel at 400 °C, Accepted in Oxidation of Metals 2018

L. Mikkelsen, T. Jonsson, L. Paz, J. Eklund, J. Liske, B Jönsson, N. Israelsson, S. Selin, J. Hernblom, J. Högberg, J. Nockert Olovsjö ”Increased steam temperature in grate fired boilers - Steamboost” *KME report 2018*

Table of Contents

1 Introduction

Since around 1960, the average global temperature has been increasing at an alarming rate, see Figure 1a [1]. As a result of this, glaciers and polar ices are melting, sea levels are rising [2] and extreme weather such as heat waves, droughts, floods and hurricanes has increased [3]. The climate changes are posing a serious threat against the biodiversity on our planet as well as human health. There is strong evidence that most of the rise in temperature is caused by increased levels of greenhouse gases in the atmosphere caused by human activities [4-6]. The main greenhouse gases are carbon dioxide (CO_2) methane (CH_4) nitrous oxide (N_2O) and fluorinated gases with carbon dioxide being the most abundant. The increase in the average global temperature has been shown to correlate with the increased amount of carbon dioxide in the atmosphere (see Figure 1 and Figure 2) which increased drastically around 1960.

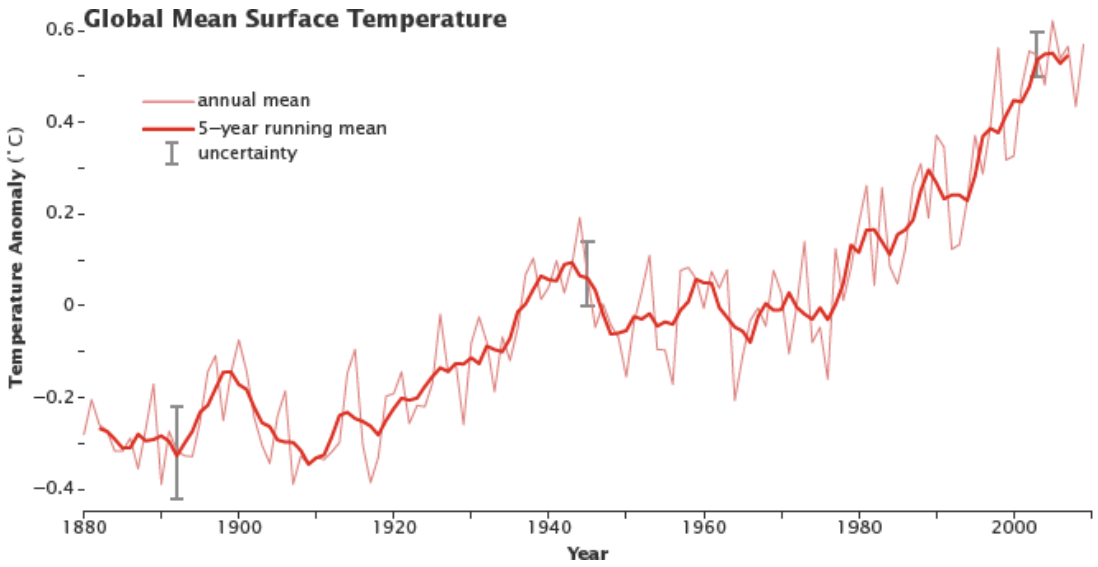

Figure 1: Graph showing the increase in the global mean surface temperature [1].

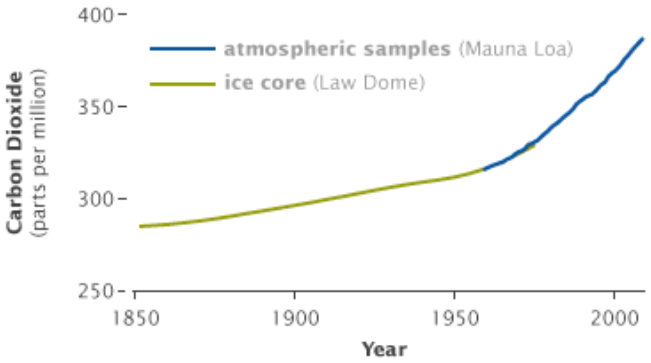

Figure 2: A graph showing the increase of carbon dioxide concentration in the atmosphere [1].

The increased pollution of CO_2 is mainly a result of the combustion of fossil fuels but also due to deforestation which reduce the CO_2 –absorbing effect. Fossil fuels are primarily used in automotive vehicles, in heat production for houses as well as for electricity production in power plants. Concurrently, the need for electricity is becoming larger in today's society due to the increase in industrial processes, more widespread use of electrical devices as well as increased electricity

requirements for these. The substitution of fossil fuel based vehicles with electrical vehicles in the recent years also leads to an increased electricity need and makes the energy source for electricity production even more crucial. Besides the environmental impacts of the combustion of fossil fuels, these are of limited supply and not renewable. It is therefore of utmost importance to develop renewable and more CO_2-neutral energy sources to substitute fossil fuels.

Biomass and certain types of waste are examples of alternative fuels that are both renewable and relatively CO_2 neutral. These can be combusted in a boiler to produce steam for use in turbines which subsequently generates electricity. The use of biomass and waste as fuels has already been implemented in Sweden, along with other Scandinavian countries. However, this has been shown to result in major technical difficulties, such as high maintenance costs and reduced efficiency of the boiler process.

Biomass and waste contains high amounts of alkali- and chlorine containing species as well as a rather high amount of water compared to fossil fuels. When combusted, these species are released in the boiler and results in a complex and severely corrosive environment. This leads to material degradation of metallic parts in the boiler and significantly reduces the lifetime of these. The superheaters in the boiler, exhibits higher material temperatures than other parts of the boiler, which results in an even more corrosive environment. To increase the lifetime and reduce maintenance costs of the superheaters, boiler operators have been forced to reduce the steam temperature. However, in doing so, the electrical efficiency of the boiler is reduced which decreases the electrical output and in turn complicates the substitution of fossil fuels. The composition of biomass and waste is varying with time which results in fluctuating harshness of the boiler environment.

Low alloyed steels as well as stainless steels are commonly used in the superheaters because of the good mechanical properties and fabricability of these as well as corrosion properties of the latter. However, in order to facilitate an increase in steam temperature to improve the electrical efficiency, more corrosion resistant materials are needed. Stainless steels generally contain at least 12% Cr in order to form a protective Cr-rich oxide layer. However, in the complex environment in the biomass and waste fired boiler, containing alkali compounds as well as high amounts of water vapour, the protective chromia layer has been shown to break down [7-10] through two separate corrosion mechanisms.

Alumina forming alloys such as FeCrAl alloys are commonly used at high temperatures (above 900 °C) in various different applications, such as ignitors, furnace rollers, gas burners electrical elements etc. and has been shown to exhibit excellent corrosion resistance in oxygen and water vapour containing environments at up to 1300 °C [11-13]. The high oxidation resistance of FeCrAl alloys at higher temperatures is due to the formation of an α-alumina layer. The α-alumina is highly protective and slow growing because of its high degree of stoichiometry. The vapour pressures of the volatile species over α-alumina are much smaller than those over chromia in the presence of water vapour and has also been shown to remain protective in the presence of KCl [14] and other alkali containing compounds. However, at lower temperatures (below 900 °C) transient forms of alumina have been shown to form at temperatures as low as 600 °C [15] which has been reported to contain small amounts of Fe and Cr [16]. Thus, below 900 °C, FeCrAl alloys may not be as resistant towards water vapour and alkali containing compounds. Increasing the amount of Cr and Al as well as adding small amounts of reactive elements and/or Si to the alloy may improve the protectiveness of the alloy [17-23]. However, this is often associated with economical drawbacks as well as negative impacts on the mechanical properties of the alloy. It is therefore important to find a balance between good corrosion properties, good mechanical properties and price.

A way to avoid the difficulties regarding mechanical properties is to use high alloyed steels as coatings. In this way, a high corrosion resistance can be achieved by spraying the coating on a substrate with good mechanical properties. Using a coating is also usually more economically favourable. Previous use of coatings for corrosion resistance at high temperatures has encountered problems such as porosity and poor adherence to the substrate, resulting in the failure of the coating. Recently, new spraying techniques has been developed. Among them is the high velocity air fuel (HVAF) technique that has been shown to be able to produce more dense coatings (lower degree of porosity) with better substrate adherence [24, 25].

The knowledge regarding the altering of composition in FeCrAl alloys to enhance corrosion properties can be utilized when designing coatings for corrosion protection. Therefore, the overall aim of this study is to investigate both approaches in parallel and evaluate the possibilities for utilizing these to mitigate the high temperature corrosion in biomass- and waste-fired boilers. Si was selected as a corrosion protection enhancing element and the effect of minor additions on the corrosion properties of FeCrAl alloys was investigated in several corrosive environment at 600 °C. Simultaneously, the performance of HVAF-sprayed Ni-based coatings in a highly corrosive environment (at 600 °C in the presence of water vapour and KCl) was investigated.

2 Combustion of biomass and waste for power generation

Combustion of a fuel in a boiler is a widely used concept for generating power as well as heat. The majority of fuels are based on fossil fuels such as coal but recently, with the increasing awareness of the negative effects of the pollution of greenhouse gases, more environmentally friendly fuels are being used. An example of such a fuel is biomass and waste which can be combusted in a similar way. The design and size of the boilers differ (Grate Firing boilers and Fluidized Bed boilers are the most commonly used) but the fundamental concept is the same and is based on converting heat energy to mechanical work in order to generate electricity using turbines. The heat produced can also be used for district heating. During the combustion of the fuel a hot flue gas is produced which, by using heat exchangers (superheaters), heats up water. As a result of this the water evaporates but is further heated until it reaches a temperature far above the saturation temperature. Superheated steam becomes pressurized in a confined space and therefore contains a large amount of internal energy. This is utilized as the steam enters the turbine where the steam can expand which enables the turbine to drive an electric generator. The low-pressure steam from the turbine is later condensed and can be recycled in the process or used for district heating. This is known as the Rankine cycle, illustrated in Figure 2, and the efficiency of this process is dependent on the temperature and pressure of the superheated steam that enters the turbine [26].

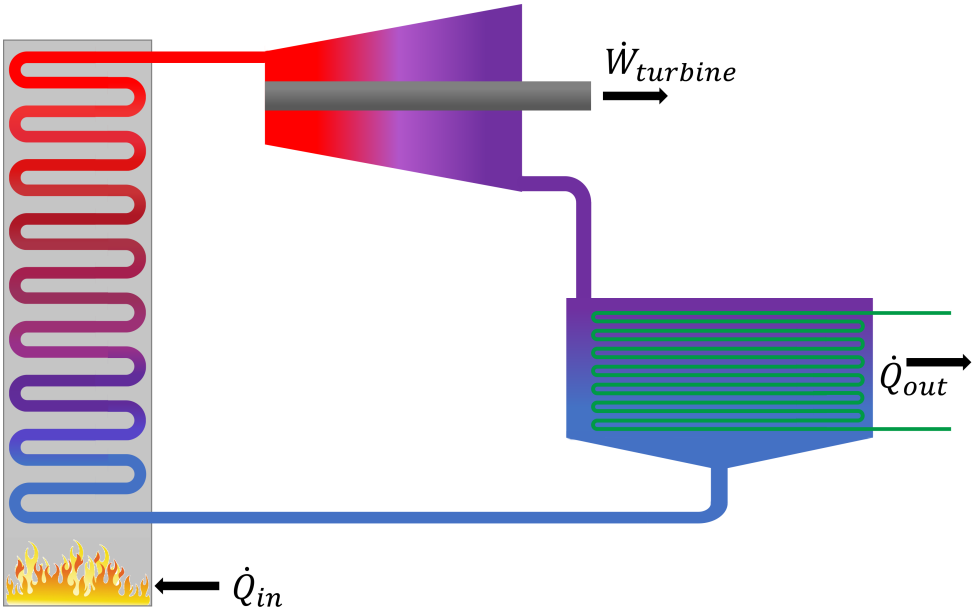

Figure 3: Schematic illustration of the Rankine cycle.

Thus, to improve the efficiency of the process, the temperature of the steam in the superheaters should be maximized. However, with higher temperatures several problems regarding the material of the superheater arises. Firstly, mechanical properties such as tensile strength and creep strength is decreased with temperature for metals in general. Simultaneously, the pressure of the superheated steam increases with increasing temperature which results in higher requirements regarding the mechanical properties of the superheater material. Secondly, at higher temperatures, corrosion reactions occur at a higher rate which may result in severe degradation of the material. Combining both good mechanical properties and good corrosion behaviour is challenging and finding a balance between these two is crucial. This will be further discussed in chapter 3.

One of the major problems regarding the combustion of biomass and waste as an alternative to coal is the altered composition of the flue gas. When combusting biomass and waste the amounts of several

corrosive species, such as water vapour, HCl(g) and alkali salts (NaCl and KCl) are significantly increased [27-30]. Thus, in addition to the high temperatures the superheaters are exposed to, the increased corrosiveness of the flue gas results in severe corrosion attacks and rapid material degradation. As a result of this, boiler operators are forced to reduce the temperature of the superheated steam which consequently reduces the efficiency of the process. Two alternative approaches to reduce the material degradation is changing the fuel composition (for example through sulphur additives [28, 29, 31, 32]) or changing the material of the boiler components. The latter will be discussed in the upcoming chapter.

3 Materials

A huge range of different materials are used in different applications, requiring different properties. In load bearing applications, such as infrastructure, mechanical properties are of utmost importance. These may include mechanical strength, ductility and creep strength. In applications involving electrical equipment, physical properties such as electrical conductivity is essential. In many power production applications, a materials thermal conductivity is important when dealing with the transportation of heat through high temperature fluids and gases (heat exchangers such as superheaters). Along with the high temperature, the corrosion properties of the exposed materials are increasingly important to reduce the maintenance costs of the power plant. For some components, pressure bearing capabilities are crucial as well and a balance between the most important properties has to be established. Today, the materials used for superheaters are low-alloyed steel and stainless steels due to their high mechanical strength of the former and high corrosion resistance of the latter. As described in chapter 2, the environment in a biomass- and waste-fired boiler is highly corrosive, especially in the conditions which the superheaters are exposed to, and results in accelerated corrosion for both low-alloyed and stainless steel (due to the breakdown of the protective oxide). Thus, other material solutions are needed to reduce maintenance costs and increase efficiency of the boiler. In the following subchapters, two alternative material approaches will be described.

3.1 FeCrAl alloys

FeCrAl alloys are ferritic iron-based alloys with a body-centred cubic (bcc) crystal structure. Commercial FeCrAl alloys generally contain roughly 20 wt% Cr and 1-5 wt% Al and are most commonly used in high temperature applications (900-1300 °C) such as ignitors, furnace rollers, heating elements in industrial furnaces etc. The reason for this is their superior oxidation resistance at higher temperatures due to the ability to form an α-Al_2O_3. The α-Al_2O_3 is a highly stoichiometric oxide and is therefore slow growing and highly protective.

In power production, the material temperature of the different components is varying but is generally below 900 °C. This is not necessarily positive since at temperatures below 900-950 °C, transient forms of alumina (γ-, δ- and θ-Al_2O_3) usually forms instead, in which the rate of ion transport is higher and therefore does not provide an equally good corrosion protection [11].

As the reason behind the great corrosion properties of FeCrAl alloys their ability to form an alumina scale, the high presence of Cr in the alloy may seem confusing. FeAl alloys can also form the same type of protective alumina scale, but it has been shown to form internal oxidation and nitridation due to the low activity of Al even at relatively high temperature (1300 °C) [33]. Increasing the Al content reduces the degree of internal oxidation/nitridation but also has negative impacts on mechanical properties of the alloy, such as fabricability [34] and reduction in high-temperature strength which limits the Al addition to the alloy for applications which need good pressure bearing properties. However, upon addition of Cr to the FeAl alloy, the amount of Al needed to form an α-Al_2O_3 is reduced [35] and thus, so is the problem regarding internal oxidation/nitridation. However, even for FeCrAl alloys, the pressure bearing properties are generally insufficient for integrating them for use in superheaters in power generation boilers. Increasing the amount of other corrosion resistance enhancing elements such as Cr and Si has also been shown to negatively affect the mechanical properties of the alloy, resulting in embrittlement and further negative effects on the fabricability (increased deformation resistance and ductile-to-brittle transition temperature (DBBT)) [36-38]. Decreasing the Al and Cr contents to levels at which sufficient mechanical properties are achieved would result in poor corrosion properties. One viable solution for this problem could be to use a compound tube, which is a tube consisting of an outer and an inner component which are mechanically bonded through hot extrusion. By selecting a corrosion resistant outer component (such as a FeCrAl

alloy) and an inner component with good mechanical properties, these properties can be combined. However, interdiffusion of elements may occur at elevated temperatures between materials of different composition which is in physical contact. Interdiffusion of Al and Cr from the outer component to the inner component may have negative impacts on the mechanical properties (such as embrittlement). Another solution for combining corrosion resistance with good mechanical properties is the use of a coating which will be described in the following subchapter.

3.2 Coatings

In many applications, the use of coatings is a good way to protect or add specific surface properties to a material. These kind of properties can range from functional properties such as adhesion, wettability and even electrical conductivity to protective properties such as wear resistance and corrosion resistance. In this study, coatings have been used to increase the corrosion resistance of low alloyed steels.

Coatings can be applied to a surface in several different ways, depending on the application requirements. For corrosion protection, the density of the coatings is of utmost importance regarding the protectiveness of the coating. A coating with a low degree of porosity is essential to prevent the underlying material from being exposed to the corrosive atmosphere. The state of the art thermal spraying technique HVAF (High Velocity Air-Fuel) has been shown to produce coatings with low degree of porosity, low oxide content [24, 25] and high bond strengths compared to other thermal spraying techniques. This is due to the much higher particle velocity (1100-1200 m/s) and lower particle temperature (1500 °C) [39] compared to other spraying techniques such as HVOF (High Velocity Oxy-Fuel) and APS (Atmospheric Plasma Spraying) for which the particles exhibit particle velocities of 550 m/s [40] and 300 m/s [41] respectively and temperatures of 3000 °C [40] and 15000 °C (flame temperature) [41] respectively.

As mentioned in the previous subchapter, the disadvantage of high alloyed steels is their relatively poor mechanical properties and fabricability which limits the addition of Cr, Al etc. The use of corrosion protective coatings eliminates these kind of limitations which enables the use of higher amounts of elements that contribute to better corrosion protection. However, there are some complications regarding coatings as well, such as porosity and adhesion. The porosity is greatly reduced upon using the HVAF spraying technique but may still be to a large enough degree to enable the transport of corrosive species to the substrate. For coatings in general, the adhesion of the coating to the substrate may be problematic, as the thermal expansion coefficient of the coating and the substrate may differ, resulting in mechanical stresses during temperature fluctuations (for example during cycling) and may lead to spallation of the coating. In this study, HVAF coatings were produced by University West. The performance of these was investigated by exposing them in a corrosive environment, mimicking the environment in a biomass- and waste-fired boiler, in order to assess the possibility of using HVAF-sprayed coatings for corrosion protection.

3.3 Corrosion problems at high temperatures

Most high temperature applications are associated with different degrees of corrosion problems. In order to find viable solutions for these problems, such as altering the design (or fuel) of the application, selection of materials etc. it is of utmost importance to understand why oxidation/corrosion occur and what mechanisms are involved. In the following chapter, the fundamentals of oxidation/corrosion of metals will be explained.

4 Oxidation of metals

Most metals and alloys are thermodynamically unstable in an oxygen-containing atmosphere and therefore spontaneously react with the environment, forming different oxides which depends on several factors regarding the specific environment the metal is exposed to [11]. The temperature is one of the main factors, as the rate of oxidation reactions is increased with temperature [35]. However, not only the rate of the oxidation reactions is affected by the temperature, but also the spontaneity of the reactions which determines what oxides form. This is also affected by the oxygen partial pressure, $p(O_2)$, in the surrounding atmosphere.

The oxidation resistance of a metal and/or alloy, is dependent on the formation of a protective and well adherent oxide. Thus, the surrounding environment as well as the alloy chemistry are crucial factors to take into consideration when choosing a material for a specific application.

4.1 Thermodynamics

The chemical reaction between a metal, M, and oxygen gas, O_2, may be written as:

$$xM(s) + \frac{y}{2}O_2(g) \rightleftharpoons M_xO_y(s) \qquad \text{(Reaction 4.1)}$$

The spontaneity of Reaction 4.1 is determined by the second law of thermodynamics which can be written in terms of Gibbs free energy (G) of a system if the assumptions of constant temperature and pressure applies:

$$G = H - TS \qquad \text{(Equation 4.1)}$$

where H and S is the enthalpy and the entropy of the system respectively and T is the temperature. At the above conditions (constant temperature and pressure) the reaction is spontaneous if ΔG has a negative value. The reaction is instead thermodynamically unfavourable if the value of ΔG is positive and at equilibrium if ΔG is equal to zero [42]. On a basis of one mole O_2, Reaction 4.1 may be written as in Reaction 4.2:

$$\left(\frac{2x}{y}\right)M(s) + O_2(g) \rightleftharpoons \left(\frac{2}{y}\right)M_xO_y(s) \qquad \text{(Reaction 4.2)}$$

Using the relation between ΔG and the activities of the species involved, ΔG for Reaction 4.3 may be expressed as:

$$\Delta G = \Delta G^{\circ} + RT\ln\left(\frac{a_{M_xO_y}{}^{2/y}}{(a_M{}^{2x/y})(a_{O_2})}\right) \qquad \text{(Equation 4.2)}$$

where ΔG° is the Gibbs free energy at standard conditions, R is the universal gas constant, and a is the activity of the reactants and products in Reaction 4.2. At all temperatures and pressures, the activities of pure solids are equal to 1 and by definition, $a_{O_2} = p_{O_2}$ (oxygen partial pressure). Considering the dissociation of an oxide into oxygen gas and metal, at equilibrium, where $\Delta G = 0$, Equation 4.4, can be simplified as follows:

$$\Delta G^{\circ}_{O_2} = -RT\ln p_{O_2} \qquad \text{(Equation 4.3)}$$

where p_{O_2}can be interpreted as the dissociation pressure of oxygen, i.e. the lowest oxygen partial pressure at which the oxide is thermodynamically stable at a given temperature. A convenient way of displaying this for several types of oxides is by means of an Ellingham diagram, see Figure 2.

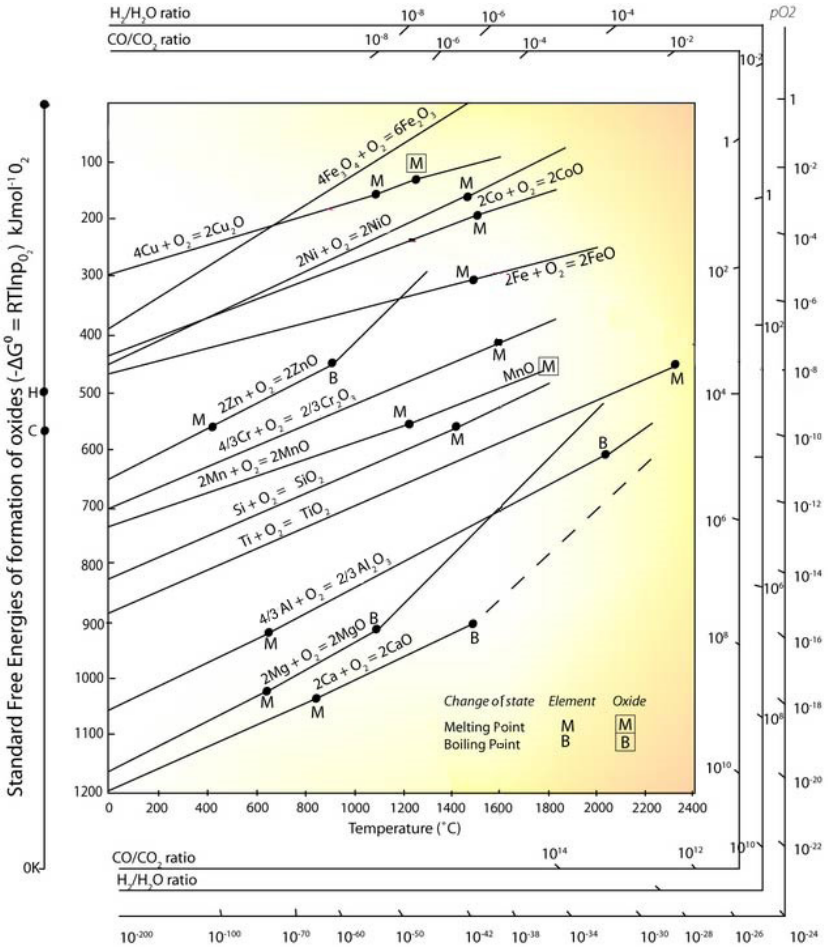

Figure 4: Ellingham diagram displaying the temperature dependence of oxide stability for several metals [43].

4.2 Oxide formation

4.2.1 Initiation of the oxide formation

For the initial oxide formation to take place, oxygen in the atmosphere must be adsorbed on the metal surface and subsequently reduced to O^{2-} ions and, see Figure 4. When the oxygen anions come in contact with the metal cations, a reaction occurs and the oxide formation is thus nucleated. The oxide nuclei continue to grow laterally until a continuous oxide layer has formed on the metal surface [11]. The adsorption of oxygen on the metal surface as well as the oxide formation is affected by the factors such as surface preparation, impurities and defects on the metal surface.

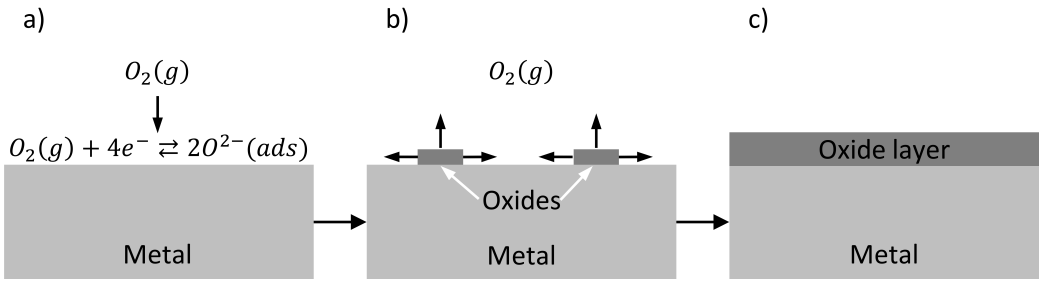

Figure 5: Illustration of the initial oxide formation on a metal surface, initiated by the adsorption of oxygen (a), followed by oxide nucleation (b) and finally the formation of a continuous oxide scale (c).

Once the continuous oxide scale has formed, the metal is no longer in direct contact with the atmosphere (assuming there's no presence of porosity or micro cracks in the oxide). At room temperature this generally means that oxide formation process is inhibited since the diffusion through the oxide scale is too slow. However, as the temperature increases, the diffusion rate of ions within the oxide is rapidly increased [11].

4.2.2 Oxide defects

Above absolute zero temperature all crystalline materials, such as oxides, contain defects in the crystal structure which are essential for ion and electron transport through the material. The types of defects can be divided into two groups[11, 44]:

1. Point defects
2. Line and surface defects

The first type of defects, point defects, are imperfections in the crystal structure which is limited to one lattice site, such as vacancies or interstitial atoms. Also impurities, such as foreign atoms, are considered point defects. In stoichiometric crystals, the number of cations and anions are in balance resulting in a low defect concentration which mostly consists of Schottky and Frenkel defects, see Figure 5 and Figure 6.

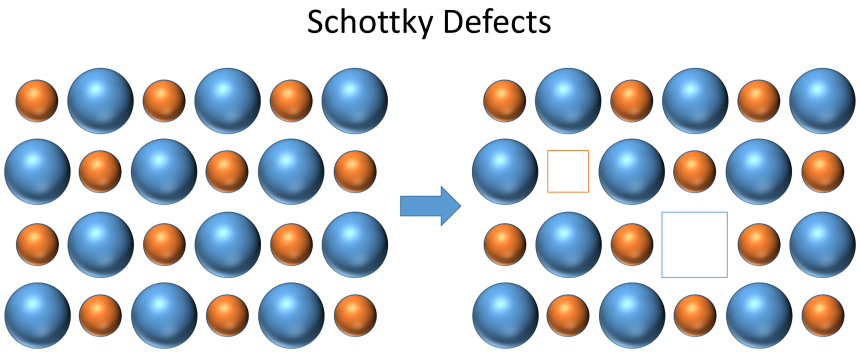

Figure 6: Schematic illustration of Schottky defects.

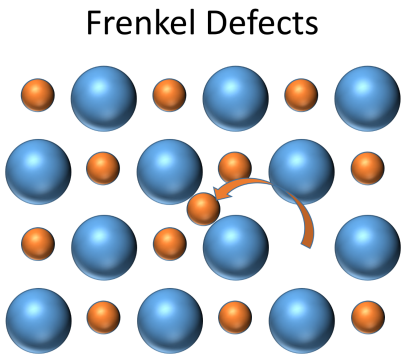

Figure 7: schematic illustration of Frenkel defects

Schottky defects involves the formation of a cation vacancy which is balanced by an anion vacancy to maintain charge neutrality. Frenkel defects instead involves the relocation of a cation to an interstitial lattice site, leaving behind a cationic vacancy. Both of these defects increase the ion mobility in the crystalline material but does not provide a mechanism by which electrons may be transported [42].

In non-stoichiometric oxides, the defect concentration is higher than stoichiometric oxides and can be classified as semiconductors, i.e. a material that has an electrical conductivity value somewhere

between a conductor and an insulator. These oxides can behave as either p-type or n-type semiconductors. In p-type semiconductors there is a deficiency of metal or excess of oxygen in the crystal structure in the form of metal vacancies or interstitial oxygen. These defects result in a negative charge which is compensated by positive electron holes. In n-type semiconductors, there is either a metal excess or an oxygen deficiency in the form of interstitial metal ions or oxygen vacancies. These instead results in a positive charge which is compensated by excess electrons [11, 42].

The second group of defects, line and surface defects, comprise several types of defects. One of them is edge dislocation in which a plane of atoms is terminated in the middle of the crystal. Grain boundaries are important interfacial defects in which grains with different crystallographic orientations are separated, see Figure 7.

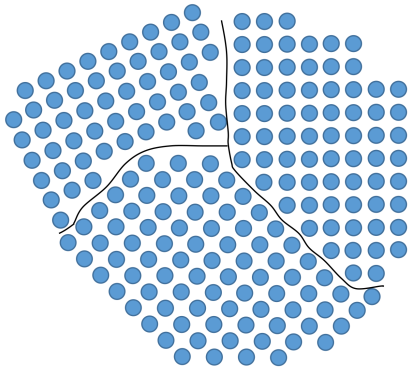

Figure 8: Schematic illustration of grains with different crystallographic orientation resulting in grain boundaries.

The irregularity along a grain boundary is resulting in a higher energy state of the bonded atoms which causes a higher chemical reactivity [44]. Due to this, impurities tend to preferentially segregate along the grain boundaries.

4.2.3 Diffusion

As mentioned in the previous subchapter, the transportation of ions in any crystalline material, such as oxides, occurs through defects present in the material. There are several different diffusion paths and mechanisms that can take place depending on the type of defects that are present. The mechanisms can be divided into two groups [11]:

- Lattice diffusion
- Short-circuit diffusion

The two types of mechanisms have different diffusion coefficients, depending on the element, the present phases and the temperature [11]. This is described in Equation 4.4:

$$D = D_0 e^{-\frac{Q_D}{RT}} \qquad \text{(Equation 4.4)}$$

where D is the diffusion coefficient, D_0 is the frequency factor (temperature independent) and Q_D is the activation energy for diffusion.

4.2.3.1 Lattice diffusion

Transport of ions through lattice diffusion takes place due to the presence of point defects, described in the subchapter 4.2.2. The main mechanisms for lattice diffusion are illustrated in Figure 8 [11].

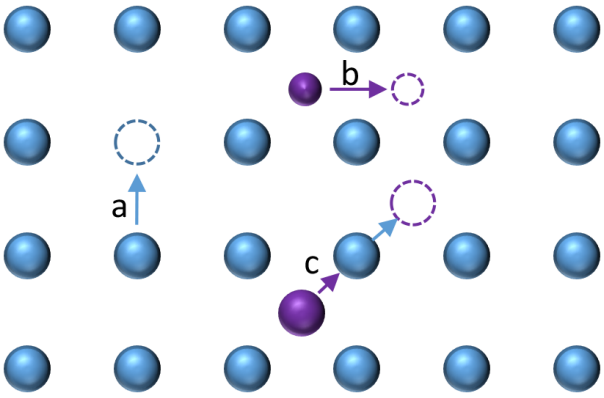

Figure 9: Schematic illustration of the three main mechanisms of lattice diffusion; a) vacancy diffusion, b) interstitial diffusion and c) interstitialcy diffusion.

Vacancy diffusion occurs due to the presence of vacancies in the crystal structure. The mechanism consist of the movement of an atom or ions from a regular lattice site to an adjacent vacancy, resulting in another vacancy.

Interstitial diffusion is most common for smaller atoms or ions that are situated at an interstitial lattice site and consist of the movement from one interstitial site to an adjacent vacant interstitial site. The mechanism can occur for larger atoms or ions as well but may result in distortions in the crystal structure.

Interstitialcy diffusion consists of the dislocation of an interstitial atom or ion to an occupied regular lattice site, forcing the atom or ion to move to an adjacent interstitial lattice site.

4.2.3.2 Short-circuit diffusion

Line defects, such as grain boundaries, were described in subchapter 4.2.2. These are especially important when it comes to the diffusion on ions in oxides at lower temperatures (below 600 °C). This is due to the much greater flux of atoms and ions along the grain boundaries compared to lattice diffusion which is small at low temperatures. This can be explained by higher energy state of the atoms bonded along the grain boundaries, which leads to a significantly lower activation energy compared to lattice diffusion. Thus, at lower temperatures, the transport of ions through the oxide is dominated by grain boundary diffusion [44, 45]. As the temperature increases, the importance of lattice diffusion increases and thus the contribution of lattice diffusion is brought closer to that of the grain boundary diffusion. However, this also depends on the defect concentration as well as the grain size in the material (smaller grains result in larger boundary area). In highly stoichiometric oxides such as α-Al_2O_3, with low defect concentrations, grain boundary diffusion is dominating even at higher temperatures.

4.3 Oxidation kinetics

Throughout the oxidation process the weight of the metal is increased due to the oxide formation. Because of this, the oxidation rate of the metal can be measured by weighing continuously or at certain intermediate intervals of the oxidation process. Generally, the oxidation rate can be described by three different kinetic laws, namely the linear, parabolic and logarithmic rate laws [11], see Figure 9.

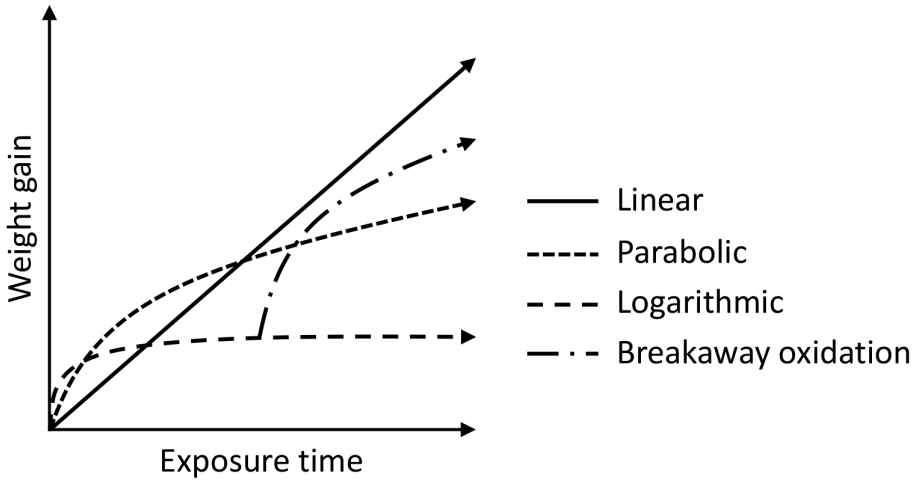

Figure 10: Schematic representation of the three most common kinetic rate laws during oxidation as well as breakaway oxidation.

Investigating the kinetics of the oxidation process is of great importance to obtain valuable information regarding the oxide formation, the properties of the oxide scale(s) and the oxidation mechanisms involved. In reality, the kinetic laws largely depend on factors such as temperature, oxygen partial pressure in the present environment, surface preparation, pre-treatments, the alloy chemistry (determines what oxides may form) and indications about the rate-determining mechanisms. In some cases, it is not possible to describe the oxidation rate with only one kinetic equation but a combination of two or more. This also, gives valuable information about the oxidation process.

4.3.1 Linear rate law

In some cases, the oxidation process can be described with the linear rate equation (Figure 9), that is, when the oxidation rate is constant with time. The linear rate equation is expressed as [11]:

$$\frac{dx}{dt} = k_l \qquad \text{(Equation 4.5)}$$

$$x = k_l t + C \qquad \text{(Equation 4.6)}$$

where x is the oxide thickness, t is the amount of time since the beginning of the oxidation process, k_l is the linear rate constant and C is the integration constant. Since the oxide thickness, x, is assumed to be equal to zero at the beginning of the oxidation process (t=0), C is equal to zero. If the oxidation rate can be described by the linear rate equation, the rate determining step may be a surface or phase boundary process or a reaction [11]. This may involve a steady-state reaction which is limited by the adsorption of oxygen at the oxide/gas interphase when diffusion through the oxide scale is rapid. This mostly occurs when the oxide scale is thin (i.e. beginning of the oxidation process) and the oxygen partial pressure is low or when the formed oxide scale is highly porous, leaving the metal surface exposed.

4.3.2 Parabolic rate law

Many metals are found to follow a parabolic time dependence (see Figure 9) when oxidized at elevated temperatures. The parabolic rate equation is given by:

$$\frac{dx}{dt} = \frac{k_p'}{x} \qquad \text{(Equation 4.7)}$$

$$x^2 = 2k_p' t + C = k_p t + C \qquad \text{(Equation 4.8)}$$

where k_p' and k_p are the parabolic rate constants and C is the integration factor (mostly equal to zero, see subchapter 4.3.1). The parabolic oxidation behaviour was first recognized by Carl Wagner in the 1930s [46]. A parabolic oxidation rate at high temperatures is indicative of a rate determining diffusion process. This may include the diffusion of oxygen ions, metal ions or both through the growing oxide scale. As the oxide scale thickens, the diffusion distance of the reactants increases, resulting in a continuously decreasing oxidation rate with time. Some further assumptions, made by Wagner, was:

- The oxide layer is compact and adherent.
- Thermodynamic equilibrium is established throughout the oxide as well as at the gas/oxide and oxide/metal interface
- Oxygen solubility in the metal may be neglected

4.3.3 Logarithmic rate law

At lower temperature (generally below 300-400 °C) the oxidation process of many metals follow a logarithmic rate, distinguished by the quite rapid initial oxidation rate followed by the deceleration to negligible rates. This kind of corrosion behaviour can often be described by the logarithmic rate equations [11]:

Direct logarithmic (Figure 9): $x = k_{log} \log(t + t_0) + A$ (Equation 4.9)

Inverse logarithmic: $\frac{1}{x} = B - k_{il} \log(t)$ (Equation 4.10)

where x represents the oxide thickness, t denotes the time k_{log} and k_{il} represents the rate constant for the direct logarithmic and inverse logarithmic rates respectively and A and B are constants. What mechanisms are responsible for the logarithmic behaviour is not completely clear but there are several theories, including rate determining chemisorption, rate determining transport or ions or electrons due to electric fields in or across the oxide scale, and cavity formation in the oxide [11].

4.3.4 Breakaway oxidation

The kinetics of highly protective and slow growing oxides usually follows the logarithmic rate law as described above. However, during certain conditions, these oxides may degrade due to reactions with the environment, causing them to break down and therefore lose their protective properties. This can also be caused by physical defects such as cracks or spallation of the oxide layer. The loss of the protective oxide may lead to the formation of more fast-growing oxides which results in a sudden acceleration of the corrosion process, see Figure 9.

4.4 Corrosion products

Metals or alloys can form several types of corrosion products. Which type(s) is largely dependent on temperature (see Ellingham diagram in subchapter 4.1), the environment (gas composition, present compounds etc.) and the chemical composition of the alloy. As was described in the previous subchapters, metals are generally thermodynamically unstable in an oxygen containing environment in which the respective metal oxides are thermodynamically stable. Therefore, depending on the metal or the chemical composition of the alloy, different oxides may form. These, along with other types of corrosion products, will be described in the following subchapters.

4.4.1 Oxides

Both at low and high temperatures metals and alloys form oxides. These can be seen as a natural protection against further corrosion. At low temperatures, the diffusion of ions through the oxide scale is slow and therefore, further corrosion is usually prevented. However, at high temperature the

diffusion through the oxide scale occurs at a much higher rate and the properties of the formed oxides is increasingly important to achieve a good corrosion behaviour. To behave protective at higher temperatures, the oxide should meet the following requirements [47]:

- Thermodynamically stable
- Highly stoichiometric – low defect concentration resulting in slow ion diffusivity
- Thermal expansion coefficient similar to the metal
- High melting temperature
- Well adherent to the alloy
- High plasticity at high temperature

The type of oxide that can form depends on the chemical composition of the alloy and the properties of these vary largely.

It is generally known that iron-based chromia (FeCr) forming alloys has to form a thin, adherent and slow-growing Cr-rich oxide while iron-based alumina forming alloys (FeAl, FeCrAl) has to form a thin and slow-growing Al and/or Cr-rich oxide in order to achieve a good corrosion resistance. It has been shown that the breakdown of the protective oxide results in a rapid formation of outward growing iron-rich oxide and inward growing spinel [48, 49]. This phenomenon is often referred to as breakaway oxidation (described in subchapter 4.3.4). The oxide prior to breakaway oxidation is usually called a protective oxide while the thick iron-rich oxide after breakaway oxidation is called a non-protective oxide. In this study, it has been shown that varying the amounts of certain alloying elements may have an effect on the growth rate of the "non-protective" oxide i.e. the protectiveness of the iron-rich oxide may be improved. The author has therefore decided to instead define two different stages of oxidation; **primary protection** (thin Cr/Al-rich oxide) and **secondary protection** (thick iron-rich oxide).

In the following subchapter, the most commonly occurring oxides, formed on iron-based and nickel-based chromia and alumina formers, will be described.

4.4.1.1 Iron oxides

Iron can form three different types of oxides: wüstite ($Fe_{1-y}O$), magnetite (Fe_3O_4) and hematite (Fe_2O_3). All three of these oxides have different crystal structure which largely affect their properties. Wüstite has a rock salt structure (NaCl), magnetite has a spinel structure and hematite has a corundum structure.

Wüstite

Wüstite is only stable a temperatures above 570 °C and at very low oxygen activites. Wüstite is metal deficient, as is indicated by the formula ($Fe_{1-y}O$), and is therefore a p-type semiconductor. The crystal structure consists of cubic close-packed oxygen ions and iron ions occupying the octrahedral interstices. Due to the high degree of nonstoichiometry, the diffusion coefficient for wüstite is large and thus the oxide growth is rapid, resulting in a thick oxide scale at high temperatures [11]. For Cr-containing alloys, the wüstite formation is inhibited and may not form since the thermodynamical stability temperature is shifted to higher temperatures [50].

Magnetite

The crystal structure of magnetite is spinel. A spinel oxide consists of cubic close packed oxygen ions with metal ions occupying the tetrahedral and octahedral sites. Which of these sites that is occupied depends on the valency of the metal(s). Divalent metal ions occupy the tetrahedral sites while trivalent metal ions occupy the octrahedral sites. Since iron can be both in the divalent (Fe^{2+}) and trivalent (Fe^{3+}) state it can occupy both the tetrahedral and octahedral sites. In alloys containing several divalent and

trivalent elements (of similar size), a spinel-type solid solution may form when oxidized. In such an oxide, the divalent metal ions compete for the tetrahedral sites while the trivalent metal ions compete for the octahedral sites, resulting in a large range of combinations in element distribution. Examples of such spinel oxides are $(Fe,Cr,Ni)_3O_4$, $(Fe,Cr,Al)_3O_4$, $(Cr,Mn)_3O_4$ etc.

Magnetite has a higher degree of stoichiometry compared to wüstite, resulting in a smaller diffusion coefficient and a slower oxide growth rate. However, at higher oxygen partial pressures, magnetite is metal deficient (metal deficiency increases with temperature) and has oxygen excess at lower oxygen partial pressures [11]. Thus, magnetite behaves as a p-type semiconductor.

Hematite

The crystal structure of hematite is corundum. The corundum structure consists of hexagonally close-packed oxygen ions with metal ions occupying 2/3 of the octahedral sites [11]. Other examples of oxides that have a corundum structure is Cr_2O_3 and Al_2O_3.

Hematite has the highest degree of stoichiometry of all the iron oxides which results in the smallest diffusion coefficient of the different iron oxides [35] and therefore a low oxide growth rate. Thus, hematite is considered the most protective of the iron oxides. Being oxygen deficient, hematite is behaving as an n-type semiconductor in the range of 650-800 °C [11]. However, at higher temperatures, hematite behaves as a p-type semiconductor.

4.4.1.2 Chromium oxide

At high temperatures, the only solid form of chromium oxide that is stable is chromia, Cr_2O_3. Like hematite, it has a corundum structure with the oxygen ions being hexagonally close-packed with the Cr ions occupying the 2/3 of the octahedral sites. Due to its high degree of stoichiometry, chromia grows very slow even at elevated temperatures (up to 1000 °C) [11]. Thus, it is considered a protective oxide and is desired to form in high temperature applications to prevent further corrosion.

Measurements on bulk chromia have indicated that the defect structure is metal deficient, meaning that it will behave as a p-type semiconductor. However, it has been shown to behave as an n-type semiconductor at low oxygen partial pressures [51]. This suggests that closer to the oxide surface, where the oxygen partial pressure is higher, the chromia behaves as a p-type semiconductor but behaves as an n-type semiconductor close to the oxide/metal interface at which the oxygen partial pressure is low. [11]

Regarding corrosion protection, there are some disadvantages with relying the formation of a chromia layer depending on the environment the material is exposed to. In water vapour-containing environments, the chromia layer may be subjected to the phenomena known as Cr-evaporation in which the Chromia is depleted of Cr [7]. This may in turn result in the loss of the protective properties of the chromia layer. At elevated temperatures (above 900 °C) Cr-evaporation may occur in the absence of water vapour due to the volatilization of CrO_3 [52, 53]. In some applications, the material is exposed to alkali containing compounds. These tend to react with the Cr in the chromia layer, resulting in the formation of alkali chromates [8]. This is detrimental for the protective behaviour of the material as this may lead to the loss of the chromia layer. These phenomena will be further described in subchapters 4.5.1 and 4.5.2.

4.4.1.3 Aluminium oxide

The only stable form of aluminium oxide is Al_2O_3 which may exists in several variations. The most commonly occurring variations are the α- and γ-phases. γ-Al_2O_3 usually forms below 900 degrees and is a transient oxide (not thermodynamically stable). At 900-1000 °C, it transforms into α-Al_2O_3 which is

the only thermodynamically stable form of Al_2O_3. α-Al_2O_3 has a very high degree of stoichiometry due to its large bandgap and high lattice energy which results in a very low defect concentration [11]. Thus, the ions transport through the oxide is very slow even at elevated temperatures and results in a very low oxide growth rate. Due to this, the α-Al_2O_3 layer has a high corrosion resistance and prevents the metal/alloy from further corrosion.

α-Al_2O_3 has a corundum structure with hexagonally close-packed oxygen ions with 2/3 of the octahedral sites occupied by Al ions. Since both Cr_2O_3 and α-Fe_2O_3 has a corundum structure as well, the initial formation of these favours the nucleation of α-Al_2O_3 [34] which is one of the reasons why the combinations of Fe, Cr and Al in FeCrAl alloys are beneficial. α-Al_2O_3 is a highly inert oxide which is beneficial regarding corrosion protection in complex environment containing various corrosive compounds. As previously mentioned, Cr_2O_3 is sensitive towards water vapour and alkali containing compounds due to Cr depleting reactions. However, these reactions do not occur for α-Al_2O_3 and therefore generally remains protective in such environments as long as the oxide scale remain intact. However, the high temperature needed for the α-Al_2O_3 to form is a large drawback for applications involving temperatures below 900 °C in which the corrosion protection has to rely on the formation of other less corrosion resistant oxides.

4.4.1.4 Silicon dioxide

Small amounts of Si is commonly added to steels due to the positive effects on the corrosion properties. When exposed at high temperature, the Si-containing alloys has been shown to form SiO_2 (often amorphous) [54] in the form of a dense discontinuous or continuous layer. This layer may act as a diffusion barrier, inhibiting the transport of ions which in turn prevents further corrosion attack.

4.4.2 Chromates and metal chlorides

As mentioned in chapter 2, the combustion of biomass and waste results in a flue gas with high concentrations of alkali- and chlorine containing compounds. These are involved in corrosion reactions that are detrimental for the material lifetime of several important parts of the boiler. The mechanisms for these reactions will be further described in subchapters 4.5.2 and 4.5.3.

The presence of alkali-containing compounds, such as KCl, K_2CO_3, NaCl etc, is especially unfavourable to the performance of chromia forming alloys as the reaction between these results in the formation of alkali chromates. These forms as porous crusts on the surface (see Figure 10) and does not contribute to the protective behaviour but instead depletes the chromia of the Cr, eventually resulting in the loss of its protective properties.

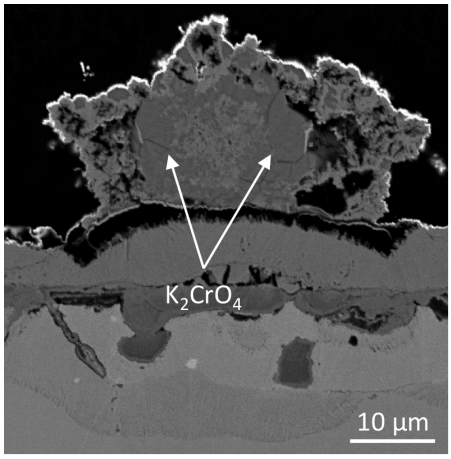

Figure 11: SEM-BSE cross section image of a crust of K_2CrO_4 formed after 168 hours of exposure in 5% O_2 + 20% H_2O + N_2 with KCl present.

The presence of chlorine species, at high temperatures, often leads to severe corrosion attack on surrounding metals and alloys. One of the corrosion products associated with this is metal chlorides, such as $FeCl_2$, $FeCl_3$, $CrCl_2$, $CrCl_3$ and $NiCl_2$. Which of these that are able to form depends on the alloy chemistry, chlorine activity as well as oxygen activity. Metal chlorides are formed at low oxygen partial pressures [55] and is therefore usually detected close to the oxide/metal interface, see Figure 11.

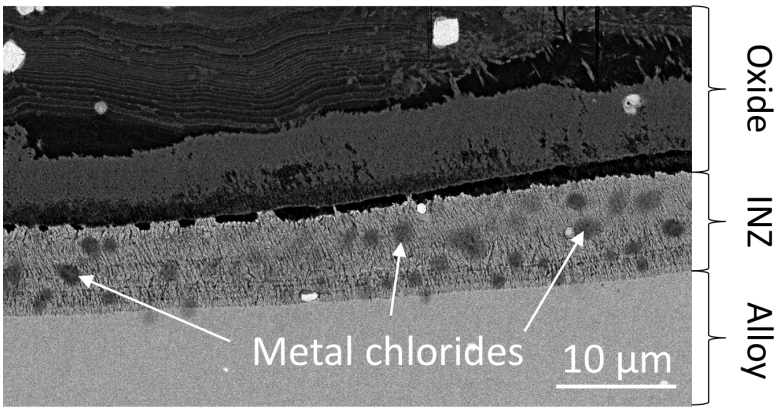

Figure 12: SEM-BSE cross section image displaying metal chloride formation in the internal nitridation zone on Fe5Cr3Al after exposure at 600 °C in the presence of KCl.

Due to their volatility and instability at higher oxygen activities, the metal chlorides often diffuse up through the oxide, causing them to decompose, which makes them difficult to detect and analyse.

4.5 Corrosion mechanisms

Depending on the environmental parameters that a metal/alloy is exposed to, various kinds of reactions may occur. Apart from the oxide formation, these reactions generally reduce the material lifetime by increasing the corrosion rate, break down protective oxide scales etc. In this chapter, some of the most important corrosion mechanisms associated with the environment in biomass- and waste-fired boilers will be described.

4.5.1 Chromium-evaporation

As mentioned in chapter 2, the flue gas in a biomass- and waste-fired boiler contain increased amounts of water vapour compared to the flue gas in coal-fired boilers. It is well known that the presence of water vapour drastically accelerate the oxidation rate of chromia forming steels [11]. Various hypothesis has been made about the involved mechanism regarding the corrosive effect of water vapour. However, the one which has become the most accepted in oxygen containing environments is the hypothesis involving the volatilization of chromium from the oxide [7, 56, 57]. In this mechanism, the protective chromia layer reacts with oxygen and water vapour to form chromic acid according to Reaction 4.3:

$$\frac{1}{2}Cr_2O_3(s) + \frac{3}{4}O_2(g) + H_2O(g) \rightleftharpoons CrO_2(OH)_2(g) \qquad \text{(Reaction 4.3)}$$

$\Delta G = 81.1 \frac{kJ}{mol}$, p($CrO_2(OH)_2$)=$2.97 * 10^{-7} atm$ (calculated with the following parameters and K_{eq} from Factsage; T=600°C, pO_2=0.05, pH_2O=0.2)

Despite the positive value of ΔG, this reaction has been shown to occur at significant rates at temperatures as low as 600 °C in systems with flowing gases. This is because the equilibrium is shifted

to the right when the chromic acid is transported away from the metal surface. As long as there is a balance between the evaporation of Cr and the diffusion of Cr from the alloy to the surface, the chromia will remain protective. However, if Cr-evaporation occurs at a higher rate than the alloy is able to resupply the surface with Cr, the reaction will eventually result in the breakdown of the protective chromia layer. This is followed by a rapid increase in oxidation rate as the faster growing iron oxide begins to form (for iron-based chromia formers). The transition between protective behaviour and rapid oxidation rate is commonly termed “breakaway oxidation”.

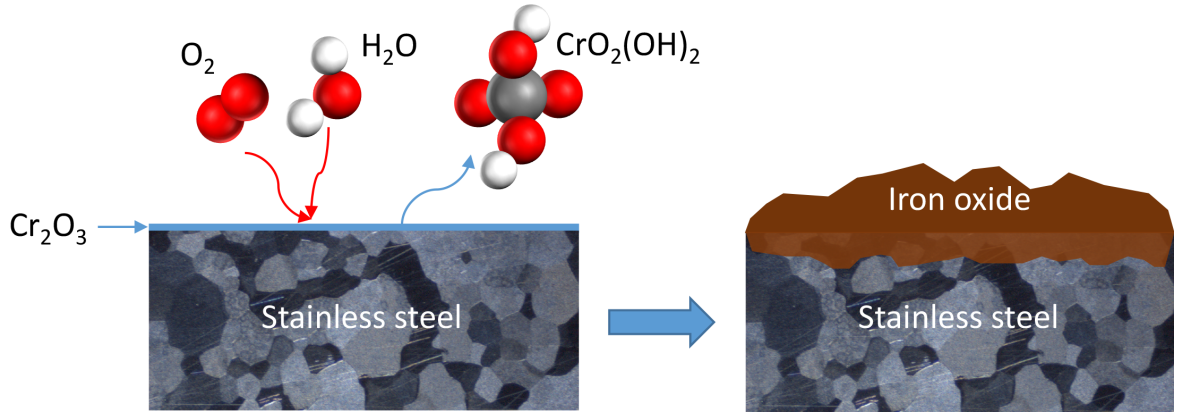

Figure 13: Schematic illustration of the breakdown of the protective chromia layer due to chromium evaporation on stainless steel.

4.5.2 Chromate formation

Another corrosion mechanism which also may break down the protective chromium-rich layer on chromia-formers is chromate formation. An explanation for this mechanism was done by Petterson et al [58, 59] which suggests that the alkali-containing species, such as KCl and K_2CO_3 reacts with the chromia layer to form K_2CrO_4 according to the following reactions:

$$\frac{1}{2}Cr_2O_3(s) + 2KCl(s) + H_2O(g) + \frac{3}{4}O_2(g) \rightleftharpoons K_2CrO_4(s) + 2HCl(g) \qquad \text{(Reaction 4.4)}$$

$\Delta G = 145.6\frac{kJ}{mol}$,p(Cl_2)=$1.04 * 10^{-6} atm$ (calculated with the following parameters and K_{eq} from Factsage; T=600°C, pO_2=0.05, pH_2O=0.2)

$$\frac{1}{2}Cr_2O_3(s) + K_2CO_3(s) + \frac{3}{4}O_2(g) \rightleftharpoons K_2CrO_4(s) + CO_2(g) \qquad \text{(Reaction 4.5)}$$

$\Delta G = 72.5\frac{kJ}{mol}$, p(HCl)=$9.87 * 10^{-4} atm$ (calculated with the following parameters and K_{eq} from Factsage; T=600°C, pO_2=0.05, pH_2O=0.2)

Similar to Reaction 4.3, the value of ΔG of reaction 4.4 is positive implying that the reaction is not thermodynamically spontaneous. However, the equilibrium vapour pressure of HCl is significant which means that in a system with flowing gas, such as areas exposed to the flue gas in biomass- and waste-fired boilers, the gaseous species (in this case HCl) are transported away from the metal which shifts the equilibria towards the right side of the reaction.

Formation of K_2CrO_4 result in depletion of the chromia layer which will eventually break down, leaving the metal/alloy unprotected which generally results in a rapid formation of thick iron oxide, see Figure 13.

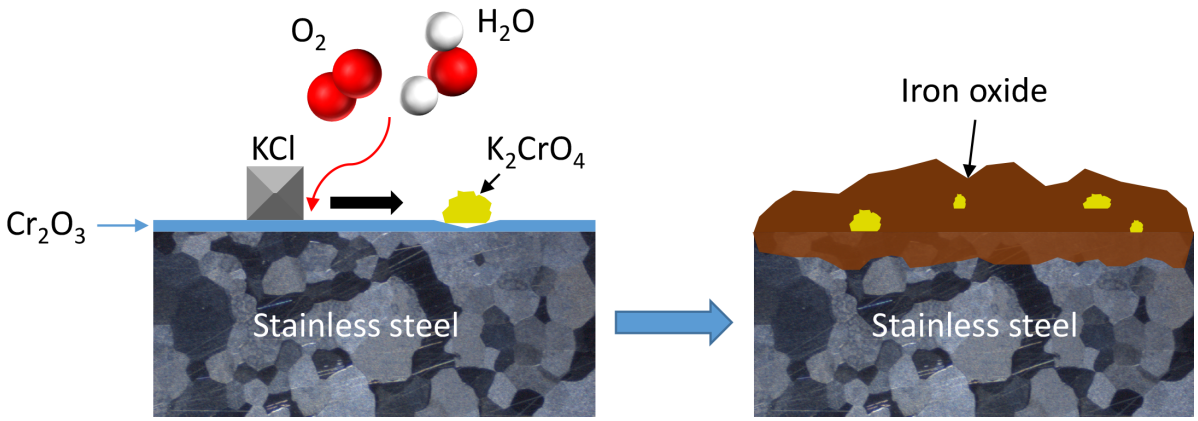

Figure 14: Schematic illustration of the breakdown of the chromium oxide due to formation of K_2CrO_4 in the presence of KCl.

4.5.3 Chlorine-induced corrosion

In addition to high levels of water vapour and alkali-containing compounds, large amounts of chlorine-containing species, such as KCl, NaCl, HCl and Cl_2, are present in biomass- and waste-fired boilers. It is generally known that these species negatively affect the high temperature corrosion resistance of metals, resulting in drastically accelerated corrosion rates. The mechanism involved has been investigated extensively over the years but is still not fully understood. However, a hypothesis called active oxidation (or chlorine cycle) has been suggested by McNallan et al [60] and further developed by Grabke et al [61]. According to their hypothesis, the mechanism is initiated by the transport of molecular chlorine, Cl_2, through micro crack and pores in the oxide scale to the oxide/metal interface. There, Cl_2 reacts with the metal according to Reaction 4.6:

$$\frac{x}{2}Cl_2(g) + Me(s) \rightleftharpoons MeCl_x(s) \qquad \text{(Reaction 4.6)}$$

where x is the valency of the metal ion. Metal chlorides such as $FeCl_2$ and $CrCl_2$ is only stable at low oxygen partial pressures which is why they form at the oxide/metal interface. However, at elevated temperatures, the vapour pressure of metal chlorides is fairly high and they are therefore believed to diffuse upward through the oxide scale. Along the oxide scale there is a gradient of oxygen partial pressure with the maximum value at the oxide surface and a minimum value at the oxide/metal interface. As the metal chlorides diffuse up through the oxide, they will eventually reach an oxygen partial pressure at which they are not stable. Thus, the metal chlorides will react with oxygen to form their respective metal oxides according to Reaction 4.7:

$$yMeCl_x(g) + \frac{z}{2}O_2(g) \rightleftharpoons Me_yO_z(s) + \frac{xy}{2}Cl_2(g) \qquad \text{(Reaction 4.7)}$$

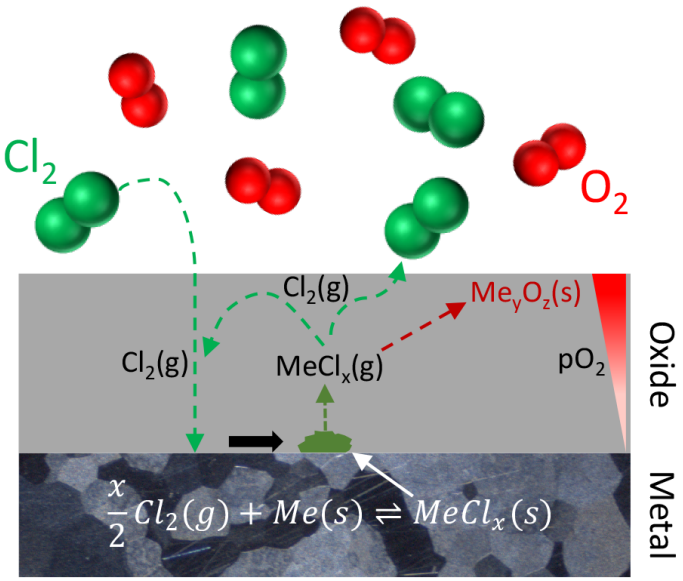

Figure 15: Schematic illustration of the active oxidation mechanism.

The Cl_2 released formed in Reaction 4.7 may either be released to surrounding atmosphere or diffuse back to the oxide/metal interface to begin a new cycle (from reaction 4.6) [61]. There is however some problems regarding the active oxidation mechanism. The hypothesis is based on the possibility of Cl_2 to diffuse through the oxide scale as well as a low oxygen partial pressure at the oxide/metal interface. If the cracks and pores in the oxide scale is large enough for Cl_2 to diffuse through, then O_2 molecules should be able to diffuse through the same cracks and pores since the molecular length of Cl_2 (396 pm) is larger than that of O_2 (264 pm). Thus, the oxygen partial pressure at the oxide/metal interface would become too high for the formation of metal chlorides to be favourable.

Another approach was suggested by Folkesson et al [62]. Compared to the previously mentioned hypothesis regarding the transport of molecular chlorine through the oxide scale, this approach involves the flux of anions and cations and an electronic current. It is suggested that, since Cl_2 is a strong oxidant and easily dissociates, it is reduced at the oxide scale surface which results in the formation of Cl^- ions, see Reaction 4.8. The electronic current needed for the reaction is provided by the oxidation of metal at the oxide/metal interface (Reaction 4.9).

$$Cl_2(g) + 2e^- \rightleftharpoons 2Cl^-(ads) \qquad \text{(Reaction 4.8)}$$

$$Me(s) \rightleftharpoons Me^{n+} + ne^- \qquad \text{(Reaction 4.9)}$$

Chloride ions may also be formed by the reduction of adsorbed oxygen and the simultaneous deprotonation of adsorbed HCl according to Reaction 4.10:

$$2HCl(ads) + \frac{1}{2}O_2(ads) + 2e^- \rightleftharpoons H_2O(g) + 2Cl^-(ads) \qquad \text{(Reaction 4.10)}$$

In the presence of oxygen and water vapour, alkali chlorides such as KCl may form chloride ions by reaction with water and oxygen according to the following reaction [63]:

$$2KCl(s) + \frac{1}{2}O_2(g) + H_2O(g) + 2e^- \rightleftharpoons KOH(g) + 2Cl^-(ads) \qquad \text{(Reaction 4.11)}$$

Grain boundaries can be regarded as inner surfaces in a polycrystalline material [64] due to the higher energy state of the atoms bonded along the grain boundaries as mentioned in subchapter 4.2.3.2. Thus the activation energy for diffusion is low along the grain boundaries. When the chloride ions has

formed and adsorbed on the oxide surface they are expected to have a high mobility compared to the oxide ions due to the smaller charge/radius ratio. Therefore, the diffusivity of chloride ions along the grain boundaries may be higher than for the oxide ions. The transport of chloride ions from the oxide surface to the oxide/metal interface via grain boundary diffusion agrees well with the formation of metal chlorides at the oxide/metal interface as this would remain an area with a low oxygen partial pressure.

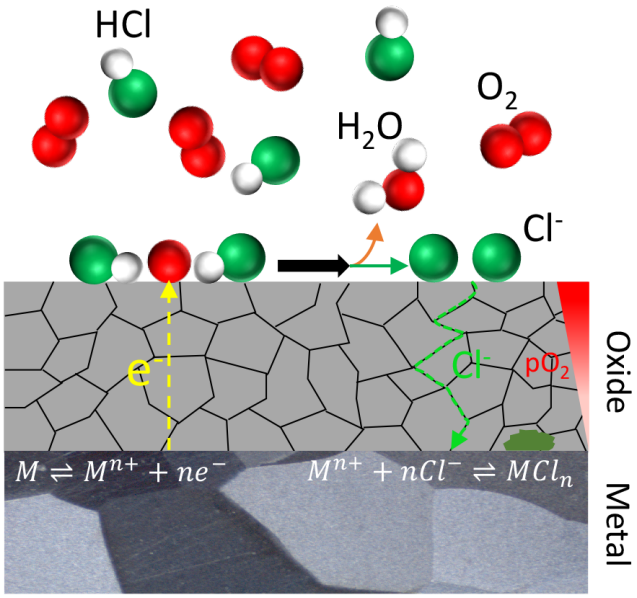

Figure 16: Schematic illustration of the chlorine-induced corrosion mechanism using the electrochemical approach.

5 Experimental Procedure

In this chapter the experimental procedures used in this study, including investigated materials, sample preparation, exposures and utilized analytical equipment, will be described.

5.1 Investigated materials

In this study, two different kinds of materials have been investigated, FeCrAl alloys and Ni-based coatings on a 13Mo3 substrate. The former consisted of model alloys which were produced to investigate the effects of one specific element, in this case Si. The alloy matrix is shown in Table 1. The Cr content of the alloys have been kept low compared to conventional FeCrAl alloys (about 20%Cr and 5%Al) since this is desirable for maintaining good mechanical properties.

Table 1: Nominal chemical composition (wt-%) of the FeCrAl model alloys.

Alloy	Cr	Al	Si	Zr
FeCrAl**0Si**	10	4	0	0.29
FeCrAl**1Si**	10	4	1	0.29
FeCrAl**2Si**	10	4	2	0.29

The alloys were produced first by melting in a vacuum induction furnace into a 1 kg ingot. This ingot was later hot-rolled into a strip and further machined to the get a thickness of about 2 mm. The strip was also heat treated at 950 °C to achieve a more even grain size distribution. All FeCrAl model alloys contained 10 wt% Cr and 4 wt% Al with a silicon content, varying from 0 to 2 wt%. An amount of 0.29 wt% of the reactive element zirconium was also added. The Cr content was kept low to reduce the negative effects on the mechanical properties associated with high Cr contents. Since the model alloys were iron-based and contained no nickel, they had a ferritic structure.

The Ni-based coatings were produced by HVAF-spraying as described in subchapter 3.2 using an HVAF gun (Uniquecoat M3^{TM}, Oilville, VA, USA) with the spraying parameters shown in Table 2 (based on preliminary coating tests, conducted in order to achieve the least porous microstructure).

Table 2: Spraying parameters for the Ni-based coatings

Variables	
Nozzle type*	3L2G
Air pressure, MPa	0.8
Fuel 1 pressure-Propane, MPa	0.7
Fuel 2 pressure-Propane, MPa	0.7
Carrier gas pressure-N_2, MPa	0.4
Feed rate, g/min	150
Pass velocity, m/min	50
Pass spacing, mm/rev.	5
Spray distance, mm	300
Number of Passes	8

Prior to spraying, the 16Mo3 substrates were grit blasted with alumina particles (63±10 µm) for cleaning and roughening the surfaces to ensure good adherence of the coating. A 16Mo3 rod with a length of half a meter was fixed in a horizontal rotating mandrel for applying the coating on the cylindrical surface. After the coating had been applied, the rod was cut into pieces of 5 mm thickness. The coatings were then applied on the flat faces of the cut pieces to ensure that the samples were coated on all sides, leaving no part of the substrate exposed. All coatings were sprayed to a thickness of roughly 250 µm.

The compositions of the coatings as well as the substrate is shown in Table 3 and Table 4. Three different coatings chemistries were selected, NiCr, NiAl and NiCrAlY to investigate the performance of a chromia forming coating, an alumina forming coating and one which is both.

Table 3: Composition of the investigated coatings.

Powders	Chemical composition (wt%)				
	Ni	Cr	Al	Y	O
NiCr	78.6	21.3	-	-	0.1
NiAl	94.1	-	5.7	-	0.2
NiCrAlY	Bal.	21.2	7.3	0.9	0.2

Table 4: Composition of the substrate on which the coatings were deposited.

Substrate	Chemical composition (wt%)					
	Fe	Cr	Mo	Mn	Si	C
16Mo3	Bal.	0.1	0.3	0.5	0.3	0.15

5.2 Sample preparation

Before examining the performance in various corrosive environments, the investigated materials went through several sample preparation steps. These differed slightly between the FeCrAl model alloys and the coatings and will be described in the following subchapters.

5.2.1 FeCrAl model alloys

The heat treated FeCrAl alloy strips, mentioned in the previous subchapter, were cut into coupons with a dimension of 10x12 mm. The alloys were analysed with optical microscopy to examine the microstructure. Elongated grains were detected in the cross section of the coupons as shown in Figure 16a. Thus, a second heat treatment at 950 °C for one hour was performed to relax elongated grains the elongated grains, resulting in a the microstructure shown in Figure 16b. Even after the second heat treatment, the grain size varied slightly between different coupons of the same alloy and the average grain size of the alloys was in the range of 110 to 130 µm.

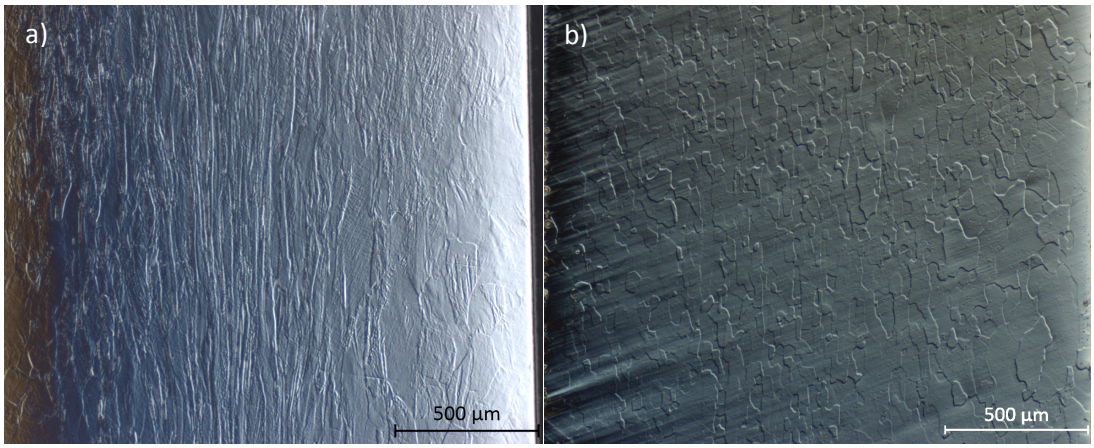

Figure 17: Optical microscope images of the cross section of FeCrAl0Si a) before and b) after second heat treatment.

A small hole with a diameter of 1.5 mm was drilled into the sample coupons to simplify weighing after deposition of salt. This hole was used to hang the sample on a hook while depositing the salt as well as in the balance, making it possible to weigh without removing any deposited. Prior to exposure, the sample coupons were ground with SiC paper (500 to 4000 grit) and then polished with a diamond suspension (3 µm followed by 1 µm) until a mirror-like surface had been achieved. To remove grease and dirt from the polishing, the samples were degreased with acetone and cleaned in an ultrasonic bath in separate tubes containing acetone. The samples were then cleaned with ethanol to remove any remaining acetone spots.

Prior to exposure, the samples were weighed to be able to record the mass gain. This was done differently depending on the exposure environment. In the absence of KCl, the samples were put in a Sartorius™ balance with microgram resolution where they were weighed. For the samples which were to be exposed in the presence of KCl the samples were hung on a hook in the same kind of balance. After weighing the sample, KCl was deposited on the sample surfaces by spraying a 20:80 water-ethanol solution, containing dissolved KCl, while continuously blowing warm air towards the sample to evaporate the solution. The samples were then weighed again to measure the amount of deposited KCl. This procedure was repeated until an amount of 1 mg/cm^2 had been deposited on the sample surfaces. KCl-sprayed samples were stored in a desiccator until right before exposure.

5.2.2 Coatings

After the coatings were sprayed onto the substrate the surfaces were coarse. Thus, to simplify analysis (gravimetry and microscopy) the surfaces were ground with SiC paper (500 grit to 4000 grit). The weighing of the samples was performed in a similar manner as for the FeCrAl model alloys but in a Sartorius™ balance with 5 decimal accuracy. No holes were made in the coated samples as this would expose the substrate. Thus, all samples were placed in the balance during weighing instead of hung regardless of the presence of deposited KCl. KCl deposition on the coated samples was carried out in the same way as for the FeCrAl alloys with the difference being that the sample was not hung in a hook during spraying.

5.3 Exposure

The high temperature corrosion tests were carried out in two different systems; a horizontal tube furnace and a thermobalance (TGA). These systems has different advantages and disadvantages. The horizontal tube furnace expose several samples at the same time, resulting in a large sample size for accurate analysis. However, only the final weight gain can be recorded from these exposures, meaning that there is information about the kinetics of the corrosion process. To achieve this, several exposures

of different intervals have to be performed. In the thermobalance, only one sample may be exposed at a time. Thus, the amount of samples from these type of exposures is very small. However, in a thermobalance, the weight of the sample is continuously measured during the exposure. Therefore, the kinetics of the corrosion process can be recorded for each sample. In the following subchapters, the procedure and the exposure parameters for the two different systems will be described.

5.3.1 Tube furnace exposure

The horizontal tube furnaces were equipped with silica tubes with an inner diameter of 45 mm. The silica tube was connected to several gas pipes through which various types of gases could be added. The flow rate of these gases could be controlled and was calibrated using a Bios Definer 220M to achieve a flow rate of roughly 3 cm/s. The silica tube was also connected to a membrane which was connected to a water bath and the gas pipes in order to mix the incoming gas with water vapour. The desired humidity was controlled by changing the temperature of the water bath. In this study, two different gas environments were used, 5% O_2 + N_2 (bal.) (FeCrAl alloys), 5% O_2 + 20% H_2O + N_2 (bal.) (FeCrAl alloys and coatings). To achieve the desired humidity, the temperature of the water bath was set to 60.4 °C. A schematic illustration of the tube furnace set-up is shown in Figure 17.

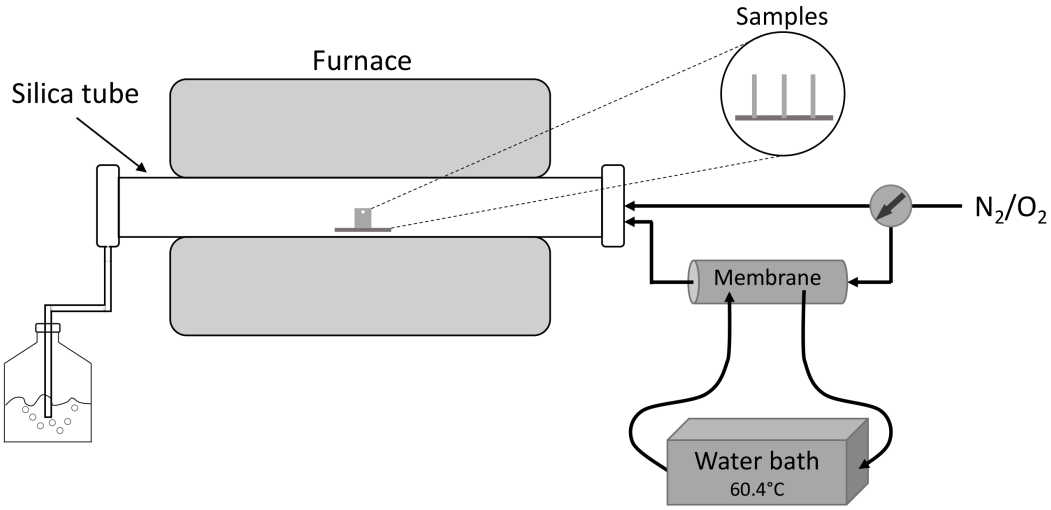

Figure 18: Schematic illustration of the tube furnace set-up used in this study.

Before inserting the samples, the gas flow parameters were adjusted and the furnace was heated up and calibrated so that the centre of the silica tube exhibited a temperature of 600 °C. The samples were mounted vertically in an alumina sample holder which differed between the FeCrAl alloys and the coatings. For the FeCrAl alloys, an alumina plate with three slits was used. Thus, three samples could be exposed at the same time (one sample per slit). For the coatings, two small alumina boats were placed on an alumina plate. The coated samples were then placed in the alumina boats (one in each boat). The sample holder, along with the samples, were then inserted to the centre of the silica tube before closing the system (with a silica end cap). For exposures with water vapour present, the valve was turned so that the gas passed through the membrane. The samples were left in the furnace for up to 168 hours before being taken out. The samples were then placed in the desiccator to prevent humidity from reacting with the corrosion products during cooling. After being kept in the desiccator for at least 12 hours, the samples were weighed in the same manner as described in subchapters 5.2.1 and 5.2.2 and a weight gain could be calculated.

5.3.2 Thermobalance exposures (TGA)

For the TGA exposures, a Setaram Setsys system connected to a Setaram Wetsys humidifier was used. A schematic illustration of the TGA system is shown in Figure 18. The exposures in the TGA system was

only performed for the FeCrAl alloys because of the size of the coated samples being too large as well as the absence of a hole for hanging the sample.

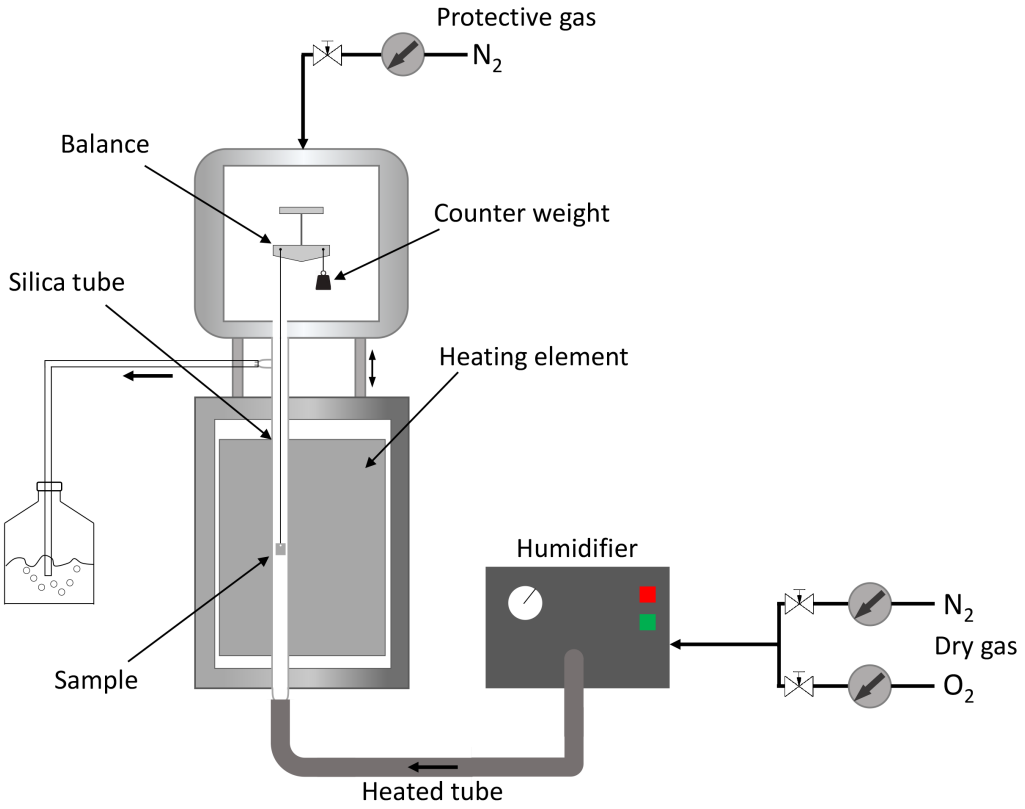

Figure 19: Schematic illustration of the TGA system used in this study.

The sample was hung on a platina hook before closing the system. The balance was calibrated by adjusting the counter weight so that the net weight was as close to zero as possible. The balance chamber is flushed for about 10 minutes before starting the exposure. When all cold spots in the TGA system had been insulated, the exposure program (600 °C, 48 hours) could be started. When the set temperature had been reached the relative humidity on the humidifier was set to 65%, resulting in a gas composition of 5% O_2 + 20% H_2O + N_2 (bal.). The gas flow rate was set to 15 ml/min which corresponds to about 0.3 cm/s (the inner diameter of the silica tube was 17 mm). The reason for the low flow rate in thermobalance compared to the tube furnace is that a higher flow rate will cause turbulence which can influence the quality and accuracy of the TGA measurement. All exposures in the TGA system in this study was performed with KCl deposited on the samples. After the exposure, the sample was taken out and left to cool in a desiccator. The samples were weighed in the same manner as described in subchapter 5.2.1.

5.3.3 Calculation of oxide thickness

Based on the weight gain of the exposed samples, theoretical oxide thicknesses were calculated. The calculation is based on the assumption that the total weight gain originates from the density change due to the ingress of oxygen. The theoretical density change is therefore given by Equation 5.1

$$\Delta\rho_{theoretical} = \rho_{M_xO_y} * \frac{M(O_2)}{M(M_xO_y)} \qquad \text{(Equation 5.1)}$$

where $\rho_{M_xO_y}$ is the density of the oxide and $M(O_2)$ and $M(M_xO_y)$ is the molar mass of oxygen gas and the oxide respectively. Utilizing the definition of density:

$$\rho = \frac{m}{V}$$ (Equation 5.2)

where m is the weight gain (g/cm^2) and V an arbitrary volume of the oxide, Equation 5.1 and 5.2 can be combined, resulting in Equation 5.3:

$$V\ cm^3 = d\ cm * 1\ cm^2 = \frac{m}{\rho_{M_xO_y} * \frac{M(O_2)}{M(M_xO_y)}}$$ (Equation 5.3)

where d is the oxide thickness of on an area of 1 cm^2. Thus, the oxide thickness in µm is given by Equation 5.4:

$$d = \frac{m}{\rho_{M_xO_y} * \frac{m(O_2)}{m(M_xO_y)}} * 10000$$ (Equation 5.4)

6 Analytical techniques

Apart from calculating the weight gain of the exposed materials, several analytical techniques were used to investigate the degree of corrosion attack, presence of corrosion products as well as determining underlying mechanisms. In this chapter the analytical techniques used in this study as well as the procedures will be described.

6.1 Microscopy

Visualizing the surface or cross section of a sample is of utmost importance for understanding the corrosion process and the underlying mechanisms. Oxide thickness, corrosion products, element distribution etc. give essential information about what has occurred during the exposure of the sample. The initial conditions of the material is of equal importance for which parameters such as grain size, surface morphology and present impurities can be studied.

6.1.1 Optical Microscopy

In optical microscopy the image is produced by utilizing photons directed towards the sample surface. The photons are reflected and refracted using lenses which results in a magnified image of the sample. In this study, a Zeiss AXIO Vert. A1 equipped with an AxioCam ICc 1 (with ZEN blue edition software) was used to examine the material prior to exposure to obtain information such as grain size and the general microstructure. It is possible to acquire a general overview of the corrosion products formed on the sample surface by using optical microscopy but it has certain limitations. The main limitation of optical microscopy is the comparatively large wavelength of the photons (390-700 nm) which results in images with a relatively low resolution. Thus, it is not possible to examine the corrosion products in detail. To acquire images with higher resolution it is therefore necessary to utilize other techniques which is not limited by large wavelengths. One such type of instrument is electron microscopes which utilizes electrons to visualize the sample surface.

6.1.2 Scanning Electron Microscopy (SEM)

An SEM is a type of microscope that utilizes electrons to visualize the surface of a sample and thus has a much higher resolution compared to optical microscopes. The SEM system consists of an electron source from which electrons are emitted and later accelerated in an electron gun. Before reaching the sample surface, the electrons pass through a system of magnetic lenses and apertures. The main functions of these are to focus the electron beam and make the probe size, i.e. the size of the surface area hit by the electron beam, as small as possible while keeping the current of electrons as high as possible [65]. The electron beam scans across the material surface to obtain information of a larger area. In the column as well as the sample chamber, it is important to maintain a high vacuum. If the vacuum is not high enough the electron beam would interact with present gas molecules.

When the electron beam hits the material, various important signals are generated and emitted such as secondary electrons (SE), backscattered electrons (BSE), and X-ray photons. Depending on the current of the incoming electron beam and the type of signal, the depth from which the signals are emitted differs [66], see Figure 19. Using different types of detectors these signals give different kinds of information.

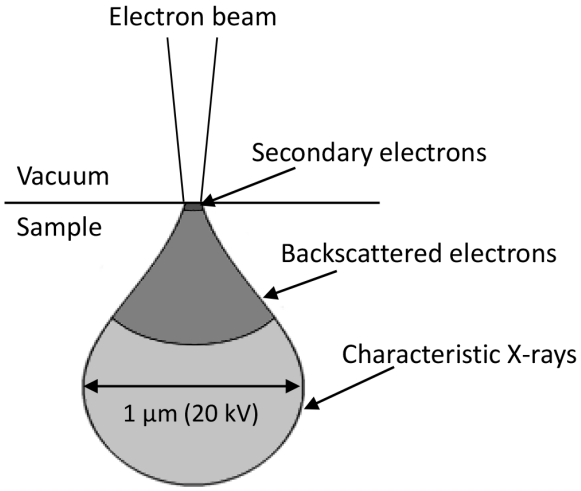

Figure 20: Illustration of the interaction volume from which the different signals are emitted when using SEM (Based on [65]).

The secondary electrons have a low energy (< 50 eV) and can therefore only escape from small volume close to the surface. Thus, secondary electrons give the best resolution of the three different signals. Edges of surface features on the sample emits more secondary electrons than flat surfaces which results in different contrast. Thus, the detection of secondary electrons is commonly used to visualize the topography of the sample surface [65].

Backscattered electrons has a higher energy than secondary electrons and can therefore escape from a larger depth which results in a lower spatial resolution. The amount of backscattered electrons emitted depends on, apart from the accelerating voltage (beam current), the composition, density, the presence of voids and the sample geometry [66]. A heavier material (higher atomic number) emits higher amounts of backscattered electrons. Thus, the detection of backscattered electrons is commonly used to visualize the distribution of different elements on the sample surface. A more porous area of the sample will appear in brighter contrast because less backscattered electrons are emitted. For crystalline samples, another mechanism can lead to differences in contrast, and is influenced by the orientation of the lattice. If the lattice is oriented in a way so that the incoming electrons encounter a low density of atoms, a fraction of these electrons will penetrate deeper into the crystal structure before being scattered [66]. Thus, the amount of backscattered electrons is reduced and a darker contrast will be displayed in this area. This type of contrast is called electron channelling contrast and can be observed on very smooth metal surfaces as the different grains are distinguished by different contrasts as the lattice orientation of the metal grain differs, see Figure 20.

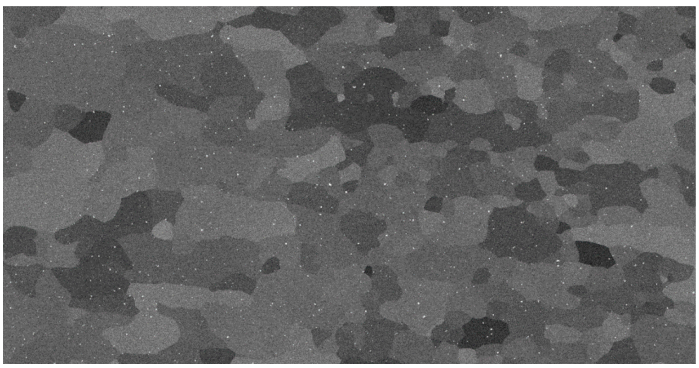

Figure 21: SEM-BSE image of a smooth metal surface. The grains are distinguished by the difference in contrast resulting from the different lattice orientations.

The third signal, X-ray photons, is different compared to the two other signals as it is not used to visualize the sample surface but instead to determine the elemental composition on the sample surface. The X-rays are produced when a high energy electron a large enough amount of energy to an atom to release an electron from an inner shell [65]. The atom can then relax by emitting energy in the form of an x-ray photon. The energy of the X-ray photon, emitted during the relaxation, is characteristic for the specific atom. Using an EDX (energy dispersive X-ray) detector, it is therefore possible to distinguish which elements are present on the surface. However, since the X-rays escape from an even larger depth than the backscattered electrons, the resulting resolution is even lower which makes it difficult to analyse the elemental composition of very small features [66].

In this study, an FEI Quanta 200 FEG ESEM equipped with an Oxford Instruments X-Max^N 80 T EDX detector was operated at 10-20 kV.

6.1.3 Broad Ion Beam (BIB)

Prior to analysing the cross sections of the samples in this study with SEM, they were prepared using Broad Ion Beam (BIB) milling. This results in a much smoother surface which reveals microstructural features and makes it possible to more accurately analyse the cross section. The BIB instrument used in this study was a Leica TIC 3X equipped with three argon guns. One side of the sample was first sputtered with a thin gold layer before attaching a silicon wafer with glue. After the glue was cured, the sample was then placed on a sample holder which in turn was placed on a stage in the BIB instrument, see Figure 21. The stage was adjusted so that roughly 0.1 mm of the sample was not covered by the mask. The instrument was operated at 6.5 kV for up to 12 hours.

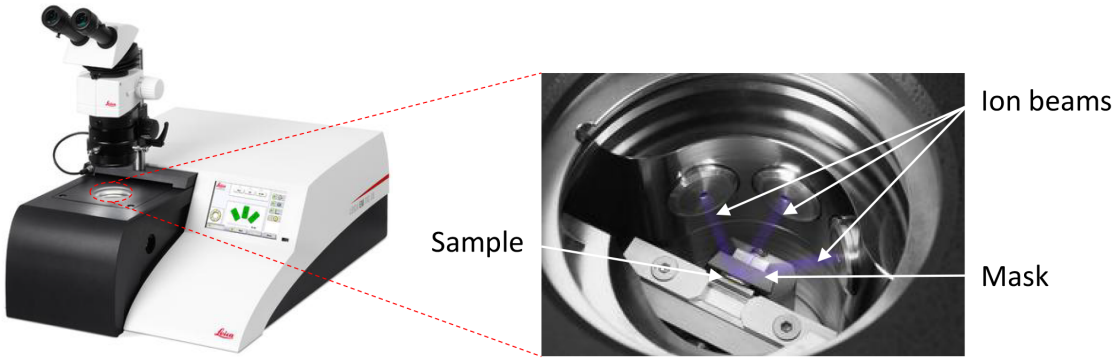

Figure 22: Picture of the BIB instrument used in this study (left). The picture to the right shows a sample attached on a sample holder which has been placed on the instrument stage. Three ion guns are directed toward the sample which is covered by a mask.

During the process, the ion beams mill the exposed part of the sample while the part of the sample covered by the mask remains unexposed as shown in Figure 22. This results in a smooth and clean surface which makes small microstructure features more distinguishable.

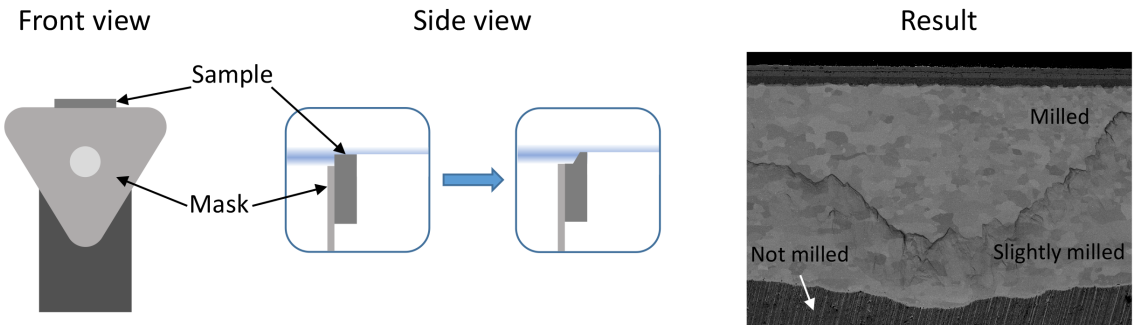

Figure 23: Schematic illustration of the BIB milling process (left) and SEM-BSE image of an exposed metal sample prepared with BIB milling (right). In the SEM image the degree of milling can be distinguished.

6.1.4 Focused Ion Beam (FIB)

In some cases, milling of a sample in a smaller and more specific area is desired. The reason may be to examine the cross section underneath a corrosion product on the sample surface or investigating the cause behind local differences in oxide thickness. This can be performed by using a Focused Ion Beam (FIB) workstation. In FIB workstation, ions are produced from an ions source and accelerated towards the sample surface. By using a high ion current and focusing the ion beam on limited area, it is possible to sputter away material in the same way as with the BIB instrument but in a more specific area. For high-accuracy milling the ion current has to be reduced since a too high ion current results in a wider distribution of the ions.

The FIB workstation can not only be used as a precision ion-miller but also as a microscope. When used as a microscope the same principle as the SEM applies, with the difference being that ions are accelerated towards the sample surface instead of electrons [65]. When the ions hit the surface it results in the emission of X-rays and secondary electrons. The number of secondary electrons emitted depends on the ion current accelerating voltage, composition of the examined area on the surface as well as surface topography. Detecting the emitted secondary electrons results in images with resolutions comparable to SEM images. A useful contrast mechanism when using a FIB workstation is the grain orientation contrast. When the ions interact with the crystals of the grains the amount of secondary electrons emitted is affected by the orientation of the crystals which makes the different grain distinguishable (more so than with an SEM). However, a disadvantage with visualizing the sample surface with ions is that they affect and damage the surface even when using a lower current [65].

In this study, a FEI Versa3D LoVac DualBeam FIB-SEM (with both an electron column and an ion column) was used by Amanda Persdotter to distinguish the oxide grains in order to examine the difference in oxide grain size for different samples, see Figure 23. The FIB-SEM was also equipped with an Omniprobe which and an ion and electron assisted Pt-deposition system. This makes it possible to perform in-situ lift out for TEM sample preparation. In this study, in-situ lift out for later TEM analysis was performed by Dr Vijayshankar Asokan.

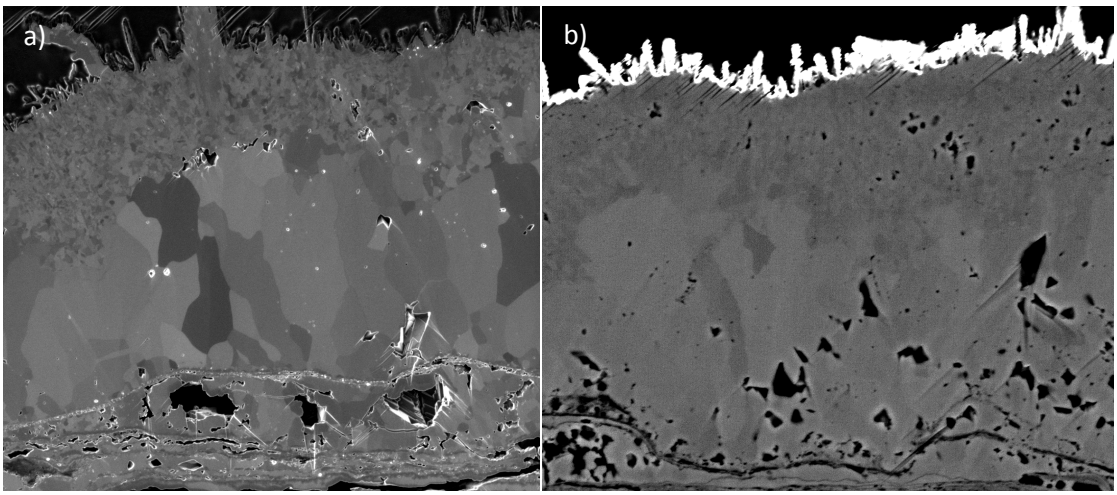

Figure 24: Two images of the same sample (not the same area), visualized using a) FIB (by Amanda Persdotter) and b) SEM. The oxide grains are more distinguishable when using FIB.

6.2 Transmission Electron Microscopy (TEM)

The principle of TEM differs from SEM in several important aspects. As with SEM, electrons are accelerated and directed towards the TEM-sample surface. However, contrary to SEM, most electrons are transmitted through the sample instead of being scattered back. It is the transmitted electrons which are detected to obtain detailed information about the sample. In order to be electron transparent the sample should be very thin, usually less than 100 nm in thickness. SEM analysis gives information about the specimen morphology, surface structure and chemical composition of the samples. With TEM analysis, information regarding the internal structure of the samples and crystal structure can be obtained as well. In addition, one of the main advantages is that small sample features can be analyzed in more detail due to the higher resolution.

In this study, TEM analysis was performed by Vijayshankar Asokan in order to investigate the nanometer thick oxides in more detail with higher magnification. TEM samples were prepared by performing lift outs (of about 100 nm thickness) of bulk specimens by utilizing a dual-beam FIB-SEM (FEI Versa 3D). After preparation of the lift outs they were fixed onto a Cu TEM grid. The imaging of the oxide layers on the TEM specimens were done using an FEI Titan 80-300, operated at 300kV in higher angle annular dark field- scanning transmission electron microscopy (HAADF-STEM) mode. The qualitative analyses of the elemental composition of the oxide layers were calculated from the energy dispersive spectra (EDS) using INCA X-sight, Oxford instruments.

6.3 X-ray diffraction (XRD)

A complementary method for performing chemical analysis is X-ray diffraction (XRD). Compared to many other types of chemical analysis, which indicate only the presence of the containing elements, XRD is able to disclose the presence of the specific compounds and/or phases on/in the examined sample.

The principle of XRD is based on the interference between X-rays scattered by atoms in a crystal structure. When an incoming beam of x-rays (commonly referred to as incident beam) reaches a crystalline material, they will interact with and be scattered by atoms. Because the X-rays consists of wave motions with certain wavelengths, these can interfere with each other, either constructive or destructive [67]. When two X-rays are in phase with each other, constructive interference occurs which results in them reinforcing each other and when the X-rays are out of phase, destructive interference occurs which results in them cancelling out each other, see Figure 24.

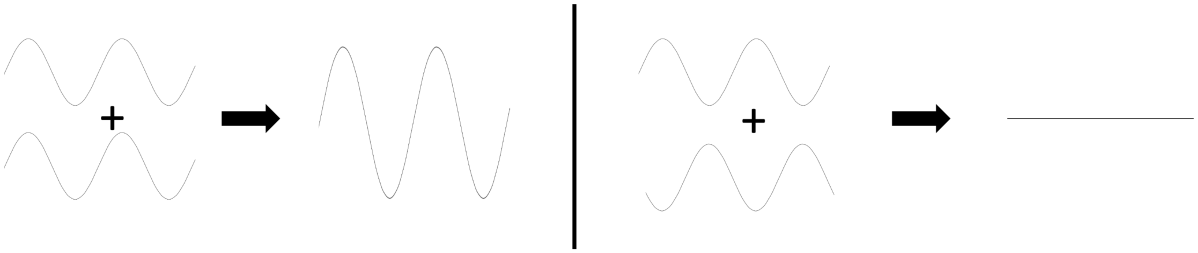

Figure 25: Schmetic illustration of constructive (left) and destructive (right) interference between waves.

A schematic illustration of the scattering of X-rays by atoms in a crystalline material is shown in Figure 25. The incident X-ray beam is scattered by atoms in three crystal planes (A, B and C). Since the atoms in the crystalline material are arranged periodically in a lattice there is a definite phase relation between the scattered waves [67]. Thus, for constructive interference to occur, the path difference, αβγ, of two X-rays has to be equal to a whole number n of the wavelength of the X-ray.

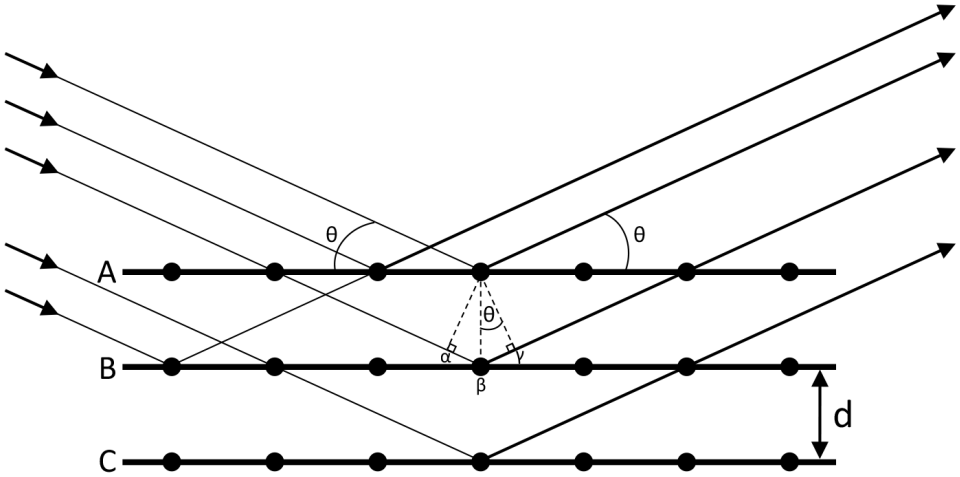

Figure 26: Schematic illustration of diffraction of an X-ray beam by atoms in several crystal planes (based on [67]).

The necessary conditions were mathematically expressed by W.L. Bragg in 1913 which resulted in Bragg's law:

$$n\lambda = 2d \cdot sin\theta \qquad \text{(Equation 6.1)}$$

where n is a whole number, λ is the wavelength of the incoming X-rays, d is the interplanar spacing in the lattice and θ is the incident angle of the incoming X-rays. Most incident angles results in a destructive interference.

When analysing a crystalline material with a diffractometer, the incident angle is slowly increased from one value to another. While varying the incident angle, the diffracted X-rays are detected and registered, resulting in a spectra. This spectra is characteristic of a specific compound or phase. Spectra of the vast amount of compounds have been recorded and stored in a database which is used when analysing the composition of unknown or partially unknown samples.

In this study, a Siemens D5000 diffraktometer was used as a complement to the chemical analysis performed with the EDX to analyse the corrosion products (mainly the upper oxide layers) of the FeCrAl alloys. The XRD program consisted of a locked couple scan ranging from 2θ=0° to 80°.

6.4 Thermodynamic modelling

A complementary tool for understanding mechanisms involved in the corrosion process is thermodynamic modelling. Thermodynamic modelling of material properties has been used for decades to predict stable phases in different systems [68]. The concept of this method is to define the conditions (basic thermodynamic properties such as temperature, composition of phases etc.) of the system in such a way that the degree of freedom equals zero. These are represented by mathematical expressions, usually in the form of Gibbs free energy. The equilibrium parameters of a system results in a minimum of Gibbs free energy. The Calphad approach used in computer software is based on this criteria; finding the Gibbs energy minima in a system and thus, the equilibrium phases, under defined conditions. Different software, e.g. Thermo-Calc and DICTRA, uses this method to evaluate thermodynamic properties by developed models in parallel with experimental data. Recent developments of models for Calphad software has enabled thermodynamic and kinetic modelling of some oxidation processes at high temperatures in simple environments (O_2) [69-71].

In this study, equilibrium thermodynamic calculations were performed by Sedigheh Bigdeli using Thermo-Calc to understand the effect of additions of certain elements to an alloy on the properties (such as composition) of the formed oxides.

7 Results and discussion

This study is divided into two parts. In the first part the effect on the corrosion behaviour of minor additions of silicon to FeCrAl alloys was investigated. In the second part the performance of HVAF-sprayed coatings in a highly corrosive environment at high temperature was investigated. The experimental procedures for these studies were presented in chapter 5. The results from the studies will be presented and discussed in the following subchapters.

7.1 The effect of silicon on the high temperature corrosion behaviour of FeCrAl alloys

The positive effect of minor additions of silicon to stainless steel as well as other corrosion resistant alloys on the corrosion behaviour has been recorded by several authors [17-20, 72-75]. The majority of the studies has been investigating this effect in the temperature range 700-1000 °C at which thin SiO_2 layers have formed. This layer is suggested to act as a diffusion barrier, preventing further corrosion attack. In many applications, the operating temperature is below this temperature range and it is therefore of interest to investigate if the effect of silicon addition still applies. In this study, the effect of minor addition of Si to FeCrAl alloys was investigated at 600 °C in three corrosive environments; O_2, $O_2 + H_2O$ and $O_2 + H_2O + KCl$.

After exposing the samples in tube furnaces for 168 hours, the mass gains from the oxidation reaction was recorded as described in subchapter 5.3.1. This data was plotted and resulted in the graph shown in Figure 26.

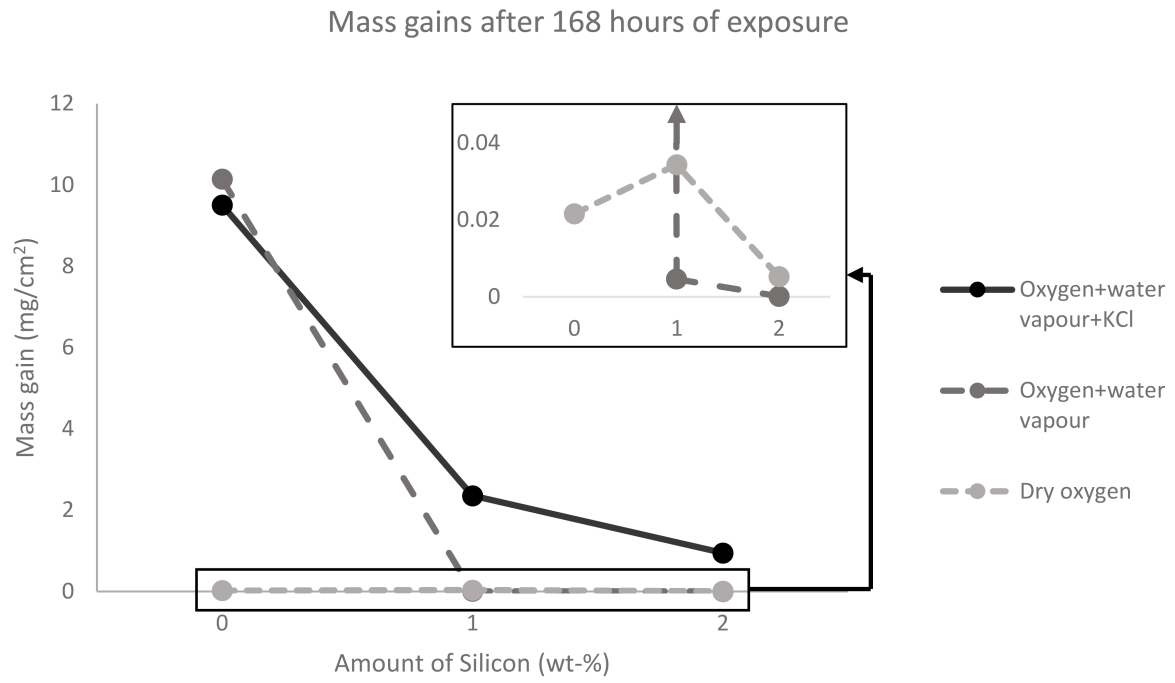

Figure 27: Mass gains plotted against silicon content of samples exposed in 5% O_2 + 20% H_2O + N_2 (Bal.) with and without KCl present as well as 5% O_2 + N_2 (Bal.) at 600 °C after 168 hours. The zoomed in box in the top-right corner shows the small differences between the low mass gain samples.

The graph gives a general overview of the effect of silicon in the three environments. The difference in corrosiveness between the environments is clear; the dry oxygen containing environment is the least corrosive and the O_2/H_2O environment with KCl present is the most corrosive. Strong effects on the corrosion behaviour, in terms of decreasing weight gain, is observed when adding Si to the alloys in the two O_2/H_2O containing environments. Minor effects can be observed in the dry oxygen

environment which is expected since even FeCrAl**0Si** has formed a protective oxide. In the upcoming subchapters, the gravimetry will be further discussed along with microstructural analysis.

7.1.1 Dry O_2 environment

Only minor effects on the weight change can be observed for dry oxygen environment in Figure 26. There is a slight increase in mass gain when adding 1 wt% Si but a larger decrease in mass gain when adding 2 wt% Si. This change correlates well with the SEM plan view images of the three alloys, see Figure 27.

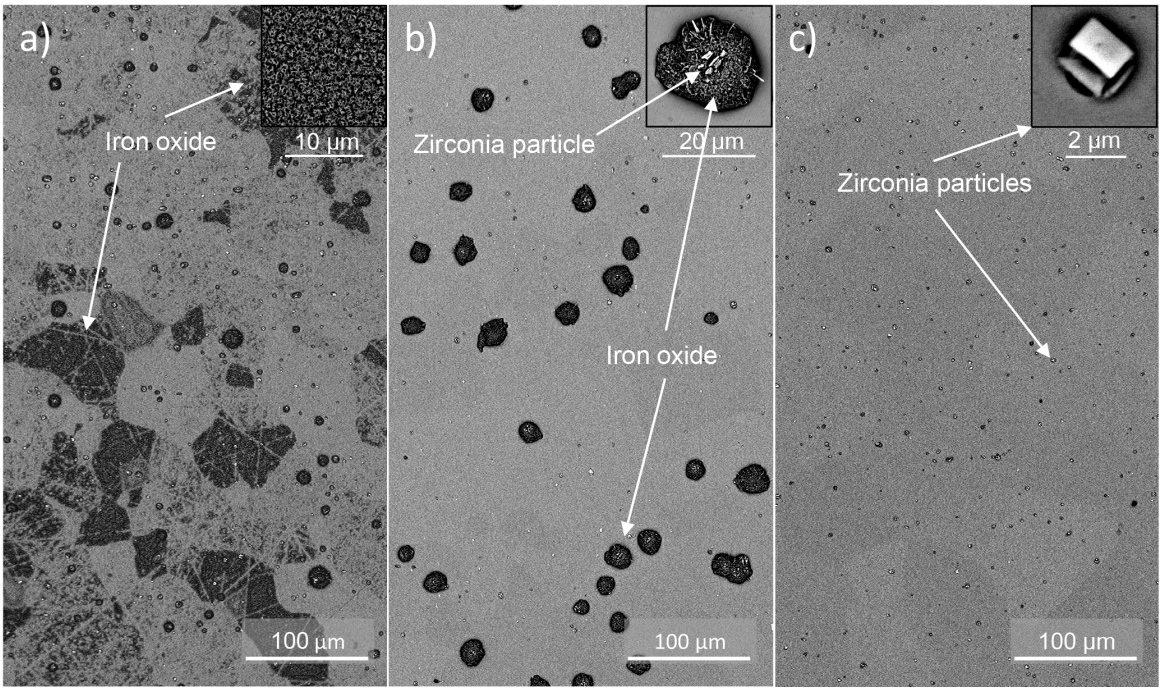

*Figure 28: SEM-BSE plan view images of a) FeCrAl**0Si**, b) FeCrAl**1Si** and c) FeCrAl**2Si** after exposure in 5% O_2 + N_2 (bal.) for 168 hours at 600 °C.*

As can be seen, FeCrAl**0Si** has formed thin iron oxide on some individual grain while other grains remains protective. This was not observed on the surface of FeCrAl**1Si** but instead iron oxide nodules has formed and is evenly distributed on the surface. This explains the slightly higher mass gain for FeCrAl**1Si** compared to FeCrAl**0Si**. The reason behind the formation of the iron oxide nodules in this mildly corrosive environment is unclear. However, examining the nodules closer reveals the presence of zirconia particles in the centre of the majority of the iron oxide nodules. This indicates that the presence of zirconia initiates the formation of the nodules. FeCrAl**2Si** has not formed any iron oxide regardless of the presence of zirconia particles but remains protective all over the surface which correlates well with the decrease in mass gain. The role of Si on this phenomenon is still unclear but is worth investigating more closely.

Since FeCrAl**2Si** only formed a thin protective oxide it was possible to calculate a theoretical thickness. Based on Cr_2O_3/Al_2O_3 the theoretical thickness was 32/42 nm. Based on previous studies, a chromia layer grows faster than an alumina layer [16, 76]. T. Jonsson et al. exposed a Fe-10Cr model alloy in dry oxygen at 600 °C for 168 hours [76] and found that the calculated chromia thickness was 90 nm which is roughly twice as thick as the oxide scale of FeCrAl**2Si**. H. Josefsson et al. exposed a commercial FeCrAl alloy (Kanthal AF) in 5% O_2 + N_2 at 600 °C for 168 hours which resulted in a roughly 40 nm thick oxide[16]. The composition of the oxide was analysed with AES and it was found that the oxide was Al-rich but also contained 6-9 at% Fe and 2-4 at% Cr. Comparing the calculated oxide thickness of FeCrAl**2Si** to those in the previously mentioned studies, indicates that the thin protective oxide of

FeCrAl**2Si** does not consist of $(Cr_x, Fe_{1-x})_2O_3$ but rather $(Cr_x, Al_{1-x})_2O_3$ and is Al-rich. To confirm these hypothesis, FeCrAl**0Si** and FeCrAl**2Si** were analysed in more detail using transmission electron microscopy and thermodynamic calculations.

Since a significant number of the grains on FeCrAl**0Si** were covered with iron oxide, it is of interest to investigate the difference between the protective grains and the non-protective grains. Figure 28 shows a TEM cross section of a less protective grain, covered with iron oxide.

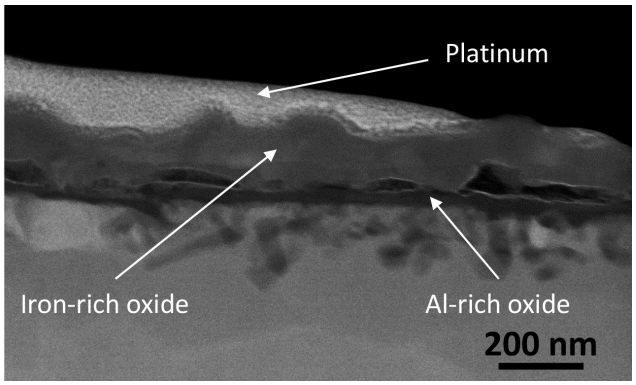

*Figure 29: STEM cross section image of the oxide formed on a non-protective grain on FeCrAl**0Si** after exposure in O_2 + N_2 at 600 °C for 168 hours. TEM analysis was performed by Dr Vijayshankar Asokan.*

As already indicated by the SEM-plan view image in Figure 27, an iron-rich oxide layer has formed on top of the grain with a thickness in the range of 150-200 nm. However, an underlying 40-50 nm thick layer was observed underneath the iron-rich oxide layer which according to EDS-analysis consists of pure Al-oxide. This may have formed after the initial formation of the iron-rich oxide and thus prevented further oxide growth. The protective grains, at which no iron-rich oxide had formed, was covered by a roughly 60 nm thick oxide, see Figure 29. EDS analysis (excluding oxygen) showed concentration gradients Fe, Cr and Al through the oxide, see Figure 29 (right). The oxide consists of different layers with varying concentrations. The concentration of iron is high in the outer part of the oxide but decreases drastically (to about 15 at%) when the Al and Cr content increases. The increased presence of Cr occurs at a lower depth than Al (the Cr and Al peaks are slightly shifted) and reaches a concentration of about 40 at%. At a slightly higher depth, the Cr content decreases and Al content increases to about 60 at%. Thus, the oxide consist of an outer iron-rich layer, followed by a Cr-rich layer and an Al-rich layer.

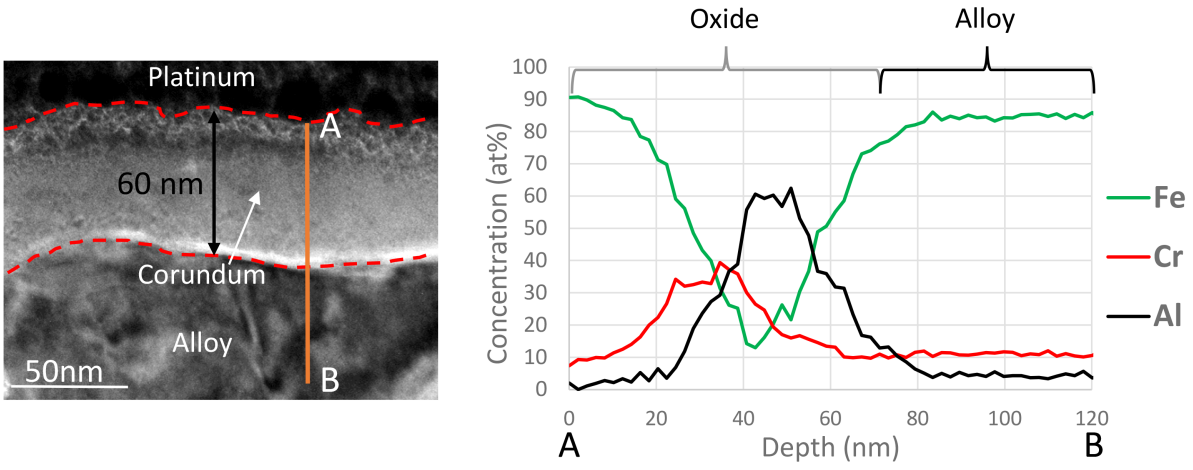

*Figure 30: STEM cross section image of the oxide formed on a protective grain on FeCrAl**0Si** (left) with EDS-data (right) after exposure in O_2 + N_2 at 600 °C for 168 hours. TEM analysis performed by Dr Vijayshankar Asokan.*

To better understand the reason behind the varying composition through the oxide, thermodynamic calculations of the corundum composition were performed for FeCrAl**0Si** (Figure 30). The calculations showed similar overall trends to the ones observed in the TEM/EDS-analysis, such as inner overlapping Al-rich and Cr-rich layers (low pO_2 in Figure 30) with an outer Fe-rich layer (high pO_2 in Figure 30). However, the calculated values of the element concentrations differed from the measured concentrations.

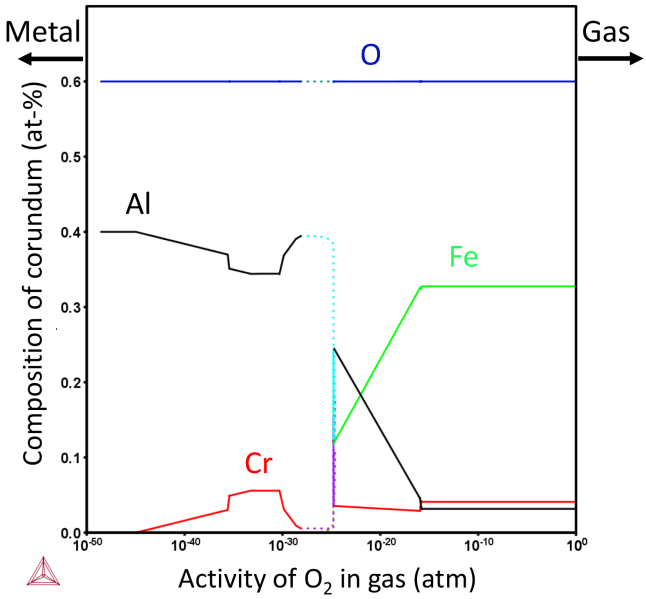

*Figure 31: Thermodynamic calculation of the composition of corundum against different activities of O_2 in gas for FeCrAl**0Si** performed by Dr Sedigheh Bigdeli using ThermoCalc. The dotted lines show a pO_2 region where corundum is metastable.*

FeCrAl**2Si** did not form any iron-rich oxide but only thin corundum oxide. TEM analysis showed that a continuous oxide with a thickness of 40-50 µm has formed (see Figure 31) which correlates well with the calculated thickness of 40 nm. Similar to FeCrAl**0Si**, the thin oxide of FeCrAl**2Si** consist of different layers but with some important differences. The outer part of the oxide consists of a thin layer (about 5 nm) of pure chromia which differs from the FeCrAl**0Si** alloy which formed an Fe-rich layer in the outer part of the oxide. This is followed by a drastic decrease of Cr and an increase in both Al and Fe, reaching levels of 70 at% and 30 at% respectively. The EDS data shows a peculiar behaviour as the Al and Fe contents varies periodically, switching from being Al-rich to Fe-rich and back to being Al-rich again. This indicates that the oxide consists of many layers with different compositions. The Fe-content is largely reduced in the inner part of the oxide while the Al-content is increased to almost 75 at%. Meanwhile, the Cr-content is increased to about 20 at%.

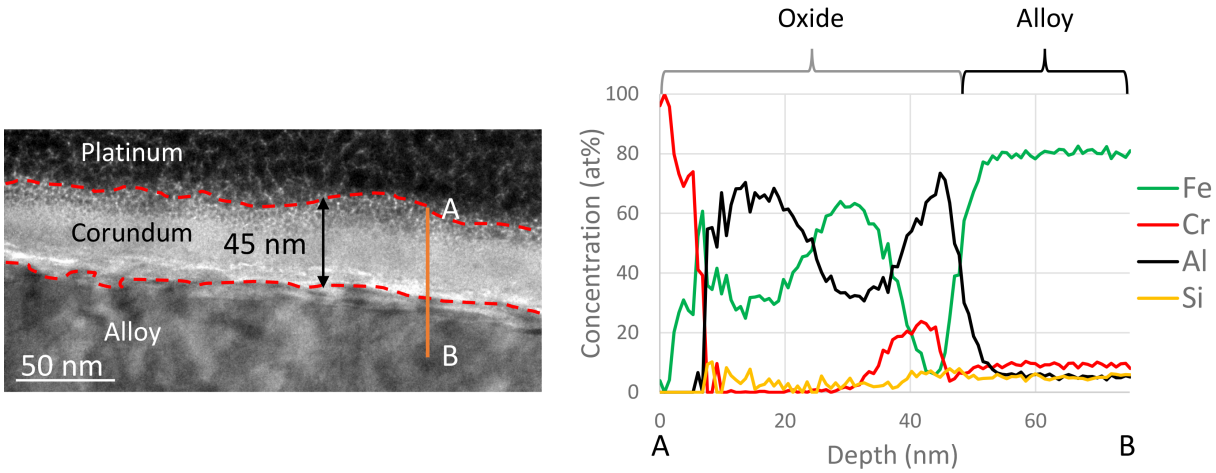

Figure 32: STEM cross section image of the thin protective oxide on FeCrAl2Si (left) with EDS-data (right) after exposure in O_2 + N_2 at 600 °C for 168 hours. TEM analysis performed by Dr Vijayshankar Asokan.

Similar to the thermodynamic calculations of the corundum of FeCrAl**0Si** the same calculations for FeCrAl**2Si** (Figure 32) correlates well with the measured composition in some aspects. The thermodynamic calculations suggests that there are an inner Al-rich layer and an outer Cr-rich layer which are separated which agrees well with TEM/EDS analysis. However, the thermodynamic calculations show that the corundum layer also consists of an outer Fe-rich layer which is not observed in the TEM/EDS analysis in which the iron seems to be incorporated in the majority of the corundum layer.

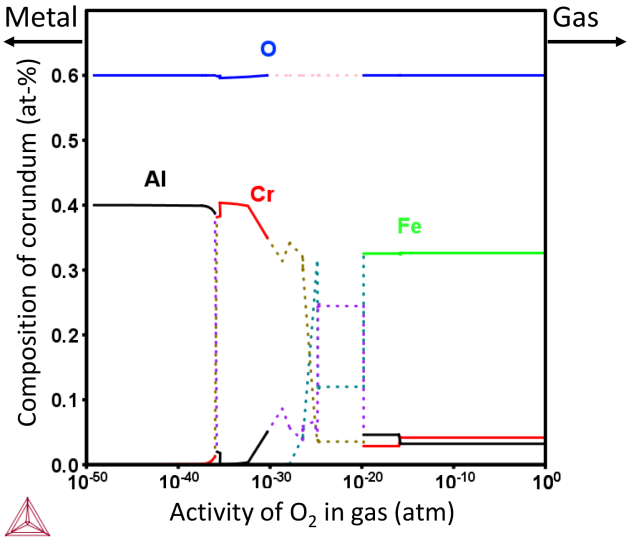

*Figure 33: Thermodynamic calculation of the composition of corundum against different activities of O_2 in gas for FeCrAl**2Si** performed by Dr Sedigheh Bigdeli using ThermoCalc. The dotted lines show pO_2 regions where corundum is metastable.*

The main differences between the corundum type oxide of FeCrAl**0Si** and FeCrAl**2Si** is the presence and distribution of Cr and Fe. The TEM/EDS analysis indicates that the addition of Si seems to push most of the Cr to the outer part of the oxide, leaving the rest of the oxide relatively free of Cr and more Al-rich. Another important aspect obtained by the thermodynamic calculations is that Si seems to reduce the pO_2 at which a pure alumina layer is formed.

Si-containing stainless steels have been shown to form a SiO_2 layer at the oxide/metal interface at elevated temperatures in similar environment (700-900) [17, 77]. However, no enrichment of Si could be detected by the EDS analysis which means no SiO_2 layer has formed.

7.1.2 O_2/H_2O environment

The presence of water vapour at high temperatures can be detrimental for materials which is dependent on the formation of a chromia layer for corrosion protection. This is due to the phenomenon known as Cr-evaporation, described in subchapter 4.5.1, which depletes the Cr in the chromia layer. This eventually results in the loss of the protective oxide and, in turn, rapid formation of iron-rich oxide.

Accordingly, FeCrAl0Si transitions from the primary protection stage when exposed in dry oxygen to the secondary protection stage when exposed in the presence of water vapour (O_2/H_2O) as it exhibits a large increase in mass gain, see Figure 26 . However, the corrosion behaviour in this environment appears to be largely affected by the addition of Si. Upon adding 1-2 wt% Si the mass gain is decreased to a value in the same range as when exposed in dry oxygen. This correlates well with the SEM analysis of the three alloys, see Figure 33.

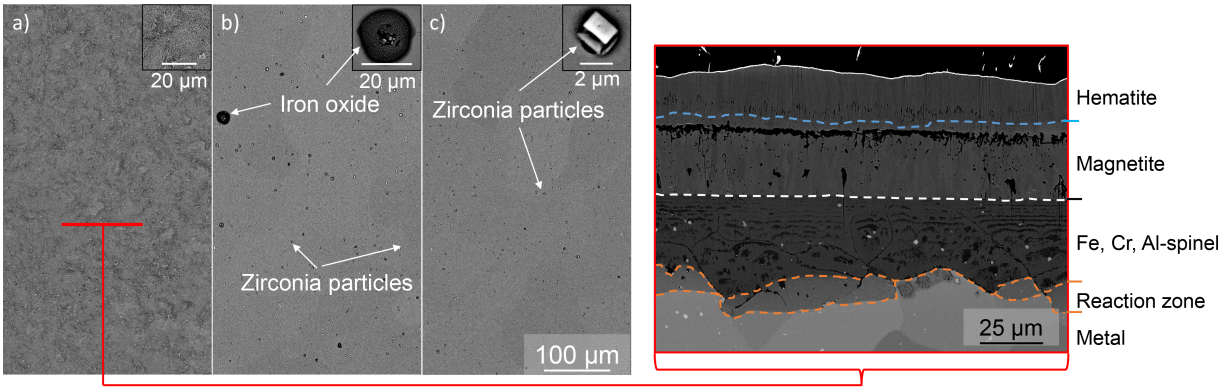

*Figure 34: SEM-BSE plan view images of a) FeCrAl**0Si**, b) FeCrAl**1Si** and c) FeCrAl**2Si** and a cross section image of FeCrAl**0Si** (far right) after exposure in 5% O_2 + 20% H_2O + N_2 (Bal.) without KCl present for 168 hours at 600 °C.*

The SEM analysis shows that FeCrAl**0Si** has formed a thick iron-rich oxide (80 µm thick), indicated by the rough surface morphology and confirmed by the cross section image. The iron-rich oxide of FeCrAl0Si consists of outward growing iron oxide (roughly 40% hematite and 60% magnetite) and an inward growing Fe, Cr, Al-spinel. Underneath the oxide, a reaction zone (internal oxidation zone) is observed which consists of about 60% oxide and 40% unreacted metal. This agrees well with studies performed by Jonsson et al. [48, 49] in which the propagation mechanisms of the oxide scale formed directly after breakdown of the slow-growing $(Cr_xFe_{1-x})_2O_3$ scale of iron-based stainless steels is described. The oxide after breakaway was shown to consist of outward growing iron-rich oxide (hematite and magnetite) and an inward growing Fe, Cr-spinel oxide/reaction zone. The reaction zone was shown to consist of Cr-rich oxide precipitates and Cr-depleted metal. Additionally, Jonsson et al. exposed a Fe-10Cr alloy in 5% O_2 + 20% H_2O +N_2(bal.) at 600 °C for 168 hours resulting in a total oxide thickness of about 80 µm, consisting of an outward growing iron-rich oxide as well as an inward growing Fe, Cr-spinel oxide. This indicates that the presence of Al/Re in the alloys does not influence the corrosion behaviour in the absence of Si. Neither FeCrAl**1Si** nor FeCrAl**2Si** has formed a thick iron oxide (apart from a few iron oxide nodules on the surface of FeCrAl**1Si**) and remains in the primary protection stage.

Since the main corrosive mechanism when adding water vapour to the oxygen containing environment is Cr-evaporation, these results indicate that the presence of Si in the alloys prevents the occurrence of this phenomenon. As mentioned in subchapter 4.4.1.4, a thin SiO_2 layer can form when a Si-containing material is exposed in an oxygen containing environment at high temperatures which may act as a diffusion barrier. However, the TEM analysis on the alloys exposed in dry oxygen shows no indications of the presence of a SiO_2 layer, see Figure 31. This indicates that the mechanism behind the large effect on the corrosion behaviour upon addition of Si is not due the formation of a SiO_2 layer.

Comparing the weight gains for FeCrAl**2Si** after exposures in the O_2 and the O_2/H_2O environments (see zoomed in box in Figure 26) a small difference is observed. The weight gain in the former is higher than in the latter which indicates that Cr-evaporation is still active with Si present. As was shown by the EDS analysis of FeCrAl**0Si** and FeCrAl**2Si** (see Figure 29 and Figure 31), addition of Si pushed most of the Cr to the outer part of the oxide (forming a roughly 5 nm pure chromia layer) while leaving the rest of the oxide relatively free of Cr and more Al-rich. This may explain why the Cr-evaporation is still active but does not result in the breakdown of the oxide when the alloy contain Si. When exposed in a water vapour-containing environment the oxide of FeCrAl**0Si** breaks down during Cr-depletion since Cr is largely incorporated in the entire oxide. However, when FeCrAl2Si is exposed in the same environment, the outer Cr-rich part of the oxide may be depleted while the remaining Al-rich oxide is left intact. The extent of the Cr-evaporation of FeCrAl2Si in 20% H_2O + air at 600 °C was measured for comparison with a pure chromia-former exposed in the same environment. For FeCrAl**2Si** an amount of 0.001 mg/cm^2 Cr had evaporated after 168 hours. Sand et al. showed that about 0.01 mg/cm^2 of Cr evaporated when exposing a pure chromia-forming alloy (NiFeCr alloy) for 90 hours. Thus, the extent of Cr-evaporation is one tenth compared to the value for a pure chromia-former. This agrees well with the previously mentioned hypothesis that only the pure chromia layer on FeCrAl2Si evaporates while leaving the rest of the oxide intact since the Cr-rich part makes up 10% of the whole oxide. This has to be confirmed with further TEM analysis. This is a distinct difference and further indicates that FeCrAl**2Si** has formed a more Al-rich oxide.

7.1.3 O_2/H_2O + KCl

Alkali salts such as KCl is highly corrosive at elevated temperatures and is one of the components in the flue gas of biomass and waste fired boilers responsible for the severely corrosive environment. The mechanisms behind the corrosivity of KCl and other alkali salts are described in subchapters 4.5.2 and 4.5.3. For ferritic stainless steels and other iron-based chromia-formers, the presence of KCl usually results in the loss of the primary protection and, in turn, a rapid formation of iron-rich oxide.

Accordingly, when the FeCrAl alloys in this study were exposed in this harsh environment, all specimens transitioned into the secondary protection stage, see Figure 26. FeCrAl**0Si** was barely affected by the presence of KCl since it exhibits roughly the same weight gain as in the absence of KCl (roughly 80 µm thick oxide) i.e. KCl has not effect on the secondary protection stage. Thus, when the primary protection is lost due to the presence of water vapour, the iron-rich oxide will grow at the same rate regardless of the presence of KCl. Upon adding Si to the alloy, the mass gain is drastically reduced but not to the same extent as in the absence of KCl (as the alloys have lost the primary protection). The gravimetrical analysis correlates well with the SEM analysis which confirms the loss of the primary protection and the drastic reduction in oxide thickness, see Figure 34.

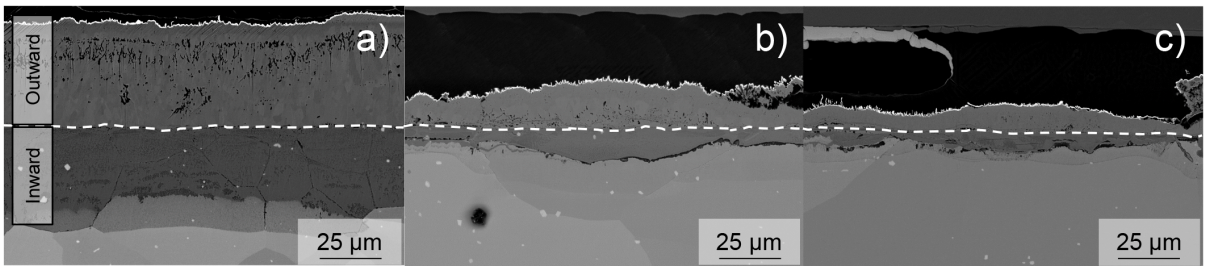

*Figure 35: SEM-BSE cross section images of a) FeCrAl**0Si**, b) FeCrAl**1Si** and c) FeCrAl**2Si** after exposure in 5% O_2 + 20% H_2O + N_2 (Bal.) with KCl present for 168 hours at 600 °C.*

All alloys has formed thick iron-rich oxide which grows both outward and inward (distinguished by the dashed line in Figure 34). Higher magnification images of the oxides are shown in Figure 35, Figure 36 and Figure 37 and displays the oxide layers formed. The microstructure of FeCrAl0Si after exposure in O_2 + H_2O in presence of KCl is similar to when exposed in the absence of KCl. However, the thickness of the hematite layer is significantly smaller in the presence of KCl (about 5 µm thick). A reaction zone has formed underneath the oxide in the presence of KCl as well.

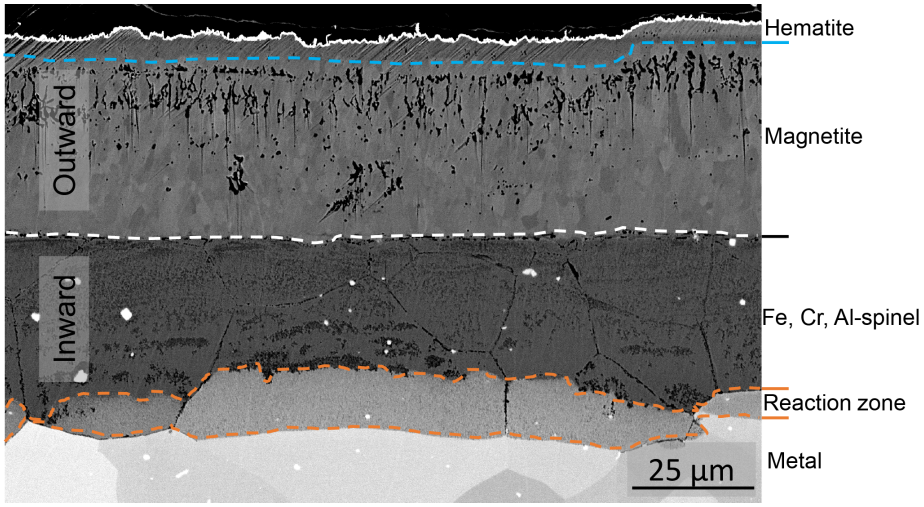

*Figure 36: SEM-BSE cross section image of FeCrAl**0Si** after exposure in 5% O_2 + 20% H_2O + N_2 (Bal.) with KCl present for 168 hours at 600 °C.*

The oxide scale of FeCrAl**1Si** is considerably thinner but has a similar microstructure. The hematite layer gives the impression that it is much thicker for FeCrAl**1Si** than for FeCrAl**0Si** but is actually in the same range (6-8 µm). Because the total oxide thickness is smaller, the ratio between the hematite and magnetite is 40:60. FeCrAl1Si also appears to have formed a reaction zone but EDX analysis as well as TEM analysis showed that the zone underneath the oxide scale is actually a nitridation zone, consisting of small Al-nitrides particles. This agrees well with a study by Israelsson et al. in which Kanthal APMT was exposed to the same conditions which resulted in the formation of Al-nitrides (confirmed with STEM/EDS). This indicates that nitrogen diffuses faster through the oxide scale compared to oxygen.

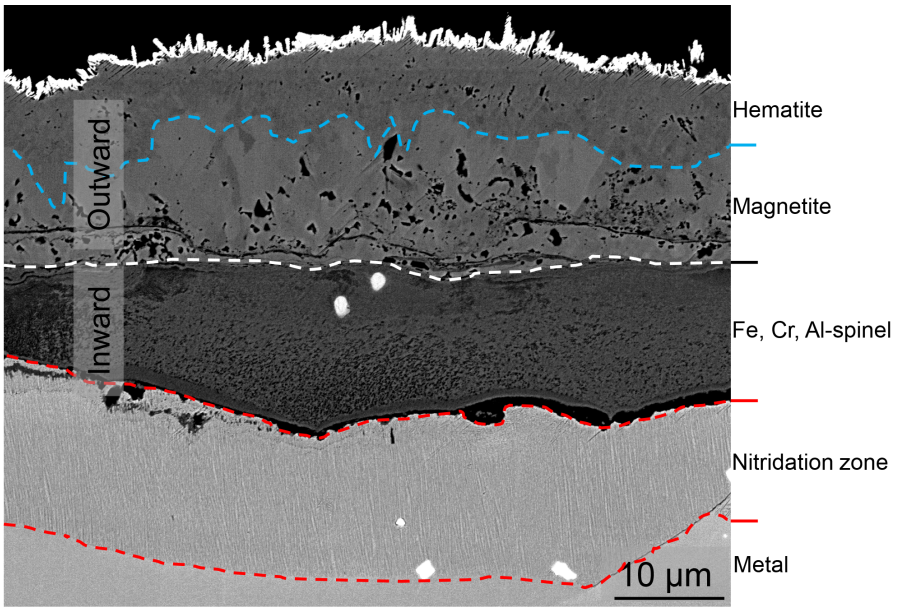

*Figure 37: SEM-BSE cross section image of FeCrAl**1Si** after exposure in 5% O_2 + 20% H_2O + N_2 (Bal.) with KCl present for 168 hours at 600 °C.*

The microstructure of the oxide scale of FeCrAl2Si differs slightly more. Apart from the reduced oxide thickness the outward growing oxide consists only of hematite which was confirmed with XRD analysis. However, the thickness of the hematite layer is still in the same range as those of the other alloys (5-10 µm). FeCrAl2Si also exhibits nitridation underneath the oxide scale but not to the same depth as FeCrAl1Si.

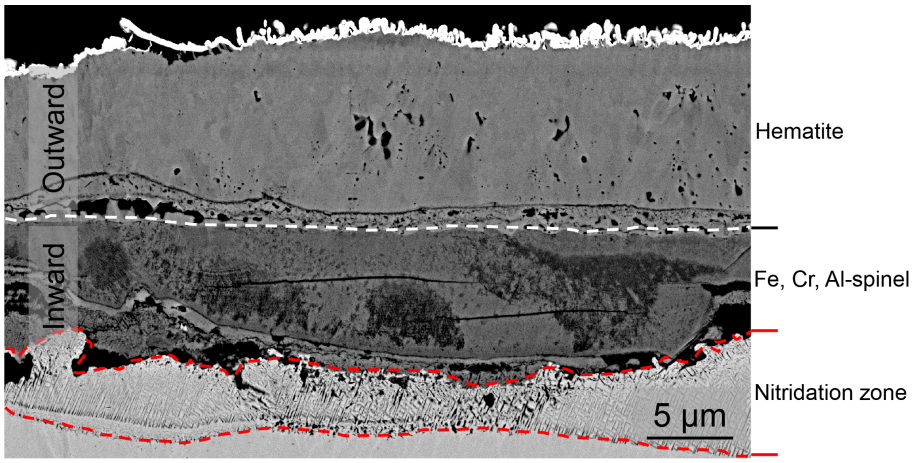

*Figure 38: SEM-BSE cross section image of FeCrAl**2Si** after exposure 5% O_2 + 20% H_2O + N_2 (Bal.) with KCl present for 168 hours.*

The calculated (based on magnetite) as well as the measured thicknesses of the different oxide layers of the alloys are summarized in Table 5.

Table 5: Measured and calculated (based on magnetite) oxide thickness of FeCrAl model alloys exposed in 5% O_2 + 20% H_2O + N_2 (Bal.) with KCl present for 168 hours at 600 °C.

Thickness of oxide scale (µm)			Outward growing		Inward growing
	Total (calculated)	Total (measured)	Hematite	Magnetite	Mixed spinel
FeCrAl**0Si**	67	67-80	5	37	25-38
FeCrAl**1Si**	17	19-32	6-8	5-9	8-15
FeCrAl**2S**i	7	8-19	5-10	0	3-9

No alumina or chromia layer could be detected during the SEM analysis after 168 hours of exposure for any of the alloys. It is possible that these has formed at an earlier stage of the exposure and broken down at a later stage.

When different alloys, capable of forming a protective oxide (alumina or chromia) exhibits different final mass gains it may be due to different incubation times i.e. the protective oxide is lost after different amount of times. To investigate the possible difference in kinetics, FeCrAl**0Si** and FeCrAl**2Si** was exposed in the thermobalance, resulting in the TGA measurement data shown in Figure 38. As can be seen, there are no significant incubation times for FeCrAl**0Si** and FeCrAl**2Si**. However, the corrosion behaviour differs significantly. The corrosion rate of FeCrAl**0Si** is much higher than that of FeCrAl**2Si**.

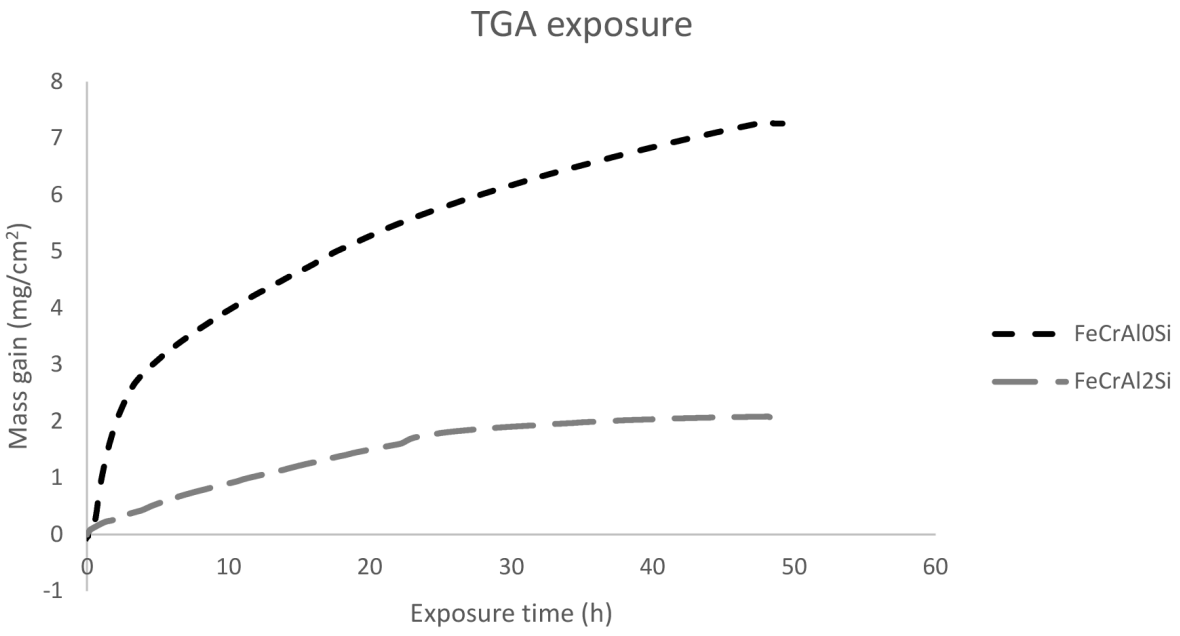

Figure 39: TGA measurement data after exposure in the thermobalance in 5%O_2 + 20%H_2O with KCl present at 600 °C for 48 hours.

Figure 39 shows the TGA measurement data from the first hour of exposure. The corrosion rate is the same for both alloys during the first 15 minutes before it drastically increases for FeCrAl**0Si** which remains fairly constant for FeCrAl2Si. However, already at this point of the exposure, both alloys have

transitioned into the secondary protection stage (relatively high mass gains). Thus, Si is affecting the oxide growth rate of the secondary protection stage.

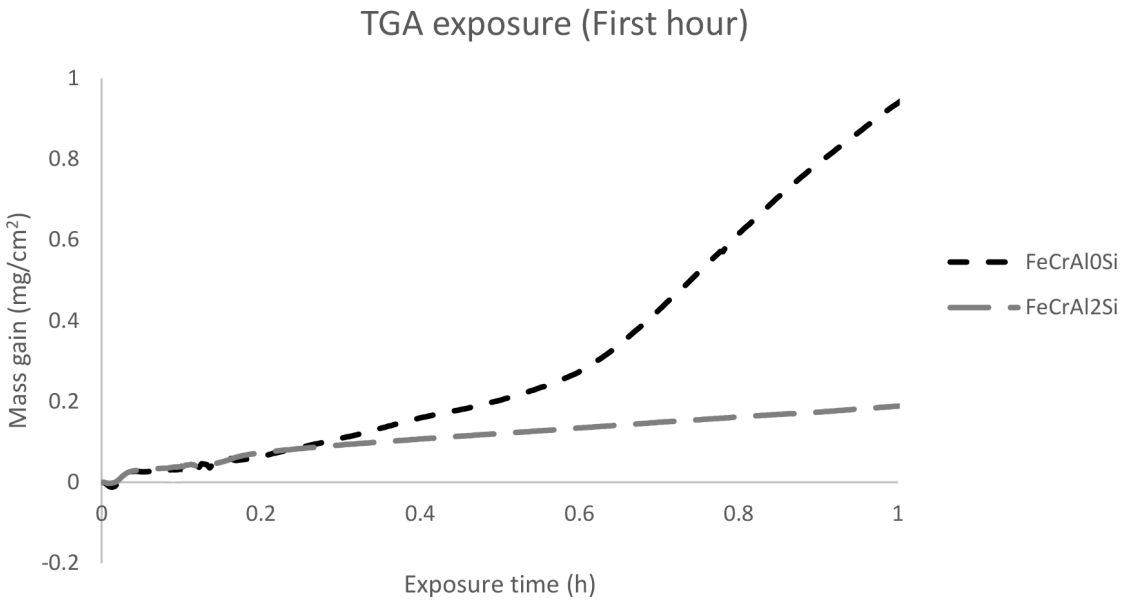

*Figure 40: TGA measurement data after the **first hour** of exposure in the thermobalance in 5%O_2 + 20%H_2O with KCl present at 600 °C.*

There are several possible mechanisms which could explain the influence of Si on the oxide growth rate. It is well known that Si containing alloys may form a thin layer of SiO_2 which may act as a diffusion barrier [17, 19, 72, 77], preventing further corrosion. Thus, SiO_2 is expected to form on FeCrAl**1Si** and FeCrAl**2Si**. This could result in a reduction of the ion diffusion rate through the oxide layer, resulting in a decreased oxide growth rate. However, upon analysing the Si-containing alloys using SEM/EDX, no continuous or discontinuous SiO_2 layer could be detected. As previously mentioned a SiO_2 layer is usually about 200 nm when formed at temperatures is the range of 700-900 °C [17] and may therefore not be possible to detect using SEM. However, TEM analysis also showed no presence of a SiO_2 layer. Thus, reduced growth rate upon addition of Si in not due to the formation of SiO_2, acting as a diffusion barrier.

The only area of the oxide with Si present is the inward growing spinel, confirmed by EDX analysis. The composition of the spinel analysed with the SEM-EDX is summarized in Table 6. It is possible that the diffusion properties of one or several of the elements in the spinel, such as the outward diffusion of iron or the inward diffusion of oxygen, is affected by the presence of Si in the spinel which would in turn affect the oxide growth rate. Another possible explanation is that Si absorbs inward diffusing oxygen which would result in reduced oxidation of the other alloying elements. If so, small SiO_2 particles would be dispersed in the inward growing spinel. This hypothesis has to be investigated further by performing more detailed TEM analysis of the spinel.

Table 6: Chemical composition (with oxygen excluded) from EDX analysis at 20kV in areas with dark and bright contrast in the spinel oxide for the model alloys.

	Composition in dark contrast area (at-%)						Composition in bright contrast area (at-%)					
Alloy	Fe	Cr	Al	Si	K	Cl	Fe	Cr	Al	Si	K	Cl
FeCrAl0Si	52.2	24.4	22.2	0	0	1.2	60.0	20.8	19.2	0	0	0
FeCrAl1Si	37.8	28.4	26.0	6.1	0.5	1.2	55.0	21.3	19.2	4.5	0	0
FeCrAl2Si	39.5	24.7	22.2	9.8	3.0	0.8	46.1	22.2	20.3	8.7	2.3	0.4

7.2 The performance of HVAF-sprayed Ni-based coatings in highly corrosive environments

The use of coatings on metal components for corrosion protection has been widely used over the years in a wide range of applications/environments. However, commonly occurring problem regarding the performance of the coatings includes high degree of porosity, oxide formation during spraying and poor adherence to the substrate. These problems usually result in the failure of the coatings to act as a corrosion protection [78, 79]. In more highly corrosive environments, such as biomass and waste boilers, in which high levels of water vapour and alkali chlorides are present, the defects in the coatings becomes increasingly detrimental. It is therefore of great importance to reduce these flaws in order to be able to utilize coatings in this kind of applications. More recently, a novel spraying technique was developed, HVAF (High Velocity Air-Fuel), which can produce denser coatings with better adherence [24, 25] (further described in subchapter 3.2).

In this study, the performance of three HVAF-sprayed coatings with different compositions were investigated by exposure to highly corrosive environments in tube furnaces followed by microstructural characterization as described in subchapters 5.3.1 and 6.1 respectively. In the upcoming subchapters the gravimetrical and microstructural analysis after exposure in the two corrosive environments (O_2/H_2O with and without KCl present) will be presented and discussed.

7.2.1 $O_2 + H_2O$

It has previously been showed that the HVAF coatings NiCr, NiAl and NiCrAlY succeeds in protecting the 16Mo3 substrate in ambient air at 600 °C as they form thin protective oxides on the surface [80]. Due to the high levels of water vapour in the flue gas in biomass and waste fired boilers, the understanding of the influence of water vapour on the corrosion protective performance of the coatings is of great importance.

As described in subchapter 4.5.1, Chromia forming steels often experience Cr-evaporation in the presence of water vapour at elevated temperatures due to the formation of chromium(VI) oxide hydroxide ($CrO_2(OH)_2$). It is therefore expected that the Cr-containing coatings in this study will experience a higher degree of corrosion attack in the presence water vapour. This agrees well with the weight change of the coatings after exposure in $O_2 + H_2O$ at 600 °C for 168 hours (Figure 40) which indicates that all coatings exhibits relatively high degrees of corrosion attacks. The red line in Figure 40 displays the mass gain of a bulk 304L sample which formed a thin Cr-rich layer in the nanometer range when exposed to the same conditions as the coatings. The calculated oxide thickness of the coatings, based on the weight gain, ranges from 0.6 – 1 µm which indicates that all coatings has lost the primary protection.

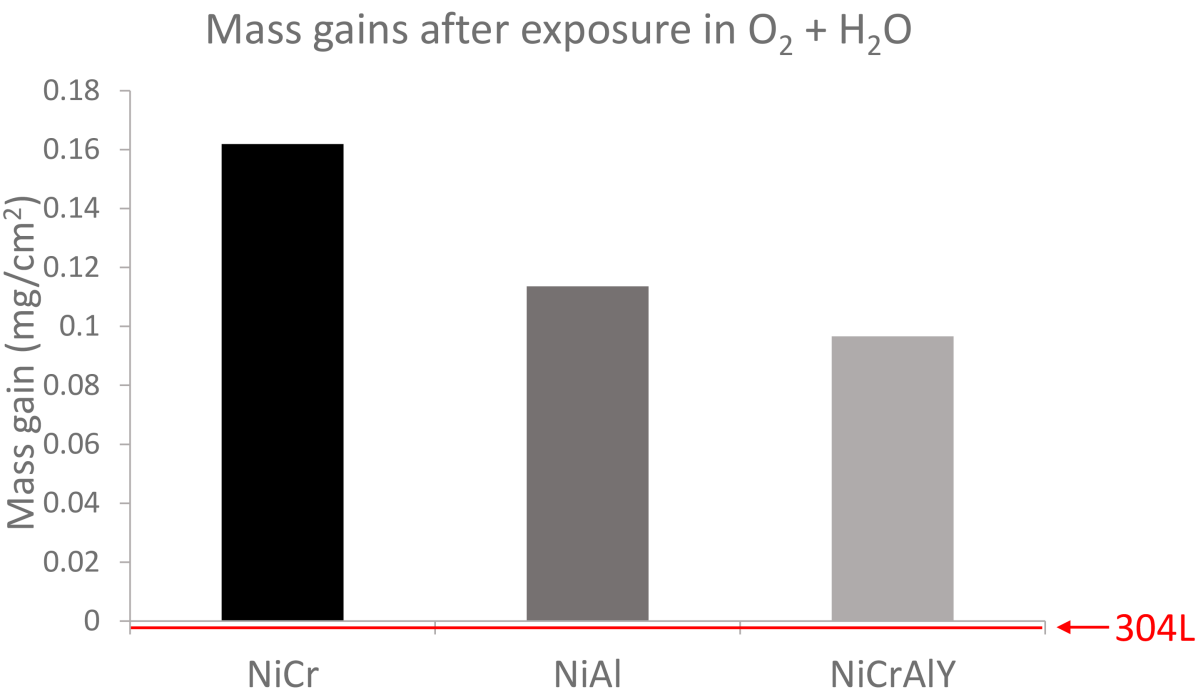

Figure 41: Mass gains of coated samples after exposure for 168 hours in 5% O_2 + 20% H_2O + N_2 at 600 °C. The red line displays the mass gain of a bulk 304L sample exposed to the same conditions.

However, upon observing the surface of the coatings the metallic lustre remained, indicating that the protective oxide has not been broken down. This was confirmed by SEM analysis in which no formation of thick oxide could be observed on the surface of any of the coatings, see Figure 41.

*Figure 42: SEM-BSE cross section image of the a) **NiCr**, b) **NiAl** and c) **NiCrAlY** coatings after exposure in 5% O_2 + 20% H_2O + N_2 at 600 °C for 168 hours. EDX map for oxygen added in bottom-left corner for each coating specimen. The dashed line shows the coating/substrate interface. Remaining Al-oxide from grit blasting of substrate observed at coating/substrate interface.*

All coatings display a significant degree of porosity mostly originating from splat boundaries. The NiCr coating exhibits larger pores while the NiAl and NiCrAlY coatings exhibits smaller pores evenly distributed in the coatings. Since the corrosive species are small, the lower diameter pores may still have a major negative effect on the corrosion protection of the coating as the corrosive species are able to penetrate the coating. Since the weight gain is not originating from the formation of a thick oxide on the surface of the coatings it is possible that oxygen has penetrated the coating through pores and other flaws, resulting in oxide formation inside the coating. EDX-analysis was performed for all three coatings to investigate the presence of oxides inside the coatings. The EDX-map for oxygen for each coating (see Figure 41) shows the presence of oxides inside the NiCr coating but not for the NiAl

and NiCrAlY coatings. Oxide formation may have occurred during the spraying of the coating, however the SEM analysis of an unexposed NiCr-coated sample showed no oxide formation, see Figure 42.

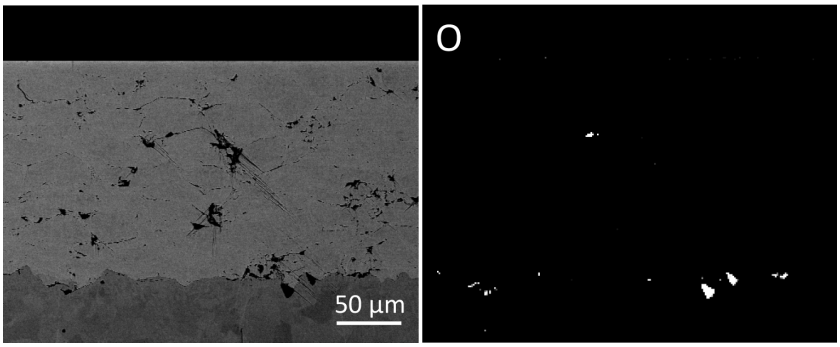

*Figure 43: SEM-cross section image of a non-exposed **NiCr** coated sample (left) and EDX map for oxygen (right) showing no oxide formation oxide formation in pores. The presence of oxygen in the coating/substrate interface originates from remaining Al-oxide from the grit blasting.*

Since all coatings have similar degrees of porosity, the oxygen penetration is expected to be in the same range. However, the severity of the porosity for the corrosion protection depends on the degree of open pores. If the majority of the pores are closed, the penetration of the corrosive species may not be as severe. It is possible that a higher degree of the pores in the NiCr are open compared to the pores in the other coatings.

The grain size may have significant effects on the protectiveness of the coatings since smaller grains could increase the diffusion rate of Cr and/or Al to the surface of the coating and facilitate the formation of Cr_2O_3 and Al_2O_3. The NiCr and NiAl coatings displays grain sizes in the range of 0.5-5 µm which is larger than the grain size of the NiCrAlY coatings (0.2 – 1 µm). Thus, the latter may be able to form a protective Cr_2O_3/Al_2O_3 faster which would prevent the penetration of oxygen. However, this does not explain why the NiAl coating does not exhibit oxide formation inside the coating while the NiCr coating does. The composition of the thin protective oxide may also be a contributing factor since a less Al-rich oxide will be more susceptible to Cr-evaporation. Regardless of the penetration of oxygen, all coatings managed to protect the substrate from being corroded for 168 hours.

A problem regarding coatings in high temperature applications is the interdiffusion of alloying elements from the coating to the substrate when the alloying chemistry between the coating and the substrate differ greatly [81]. This has been shown to cause a reduction of the amounts of corrosion resistance enhancing elements (such as Cr and Al) in the coating as well as reduced mechanical strength in the interdiffusion zone [82]. The latter can result in reduced pressure bearing capabilities and spallation of the protective coating. Since the substrate (16Mo3) used in the study was a low-alloyed iron based ferritic steel and the coatings were nickel based, all coatings exhibited a certain degree of interdiffusion after exposure in $O_2 + H_2O$ at 600 °C for 168 hours, see Figure 43 (occurred with KCl present as well). The driving force for the diffusion of nickel was especially high indicated by the EDX analysis which showed high levels of nickel to varying depths in the coatings. The interdiffusion zone of the NiAl sample contained the highest amount of Ni (40-50 at%), followed by the NiCr sample in which the interdiffusion zone contained 20-30 at% Ni. The interdiffusion zone of the NiCrAlY sample exhibited the lowest amount of Ni (8-12 at%) but reached deeper into the substrate compared to the other coatings.

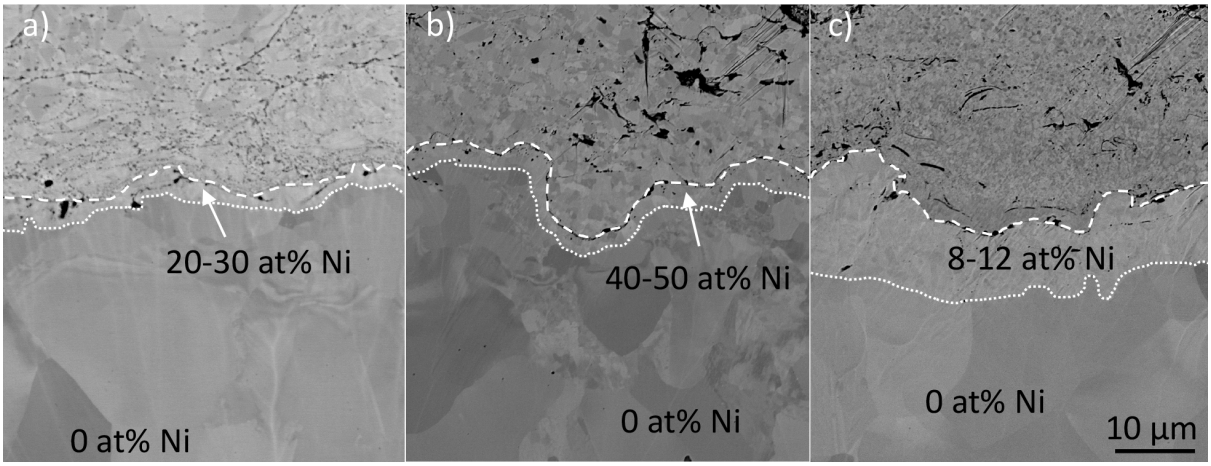

Figure 44: SEM-BSE cross section images of a) NiCr coating, b) NiAl coating and c) NiCrAlY coating, focused on the coating/substrate interface, after exposure in 5% O_2 + 20% H_2O + N_2 at 600 °C for 168 hours. The upper dashed line shows the coating/substrate interface. The lower dashed line shows the interface between austenitized (above)/ferritic (below) substrate.

Due to the high Ni content in the interdiffusion zones, austenitization occurs, i.e. the original ferritic phase in the substrate is transformed into an austenitic phase. This has earlier been shown to occur in high-Cr ferritic steels coated with metallic nickel [83]. Apart from the austenitization, the high-Cr steels formed brittle σ-FeCr phases which could lead to crack formation. Since the substrate used in this study contains very small amounts of Cr, the formation of σ-FeCr phases is not possible. However, austenitization can cause other mechanical problems due to the considerably higher coefficient of thermal expansion of the austenitic phase compared to the ferritic phase [84, 85] which may result in mechanical stresses during cycling and in turn, the spallation of the protective coating. The higher diffusion of nickel in the NiAl and NiCr coatings compared to the NiCrAlY coating can be explained by the higher Ni content in the former. This results in higher element activity gradient of Ni between the coatings and the substrate and thus a higher driving force for diffusion. In this study, no negative effects of the interdiffusion on the performance of the coatings, such as spallation or crack formation, was observed. However, since the exposures were isothermal and performed for a relatively short time, this phenomenon is of interest to study further by including thermal cycling and/or increasing the duration of the exposures.

7.2.2 O_2 + H_2O +KCl

As described in subchapters 4.5.2 and 4.5.3 chromia forming steels exhibit drastic acceleration in corrosion rate in the presence of KCl at high temperatures due to the loss of the protective chromia layer as it reacts with the KCl to form K_2CrO_4 and HCl according to Reaction 4.4.

Jafari et al. recently studied the corrosion behaviour of HVAF-sprayed NiCr, NiAl and NiCrAlY coatings in ambient air at 600 °C with KCl present for 168 hours [86]. It was shown that all three coatings managed to protect the substrate from corrosion attack during the time interval of the exposure. However, the corrosion protection differed significantly between the coatings. The NiCr coating formed an outward growing oxide as well as an inward growing oxide to a depth of roughly 30 µm. The NiCrAlY coating displayed less corrosion attack with only minor oxide formation dispersed in the upper part of the coating (to a depth of about 30 µm). The NiAl coating showed excellent performance regarding corrosion protection with no oxygen penetration and oxide formation inside the coating.

Since the combustion of biomass and waste results in a flue gas with high amounts of both water vapour and alkali compounds (such as alkali chlorides) [87, 88], the understanding of the corrosion

behaviour of the coatings in an environment containing both of these corrosive species is of utmost importance. Thus, in this study, the coatings were exposed in water vapour and KCl simultaneously.

Upon adding KCl to the O_2/H_2O containing environment the corrosion behaviour of the coatings changed drastically as shown in Figure 44. The NiCr coating exhibited a mass gain of roughly 2.4 mg/cm^2 which correlates to a theoretical oxide thickness of 17 µm (based on NiO). This is a large difference compared to when exposed in the absence of KCl, see Figure 40. The NiCrAlY coating also showed an increased weight gain when exposed in the presence of KCl but not to the same extent as the NiCr coating. The theoretical oxide thickness based on the weight gain of NiCrAlY is 3 µm. However, the NiAl coatings displays a different corrosion behaviour compared to the other coatings as it exhibits a weight loss after exposure in the presence of KCl. Weight loss during exposure is commonly due to Cr-evaporation. However the weight loss is too high to be explained by this. KCl has been shown to evaporate at significant rates in the present conditions. Thus, a more reasonable explanation for this phenomena is that the weight gain from the oxide formation on the NiAl coatings is much lower than the weight loss due to the evaporation of KCl. This indicates that the NiAl coatings only exhibits mild corrosion attack in this environment. Several 304L bulk samples were exposed in the same conditions and displayed large mass gains, exceeding those of both the NiAl and NiCrAlY coatings and shows similar behaviour as the NiCr coating.

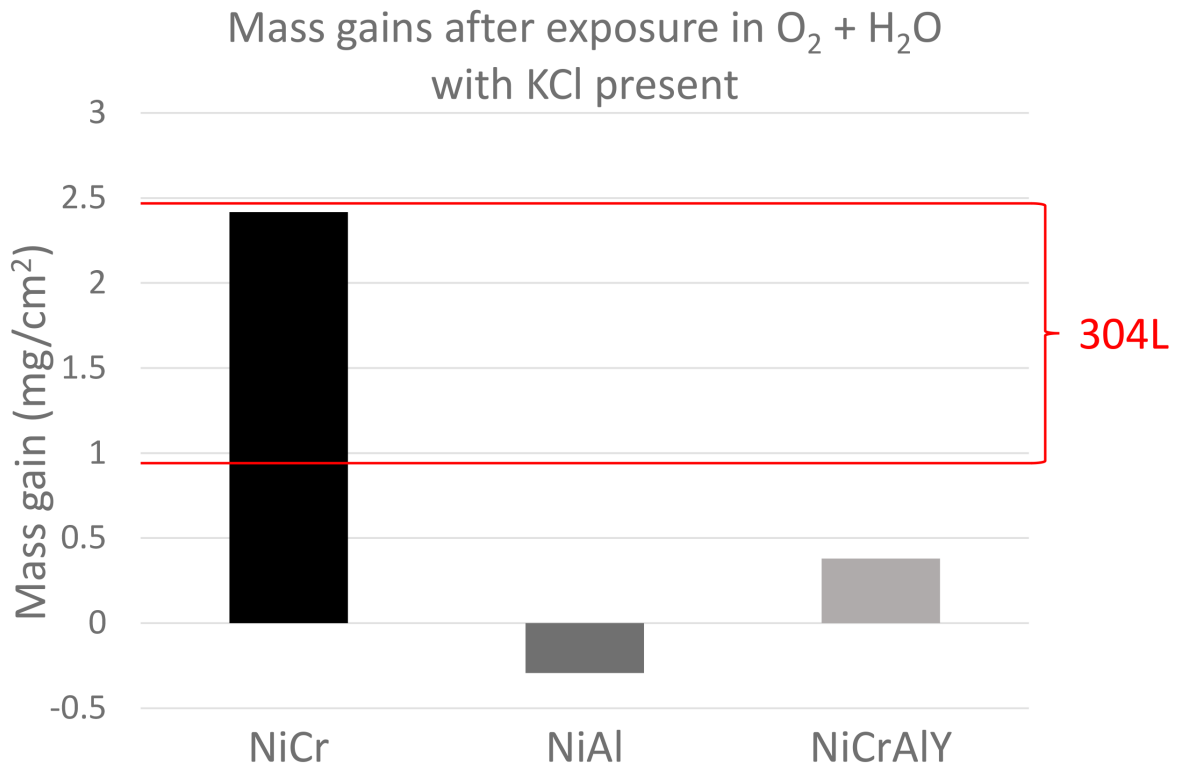

Figure 45: Mass gains of coated samples after exposure for 168 hours in 5% O_2 + 20% H_2O + N_2 at 600 °C with KCl present. The red lines display the mass gain range (based on measured oxide thickness) for a bulk 304L sample exposed to the same conditions.

SEM analysis showed that the NiCr coating had indeed experienced a severe corrosion attack in the presence of KCl, see Figure 45. A 30-50 µm thick outward growing oxide, containing both Ni and Cr has formed on the surface of the coating as well as a roughly 15 µm thick inward growing oxide, rich in Ni and Cr. Since the coating layer is relatively thick, the oxide is far from reaching the substrate. However, in addition to the oxide formation, cracks have formed in the coating and is seemingly originating from the splat boundaries. This can lead to further penetration of corrosive species through the coating

towards the substrate and may eventually result in spallation of large parts of the coating. The diffusion of Cl through the coating has occurred to a large degree indicated by the formation of metal chlorides (more specifically Cr-chlorides) close to the coating/substrate interface. The EDX-analysis indicates that the Cl diffuses through the coating along the splat boundaries, see EDX-map in Figure 45. In the magnified image to the right in Figure 45, Cl is detected at the coating/substrate interface which means that the NiCr coating is no longer protecting the substrate from the corrosive environment.

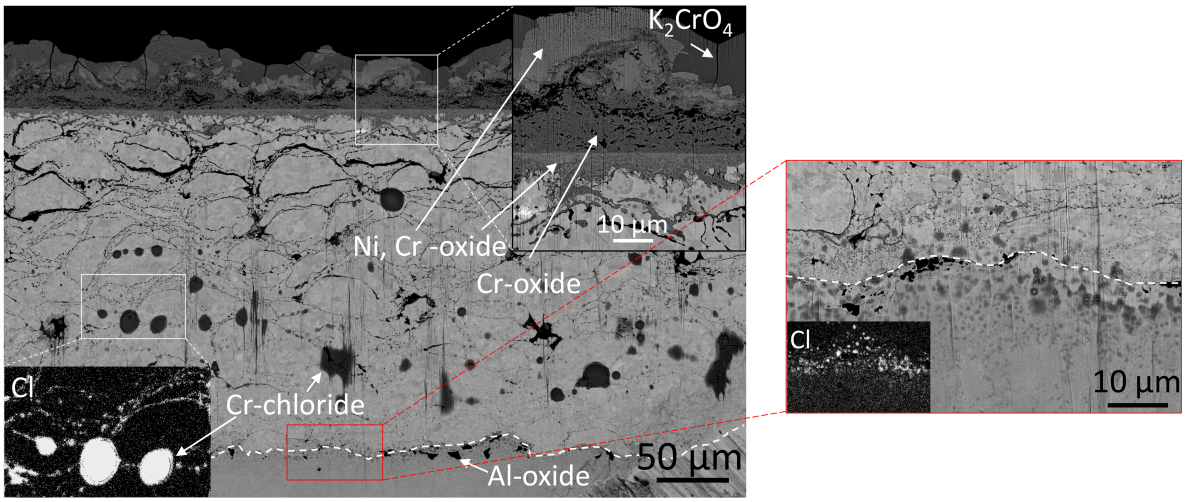

*Figure 46: SEM-BSE cross section image of **NiCr** coating after exposure in 5% O_2 + 20% H_2O + N_2 at 600 °C with **KCl present** for 168 hours. The dashed line shows the coating/substrate interface. Remaining Al-oxide from grit blasting of substrate observed at coating/substrate interface.*

The NiAl coatings are expected to reveal minor corrosion attacks due to the negative weight change. Accordingly, SEM analysis showed no significant corrosion attack on the NiAl coating, see Figure 46. Only minor oxide formations can be observed close to the surface of the coating, consisting of an internal Al-oxide. EDX-analysis detected no Cl along the splat boundaries of the coating which indicates that the Al-oxide prevents the diffusion of Cl. Thus, the NiAl coating is able to completely protect the substrate from exposure to any corrosive species. The reason behind the large differences in corrosion behaviour between the NiCr and the NiAl coatings may be that the chromia layer formed on the former breaks down due to the formation of K_2CrO_4 when reacting with KCl. This is expected for pure chromia formers in the presence of large amounts of alkali chlorides.

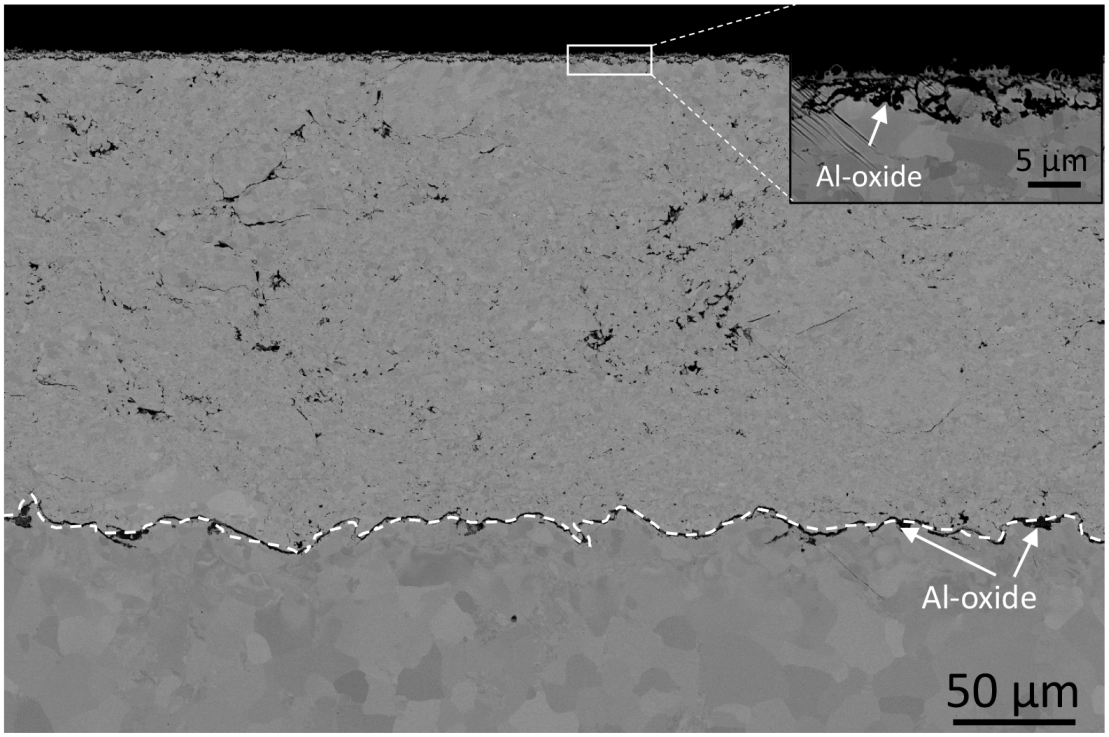

*Figure 47: SEM-BSE cross section image of **NiAl** coating after exposure in 5% O_2 + 20% H_2O + N_2 at 600 °C with **KCl present** for 168 hours. The dashed line indicates the coating/substrate interface. Remaining Al-oxide from grit blasting of substrate observed at coating/substrate interface.*

The NiCrAlY coating exhibited the lowest mass gain in the absence of KCl, see Figure 40. In the presence of KCl the coating still displays a low degree of corrosion attack compared to the NiCr coatings as well as the 304L bulk samples. However, the NiCrAlY coatings exhibits higher weight gain than the NiAl coating which could be explained by the SEM analysis which showed the formation of K_2CrO_4 on the surface of the former, see Figure 47. Apart from this, the coating displays a protective behavior as no cracks has propagated and no metal chlorides has formed. However, EDX analysis showed that Cl has diffused through the coating underneath the K_2CrO_4 crusts to a depth of 80 µm. The reason behind this may be that the protective oxide in these areas has been broken down which enables the corrosive species to penetrate the coating. EDX-analysis also showed that Cr has been accumulated along the splat boundaries underneath the K_2CrO_4 which may be explained by the higher driving force for Cr to diffuse to the surface due to Cr-depletion when reacting with the KCl. It is unclear how the performance of the coating would be affected by further depletion of Cr after longer exposures with larger amounts of KCl.

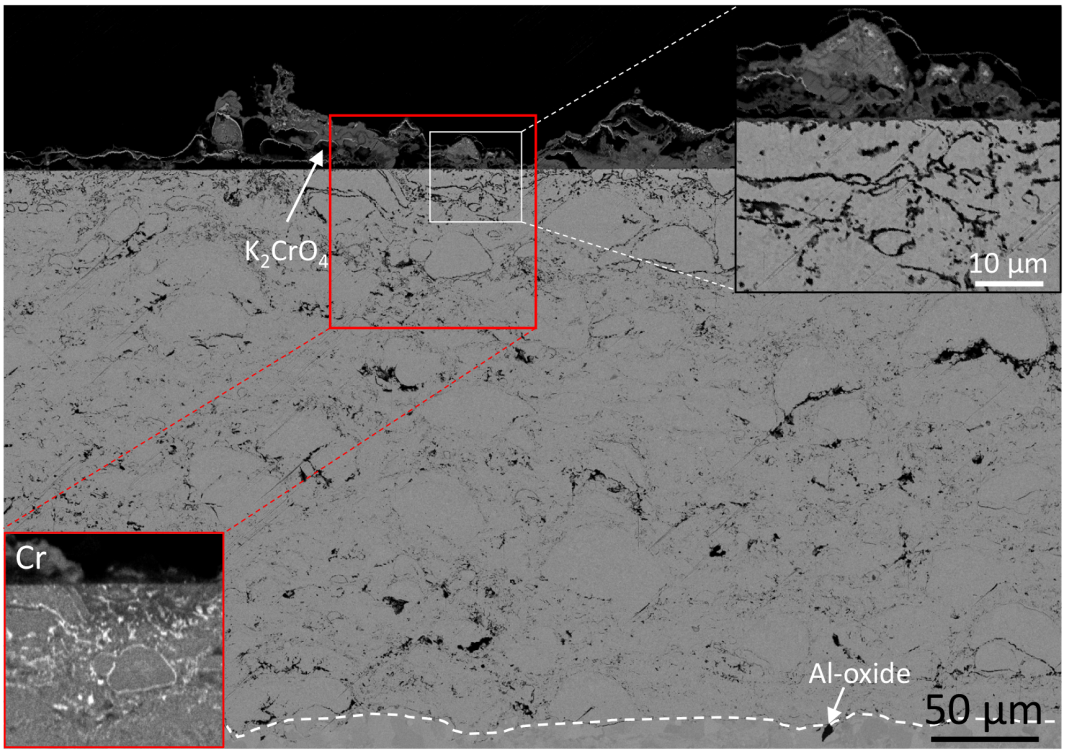

*Figure 48: SEM-BSE cross section image of **NiCrAlY** coating after exposure in 5% O_2 + 20% H_2O + N_2 at 600 °C with **KCl present** for 168 hours. The box in the bottom left corner shows the EDX-map for Cr. The dashed line indicates the coating/substrate interface. Remaining Al-oxide from grit blasting of substrate observed at coating/substrate interface.*

8 Summary

The findings of this study has been presented and discussed in the previous chapters. Conclusions and important remarks based on these will be summarized in the following subchapters.

8.1 Effect of Si-addition on high temperature corrosion behaviour of FeCrAl alloys

Exposures of FeCrAl model alloys with varying Si content was performed at medium-high temperatures (600 °C) in three corrosive environments (O_2, O_2+H_2O and O_2+H_2O+KCl) in order to investigate the beneficial effect of Si additions on the high temperature corrosion behaviour. Based on previous studies of Si-containing stainless steels the FeCrAl model alloys of this study were expected to form a SiO_2 layer which may act as a diffusion barrier, inhibiting the diffusion of corrosive species to the steel.

Accordingly, the Si-additions to the FeCrAl alloys resulted in reduced corrosion attack in all investigated environments:

- In dry oxygen, all alloys formed thin protective oxides on the surface. However, minor formation of iron oxide could be observed (nodules and individual covered grains) for FeCrAl**0Si** and FeCrAl**1Si**.
- In oxygen and water vapour, Si-addition resulted in the retention of the primary protection while FeCrAl**0Si** lost the primary protection and as a result formed thick iron-rich oxide (breakaway oxidation due to Cr-evaporation). Thus, Si may have direct or indirect effects on the Cr-evaporation.
- In oxygen and water vapour with KCl present, all alloys transitioned from the primary protection to the secondary protection, forming thick iron-rich oxide scales. However, the oxide growth rate was drastically reduced upon addition of Si to the alloy.

In contrast to the previous studies, TEM analysis showed that no SiO_2 layer had formed on the Si-containing alloys in any of the environments. Thus, the enhanced corrosion protection upon Si-addition is not due to the presence of a SiO_2 diffusion barrier. Furthermore, TEM analysis showed that the composition of corundum oxide changed upon addition of Si in dry oxygen. In the absence of Si, the Cr content was relatively high through the entire oxide and was also present in the Al-rich parts of the oxide. In the presence of Si, pure chromia formed on the outer part of the oxide, leaving the rest of the oxide Al-rich and relatively free of Cr. Thermodynamic calculations displayed similar trends as those observed in the TEM/EDS analysis which shows promise for future modelling of corrosion processes.

The retention of the primary protection (thin corundum oxide) in O_2+H_2O with Si present in the alloy may be connected to the previously mentioned effect on the corundum oxide composition;

- In the absence of Si, the relatively high Cr-content through the entire oxide results in the breakdown of the primary protection due to Cr-evaporation.
- With Si present in the alloy, the outer Cr-rich part of the corundum oxide evaporates while the inner Al-rich part remains intact.

Several hypotheses regarding the mechanism(s) behind the beneficial effect of Si on the secondary protection, including:

- Presence of Si in the spinel alters the diffusion properties of elements through the spinel.
    - Reduced inward diffusion rate of oxygen.
    - Reduced outward diffusion rate of iron.
- Absorption of oxygen in the alloy by Si, resulting in reduced oxidation of other alloying elements.

To confirm suggested mechanisms, further TEM studies combined with thermodynamic and kinetic modelling is needed, see Future Work.

The work with model alloys showed great potential for studying the influence of alloying elements on the corrosion behaviour. However, while utilizing model alloys, it is of great importance for parameters such as alloy grain size and distribution of trace elements to be well controlled to ensure accurate interpretations of the results.

8.2 Performance of HVAF-sprayed Ni-based coatings for high temperature corrosion protection

The performance of three HVAF-sprayed Ni-based coatings (NiCr, NiAl and NiCrAlY) for corrosion protection was investigated in a corrosive lab environments (O_2+H_2O and O_2+H_2O+KCl), mimicking the conditions in a biomass- and waste-fired boiler. Previous use of coatings in corrosive environments is often associated with spallation, caused by poor adhesion, and insufficient protection of the substrate due to high degree of porosity. HVAF-spraying technique has been shown to result in coatings with improved adhesion to substrate and reduced porosity, enabling them to withstand highly corrosive environments.

The performance of the coatings in this study was largely affected by the compositions and the environment:

Interdiffusion of Ni from the coating to the low-alloyed steel substrate (16Mo3) occurred for all coatings, which resulted in austenitization of the upper part of the substrates. The degree of interdiffusion was higher for the NiCr and NiAl coatings compared to the NiCrAlY coatings due to the higher driving force for interdiffusion resulting from the larger Ni-content gradient between coatings and substrate. Mechanical properties of the substrate may be affected by interdiffusion of certain elements which can lead to embrittlement and spallation of the coating. However, in this study no such effects were observed.

In O_2+H_2O all coatings displayed higher mass gains compared to the bulk stainless steel 304L samples. However, SEM analysis showed that thin protective oxides had formed on the coating surfaces. Oxide formation was observed in the NiCr coating but not for the NiAl and NiCrAlY coatings which indicates that the protective oxide of the former is susceptible to penetration of corrosive species.

In the presence of KCl, all coatings except the NiCr coating exhibited significantly lower mass gains than the 304L samples. SEM analysis showed that the NiCr coating experienced severe corrosion attack with formation of thick oxide and penetration of Cl to a depth close to the substrate. NiAl and NiCrAlY only displayed minor corrosion attack with the former exhibiting a seemingly intact protective oxide. The high performance of the NiAl and NiCrAlY coatings in this highly corrosive environment is promising for further studies in more corrosive environments, such as in a biomass and waste-fired boiler.

9 Future Work

In this study, two different material approaches for mitigating high temperature corrosion in biomass- and waste-fired boilers has been investigated; improving the corrosion behaviour of FeCrAl alloys by altering the alloying composition and the utilization of HVAF-sprayed Ni-based coatings.

In the former approach, changing the Si-content was investigated which showed great beneficial effects on the corrosion properties of the FeCrAl alloys. However, the mechanism behind this effects is still not completely understood. Therefore, further investigations, using more detailed transmission electron microscopy in combinations with both thermodynamic and kinetic calculations as well as atomistic calculations such as DFT will be performed. In addition, the effect of Cr and Al on the corrosion behaviour will be studied to get a better understanding of the role of the different alloying elements in FeCrAl alloys.

The HVAF-sprayed NiAl and NiCrAlY coatings displayed promising corrosion behaviour to be used to protect metal components from corrosion attack in very harsh environment. In this study, the coatings were studied for a limited amount of time. It is of great importance to investigate the performance of these coatings when exposed for longer times as well as included more realistic conditions such as temperature cycling which is known to be detrimental for both bulk materials and coatings. An additional step is to investigate the performance of these coatings in an actual biomass- and waste-fired boiler.

10 Acknowledgements

First of all I would like to thank my supervisors, Professor Jan-Erik Svensson, Associate Professor Jesper Liske and Associate Professor Torbjörn Jonsson for all their support, advices and inspiring discussions.

Furthermore, I would also like to acknowledge the High Temperature Corrosion Centre (HTC), the Consortium for Material Technology regarding Thermal Energy Processes (KME), the Swedish Energy Agency (SEA), Västra Götalandsregionen (VGR) as well as their member companies for support and funding. Special thanks to Kanthal for support and for producing the wide range of alloys used in this study. Many thanks to Bo Jönsson for all the advice and interesting discussions.

Moreover, I would like to thank Esmaeil Sadeghi, Shrikant Joshi and Nicolaie Markocsan at University West for making the collaboration study, included in this thesis, possible.

In addition, I would like to thank Sandra Gustafson, Anna Oskarsson and Christina Andersson for assistance with administrative matters. I would also like to thank Esa Väänänen, Torbjörn Jönsson and Erik Brunius for technical support regarding laboratory systems and material preparation. Further, I would like to thank Mohammad Sattari, Anders Kvist and Stefan Gustafsson for technical support regarding microscopy.

I also want to thank all my other colleagues at Environmental Inorganic Chemistry in the division of Energy and Materials for creating a great work environment with a lot of laughs and fun activities both within and outside of work and for always being open to discussing and helping with work-related issues.

Finally I would like to thank my parents, including step parents, for supporting me and my decisions at all times. Special thanks to my partner, MyLan Truong, for always being there for me when things get tough, for cheering me up when I'm down and for motivating me to get back up on my feet.

11 References

1. *Global Warming*. [cited 2018 05-17]; Available from: https://earthobservatory.nasa.gov/Features/GlobalWarming/page2.php.
2. *Sea level*. 2018-05-16 [cited 2018 05-17]; Available from: https://climate.nasa.gov/vital-signs/sea-level/.
3. *Extreme Weather*. [cited 2018 05-17]; Available from: https://nca2014.globalchange.gov/highlights/report-findings/extreme-weather.
4. McCarthy, J.J., *Climate change 2001: impacts, adaptation, and vulnerability: contribution of Working Group II to the third assessment report of the Intergovernmental Panel on Climate Change*. 2001: Cambridge University Press.
5. Parry, M., et al., *Climate change 2007: impacts, adaptation and vulnerability*. Vol. 4. 2007: Cambridge University Press Cambridge.
6. Field, C.B., et al., *IPCC, 2014: Climate Change 2014: Impacts, Adaptation, and Vulnerability. Part A: Global and Sectoral Aspects. Contribution of Working Group II to the Fifth Assessment Report of the Intergovernmental Panel on Climate Change*. 2014, Cambridge University Press, Cambridge, United Kingdom and New York, NY, USA.
7. Asteman, H., et al., *Oxidation of stainless steel in H2O/O-2 environments - Role of chromium evaporation*, in *High Temperature Corrosion and Protection of Materials 6, Prt 1 and 2, Proceedings*, P. Steinmetz, et al., Editors. 2004, Trans Tech Publications Ltd: Zurich-Uetikon. p. 775-782.
8. Pettersson, J., et al., *The Effects of KCl, K2SO4 and K2CO3 on the High Temperature Corrosion of a 304-Type Austenitic Stainless Steel.* Oxidation of Metals, 2011. **76**(1): p. 93-109.
9. Pettersson, C., L.G. Johansson, and J.E. Svensson, *The Influence of Small Amounts of KCl(s) on the Initial Stages of the Corrosion of Alloy Sanicro 28 at 600 °C.* Oxidation of Metals, 2008. **70**(5): p. 241-256.
10. Karlsson, S., et al., *Alkali Induced High Temperature Corrosion of Stainless Steel: The Influence of NaCl, KCl and CaCl2.* Oxidation of Metals, 2012. **78**(1): p. 83-102.
11. Kofstad, P., *High temperature corrosion*. 1988, London; New York, N.Y.: Elsevier applied science.
12. Götlind, H., et al., *The Effect of Water Vapor on the Initial Stages of Oxidation of the FeCrAl Alloy Kanthal AF at 900 °C.* Oxidation of Metals, 2007. **67**(5): p. 251-266.
13. Liu, F., et al., *TEM investigation of the oxide scales formed on a FeCrAlRE alloy (Kanthal AF) at 900°C in dry O2 and O2 with 40% H2O.* Materials at High Temperatures, 2005. **22**(3-4): p. 521-526.
14. Israelsson, N., et al., *KCl-Induced Corrosion of an FeCrAl Alloy at 600 °C in O2 + H2O Environment: The Effect of Pre-oxidation.* Oxidation of Metals, 2015. **83**(1): p. 29-53.
15. Israelsson, N., et al., *KCl-Induced Corrosion of the FeCrAl Alloy Kanthal ® AF at 600 °C and the Effect of H2O.* Oxidation of Metals, 2015. **83**(1): p. 1-27.
16. Josefsson, H., et al., *Oxidation of FeCrAl alloys at 500–900°C in dry O2.* Materials and Corrosion, 2005. **56**(11): p. 801-805.
17. Jonsson, T., et al., *Microstructural investigation of the effect of water vapour on the oxidation of alloy 353 MA in oxygen at 700 and 900°C.* Materials at High Temperatures, 2005. **22**(3-4): p. 231-243.
18. Basu, S.N. and G.J. Yurek, *Effect of alloy grain size and silicon content on the oxidation of austenitic Fe-Cr-Ni-Mn-Si alloys in pure O2.* Oxidation of Metals, 1991. **36**(3): p. 281-315.
19. Wouters, Y., et al., *Oxygen and Water Vapour Oxidation of 15Cr Ferritic Stainless Steels with Different Silicon Contents.* Materials Science Forum, 2004. **461-464**: p. pp. 839-848.
20. Nguyen, T.D., J. Zhang, and D.J. Young, *Effects of Silicon and Water Vapour on Corrosion of Fe–20Cr and Fe–20Cr–20Ni Alloys in CO2 at 650 °C.* Oxidation of Metals, 2017. **87**(3): p. 541-573.

21. Whittle, D.P. and J. Stringer, *Improvements in High Temperature Oxidation Resistance by Additions of Reactive Elements or Oxide Dispersions.* Philosophical Transactions of the Royal Society of London. Series A, Mathematical and Physical Sciences, 1980. **295**(1413): p. 309-329.
22. Pint, B.A., *Progress in understanding the reactive element effect since the Whittle and Stringer literature review*. 2001. 9-19.
23. Naumenko, D., B.A. Pint, and W.J. Quadakkers, *Current Thoughts on Reactive Element Effects in Alumina-Forming Systems: In Memory of John Stringer.* Oxidation of Metals, 2016. **86**(1): p. 1-43.
24. Sadeghimeresht, E., N. Markocsan, and P. Nylén, *Microstructural and electrochemical characterization of Ni-based bi-layer coatings produced by the HVAF process.* Surface and Coatings Technology, 2016. **304**: p. 606-619.
25. Sadeghimeresht, E., et al., *Effect of water vapor on the oxidation behavior of HVAF-sprayed NiCr and NiCrAlY coatings*. 2018.
26. Van Wylen, G.J., R.E. Sonntag, and C. Borgnakke, *Fundamentals of classical thermodynamics*. Vol. 1. 1994: John Wiley & Sons.
27. Senior, C.L., et al., *Gas-phase transformations of mercury in coal-fired power plants.* Fuel Processing Technology, 2000. **63**(2): p. 197-213.
28. Karlsson, S., L.-E. Åmand, and J. Liske, *Reducing high-temperature corrosion on high-alloyed stainless steel superheaters by co-combustion of municipal sewage sludge in a fluidised bed boiler.* Fuel, 2015. **139**: p. 482-493.
29. Kassman, H., et al., *Two strategies to reduce gaseous KCl and chlorine in deposits during biomass combustion — injection of ammonium sulphate and co-combustion with peat.* Fuel Processing Technology, 2013. **105**: p. 170-180.
30. Nielsen, H.P., et al., *The implications of chlorine-associated corrosion on the operation of biomass-fired boilers.* Progress in Energy and Combustion Science, 2000. **26**(3): p. 283-298.
31. Pettersson, J., et al., *The Influence of Sulfur Additions on the Corrosive Environments in a Waste-Fired CFB Boiler.* Materials Science Forum, 2006. **522-523**: p. 563-570.
32. Folkeson, N., et al., *Fireside Corrosion of Stainless and Low Alloyed Steels in a Waste-Fired CFB Boiler; The Effect of Adding Sulphur to the Fuel.* Materials Science Forum, 2008. **595-598**: p. 289-297.
33. Bott, J., et al., *Al N formation in Fe-A l alloys in N2-O 2 atmospheres.* Materials and Corrosion, 2014. **65**(3): p. 296-304.
34. Prescott, R. and M.J. Graham, *The oxidation of iron-aluminum alloys.* Oxidation of Metals, 1992. **38**(1): p. 73-87.
35. Young, D.J., *High Temperature Oxidation and Corrosion of Metals*. 2008: Elsevier.
36. Field, K.G., et al., *Handbook on the Material Properties of FeCrAl Alloys for Nuclear Power Production Applications.* 2017.
37. Song, L., et al., *Effects of Silicon on Mechanical Properties and Fracture Toughness of Heavy-Section Ductile Cast Iron*. Vol. 5. 2015. 150-161.
38. Chen, S. and L. Rong, *Effect of silicon on the microstructure and mechanical properties of reduced activation ferritic/martensitic steel.* Journal of Nuclear Materials, 2015. **459**: p. 13-19.
39. Lyphout, C., et al., *Screening Design of Supersonic Air Fuel Processing for Hard Metal Coatings.* Journal of thermal spray technology, 2014. **23**(8): p. 1323-1332.
40. Hanson, T.C., C.M. Hackett, and G.S. Settles, *Independent control of HVOF particle velocity and temperature.* Journal of Thermal Spray Technology, 2002. **11**(1): p. 75-85.
41. Fauchais, P., *Understanding plasma spraying.* Journal of Physics D: Applied Physics, 2004. **37**(9): p. R86.
42. Birks, N., G.H. Meier, and F.S. Pettit, *Introduction to the high temperature oxidation of metals*. 2006: Cambridge University Press.
43. *The Ellingham diagram*. [cited 2018 06-12]; Available from: https://www.doitpoms.ac.uk/tlplib/ellingham_diagrams/ellingham.php.

44. D Jr, C.W., *Materials science and engineering: an introduction.* John Wiley & Sons. Inc.–New York, USA, 2007.
45. Ågren, M.H.J., *Diffusion and Equilibria An Advanced Course in Metallurgy*. 2002: KTH.
46. Wagner, C., *Beitrag zur theorie des anlaufvorgangs.* Zeitschrift für physikalische Chemie, 1933. **21**(1): p. 25-41.
47. Jones, D.A., *Principles and Prevention of Corrosion*. 1996: Prentice Hall.
48. Jonsson, T., et al., *High-Temperature Oxidation of FeCr(Ni) Alloys: The Behaviour After Breakaway.* Oxidation of Metals, 2017. **87**(3): p. 333-341.
49. Jonsson, T., et al., *Oxidation After Breakdown of the Chromium-Rich Scale on Stainless Steels at High Temperature: Internal Oxidation.* Oxidation of Metals, 2016. **85**(5): p. 509-536.
50. Khanna, A.S., *Introduction to high temperature oxidation and corrosion*. 2002: ASM international.
51. Young, E.W.A., P.C.M. Stiphout, and J.H.W. de Wit, *n-Type Behavior of Chromium (III) Oxide.* Journal of The Electrochemical Society, 1985. **132**(4): p. 884-886.
52. Opila, E.J., et al., *Theoretical and experimental investigation of the thermochemistry of CrO2 (OH) 2 (g).* The Journal of Physical Chemistry A, 2007. **111**(10): p. 1971-1980.
53. Ebbinghaus, B.B., *Thermodynamics of gas phase chromium species: the chromium oxides, the chromium oxyhydroxides, and volatility calculations in waste incineration processes.* Combustion and Flame, 1993. **93**(1-2): p. 119-137.
54. !!! INVALID CITATION !!! [17, 19, 48, 49].
55. Zahs, A., M. Spiegel, and H.J. Grabke, *Chloridation and oxidation of iron, chromium, nickel and their alloys in chloridizing and oxidizing atmospheres at 400–700°C.* Corrosion Science, 2000. **42**(6): p. 1093-1122.
56. Asteman, H., et al., *Indication of Chromium Oxide Hydroxide Evaporation During Oxidation of 304L at 873 K in the Presence of 10% Water Vapor.* Oxidation of Metals, 1999. **52**(1): p. 95-111.
57. Asteman, H., J.E. Svensson, and L.G. Johansson, *Evidence for Chromium Evaporation Influencing the Oxidation of 304L: The Effect of Temperature and Flow Rate.* Oxidation of Metals, 2002. **57**(3): p. 193-216.
58. Pettersson, J., et al., *KCl Induced Corrosion of a 304-type Austenitic Stainless Steel at 600°C; The Role of Potassium.* Oxidation of Metals, 2005. **64**(1-2): p. 23-41.
59. Karlsson, S., et al., *Alkali Induced High Temperature Corrosion of Stainless Steel: The Influence of NaCl, KCl and CaCl2.* Oxidation of Metals, 2012. **78**(1): p. 83-102.
60. McNallan, M.J., et al. *ACCELERATION OF THE HIGH TEMPERATURE OXIDATION OF METALS BY CHLORINE*. in *International Corrosion Conference Series*. 1983.
61. Grabke, H.J., E. Reese, and M. Spiegel, *The effects of chlorides, hydrogen chloride, and sulfur dioxide in the oxidation of steels below deposits.* Corrosion Science, 1995. **37**(7): p. 1023-1043.
62. Folkeson, N., L.-G. Johansson, and J.-E. Svensson, *Initial Stages of the HCl-Induced High-Temperature Corrosion of Alloy 310.* Journal of The Electrochemical Society, 2007. **154**(9): p. C515-C521.
63. Folkeson, N., et al., *The influence of small amounts of KCl(s) on the high temperature corrosion of a Fe-2.25Cr-1Mo steel at 400 and 500°C.* Materials and Corrosion, 2010. **62**(7): p. 606-615.
64. Sutton, A.P., *Interfaces in crystalline materials.* Monographs on the Physice and Chemistry of Materials, 1995: p. 414-423.
65. Jonsson, T., *Microscopy of high temperature oxidation of iron and some stainless steels*. 2007: Chalmers University of Technology.
66. Goldstein, J., et al., *Scanning electron microscopy and x-ray microanalysis. Kluwwer Academic*. 2003, Plenum Publishers: New York, etc.
67. Cullity, B.D., *Elements of X-ray Diffraction.*
68. Kaufman, L. and J. Ågren, *CALPHAD, first and second generation–Birth of the materials genome.* Scripta Materialia, 2014. **70**: p. 3-6.
69. Larsson, H., et al., *Oxidation of iron at 600 °C – experiments and simulations.* Materials and Corrosion, 2016. **68**(2): p. 133-142.

70. Hallström, S., et al., *High temperature oxidation of chromium: Kinetic modeling and microstructural investigation.* Solid State Ionics, 2013. **240**: p. 41-50.
71. Hallström, S., L. Höglund, and J. Ågren, *Modeling of diffusion in wustite and simulation of oxidation of iron at 600°C*, in *European Stainless Steel Conference Science and Market Helsinki, Finland, June 10–13, 2008*, K. Pentti and H. Staffan, Editors. 2008, Jernkontoret: Helsinki. p. 273-278.
72. Nguyen, T.D., J. Zhang, and D.J. Young, *Effects of Silicon on High Temperature Corrosion of Fe–Cr and Fe–Cr–Ni Alloys in Carbon Dioxide.* Oxidation of Metals, 2014. **81**(5): p. 549-574.
73. Jonsson, T., et al., *Microstructural Investigation of the Effect of Water Vapour on the Oxidation of the Si-Containing FeCrNi Steel 353MA at 900 (Degree Sign) C in Oxygen.* Meeting Abstracts, 2006. **MA2006-02**(18): p. 949.
74. RADAVICH, J.F., *Effect of Silicon on High Temperature Oxidation Of Stainless Steels.* CORROSION, 1959. **15**(11): p. 73-77.
75. Inoue, Y., N. Hiraide, and K. Ushioda, *Effect of Si Addition on Oxidation Behavior of Nb containing Ferritic Stainless Steel.* Tetsu-to-Hagane, 2016. **advpub**.
76. Jonsson, T., et al., *Oxidation of Fe–10Cr in O2 and in O2+H2O environment at 600°C: A microstructural investigation.* Corrosion Science, 2013. **75**: p. 326-336.
77. Jonsson, T., et al., *Influence of H[sub 2]O(g) on the Oxide Microstructure of the Stainless Steel 353MA at 900°C in Oxygen*. Vol. 154. 2007.
78. Hjörnhede, A. and A. Nylund, *Adhesion testing of thermally sprayed and laser deposited coatings.* Surface and Coatings Technology, 2004. **184**(2): p. 208-218.
79. Hjörnhede, A., P. Sotkovszki, and A. Nylund, *Erosion-corrosion of laser and thermally deposited coatings exposed in fluidised bed combustion plants.* Materials and Corrosion, 2006. **57**(4): p. 307-322.
80. Sadeghimeresht, E., et al., *Isothermal oxidation of HVAF-sprayed Ni-based chromia, alumina and mixed-oxide scale forming coatings in ambient air.* Surface and Coatings Technology, 2017. **316**: p. 10-21.
81. Pint, B.A., et al., *High temperature oxidation performance of aluminide coatings*. 2003, Oak Ridge National Lab., Oak Ridge, TN; Tennessee Technological University Cookeville, TN (US).
82. Texier, D., et al., *Effect of interdiffusion on mechanical and thermal expansion properties at high temperature of a MCrAlY coated Ni-based superalloy.* Surface and Coatings Technology, 2016. **307**: p. 81-90.
83. Niewolak, L., et al., *Behavior of interconnect steels in carbon containing simulated anode gas of solid oxide fuel cells.* Journal of The Electrochemical Society, 2012. **159**(11): p. F725-F732.
84. Totten, G.E., *Handbook of residual stress and deformation of steel*. 2002: ASM international.
85. Cverna, F., *Thermal properties of metals.* ASM International, Materials Park, OH, 2002.
86. Jafari, R., et al., *KCl-Induced High-Temperature Corrosion Behavior of HVAF-Sprayed Ni-Based Coatings in Ambient Air.* Journal of Thermal Spray Technology, 2018. **27**(3): p. 500-511.
87. Kassman, H., et al., *Measures to reduce chlorine in deposits: Application in a large-scale circulating fluidised bed boiler firing biomass.* Fuel, 2011. **90**(4): p. 1325-1334.
88. Steinmetz, P. and C. Rapin, *Corrosion of Metallic Materials in Waste Incinerators.* Materials Science Forum, 1997. **251-254**: p. 505-518.